

UNIVERSITY OF BELGRADE
FACULTY OF TECHNOLOGY AND METALLURGY

Abubkr Mohamed Abdulhamid Abdulah HEMER

**ELASTIC-PLASTIC BEHAVIOR OF HIGH
STRENGTH STEEL WELDED JOINT UNDER
STATIC AND DYNAMIC LOADING**

Doctoral Dissertation

Belgrade, 2021

UNIVERZITET U BEOGRADU
TEHNOLOSKO-METALURSKI FAKULTET

Abubkr Mohamed Abdulhamid Abdulah HEMER

**ELASTOPLASTIČNO PONAŠANJE
ZAVARENOG SPOJA ČELIKA VISOKE
ČVRSTOĆE PRI DELOVANJU STATIČKOG I
DINAMIČKOG OPTEREĆENJA**

doktorska disertacija

Beograd, 2021

Mentor of Doctoral Dissertation: Prof. Ljubica Milovic, full professor, University of Belgrade,
Faculty of Technology and Metallurgy

Member of Committee:

Prof. Ljubica Milovic, full professor, University of Belgrade, Faculty of Technology and
Metallurgy

Signature:

Prof. Slaviša Putić, full professor, University of Belgrade, Faculty of Technology and Metallurgy

Signature:.....

Prof. Aleksandar Grbovic, full professor, University of Belgrade, Faculty of Mechanical
Engineering

Signature:

Date of Defense:

Mentor: Prof. dr Ljubica Milović, redovna profesorka, Univerzitet u Beogradu, Tehnološko-metalurški fakultet

Članovi komisije:

Prof. dr Slaviša Putić, redovni profesor, Univerzitet u Beogradu, Tehnološko-metalurški fakultet

Prof. dr Aleksandar Grbović, redovni profesor, Univerzitet u Beogradu, Mašinski fakultet

Datum odbrane:

Acknowledgment

We thank and praise **God** of the end of my journey in obtaining my Ph.D. I have not travelled in a vacuum in this journey. This thesis has been seen through to completion with the support and encouragement of numbers people including my well-wishers, my friends and colleagues. At the end of my thesis I would like to thank all those people who made this thesis possible and an unforgettable experience for me.

I would like to take this opportunity to express my sincere and heartfelt gratitude to all those who made this report possible.

At first I would like to thank my Guide, Thesis supervisor **Prof. Ljubica Milovic** from the Department of General Technical Sciences, Faculty of Technology and Metallurgy, who enabled me to work at Research and Development, Scientific Services. Without her support and invaluable guidance, it was impossible for me to complete this work.

I wish to express my thanks to Prof. Aleksandar Sedmak who helped me in the theoretical part of Fracture mechanics.

Appreciation is also extended to Prof. Blagoj Petrovski who was generous with his insight and guidance and contributions of experimental data.

I am also grateful to Prof. Aleksandar Grbovic, whom I learned a great deal from his experience and knowledge of finite element codes which is implemented in simulation of experimental results, for encouraging, providing research facilities, helping me in analyzing data and support during this investigation.

I would also like to express my sincere gratitude to the committee member Prof. Slavisa Putic. He kindly spent his time for my dissertation.

I thank my beloved friends of my college worked along with me Mrs. Bojana Zecevic, M. Sc. in Technology and Mrs. Ana Maksimovic, M. Sc. in Biotechnology.

At last, but not the least, I thank my **Family Members** without whom support and motivation I couldn't complete this work.

Elastic-Plastic behavior of welded joint made of high strength steel under static and dynamic loading

ABSTRACT

Welding is one of the most common process in industrial or production engineering practice for components joining. Its main advantages are high speed in manufacturing combined with low costs and, usually, a high degree of flexibility, integrity and reliability. Nevertheless, welding is a highly complex metallurgical process and, therefore, weldments are susceptible to cracking, flaws and residual stresses which may lead to structural failure and life time reduction.

Welded structures have wide range of applications in many industries. Steel grade DIN 15NiMoCrB4-5, which is a low-carbon microalloyed steel alloyed with Nickel and Molybdenum, which is used in line pipes for transporting oil and natural gas has been investigated. Its yield stress is 668 MPa and the UTS are close to 820 MPa. Catastrophic structure failure made of this steel grade due to fatigue is reported to cause sudden damage and loss to human-lives, as well as property. Hence, from end application point of view, knowledge on fracture toughness is of immense importance.

Several tests were conducted on the welded joints. Fracture mechanics toughness testes using three point bending specimens were done. Obtained results of the applied force and CMOD were processed in order to determine the value of K_{IC} , CTOD or J -integral.

The pre-crack was created using fatigue and the crack propagation was measured using the unloading compliance method. Calculation of critical values J_{IC} are compared with the values obtained by using FEM. The FEM model was defined on the basis of experimental condition in program Ansys.

The goal of this research was to determine effect of welded joint geometry (different zone sizes) and crack location on fatigue life. First welded joints were made using the MIG procedure and investigated in terms of mechanical and fatigue properties. The focus of this study was on experimental and numerical analysis, with special focus on the heat-affected zone.

Key words: HSLA steel, J -integral, J - R curve, Paris law, XFEM, integrity, life.

Scientific field: Technological engineering

Scientific subfield: Material engineering

Elastoplastično ponašanje zavarenog spoja čelika visoke čvrstoće pri delovanju statičkog i dinamičkog opterećenja

SAŽETAK

Zavarivanje je jedan od najčešćih procesa spajanja komponenata u industrijskoj ili proizvodnoj praksi. Njegove glavne prednosti su brzina izrade kombinovana sa niskom cenom i obično sa visokim stepenom fleksibilnosti, integriteta i pouzdanosti. Bez odzira na to, zavarivanje je izuzetno složen metalurški postupak i prema tome, zavareni spojevi su osetljivi na stvaranje prslina, grešaka i zaostale napone, što može dovesti do otkaza konstrukcije i skraćenja veka.

Zavarene konstrukcije imaju široku primenu u mnogim granama industrije. U ovom radu je ispitan čelik 15NiMoCrB4-5 čvrstoće popuštanja 668 MPa i zatezne čvrstoće blizu 820 MPa. Ovaj materijal je niskouglenični mikrolegirani čelik legiran niklom i molibdenom, koji se koristi za izradu cevovoda za transport nafte i prirodnog gasa. U takvoj primeni, katastrofalni lom izazvan zamorom uzrokuje iznenadna oštećenja imovine i pogibiju ljudi. Stoga je, sa stanovišta krajnje primene, poznavanje žilavosti loma od ogromne važnosti.

Urađena su eksperimentalna ispitivanja na zavarenim spojevima. Od ispitivanja mehanike loma urađeno je ispitivanje žilavosti loma na epruvetama za savijanje u tri tačke. Obradeni su rezultati izmerene primenjene sile i CMOD da bi se utvrdila vrednost K_{IC} , CTOD ili J -integrala.

Stvaranje zamorne prsline i propagacija prsline su merene metodom popuštanja. Izračunate kritične vrednosti, J_{IC} , su upoređene sa vrednostima dobijenim pomoću MKE. Model MKE je definisan na bazi eksperimentalnih uslova u programu Ansys.

Cilj ovog istraživanja je bio da se utvrdi uticaj geometrije zavarenih spojeva (različite veličine zona) i položaja prsline na zamorni vek. Najpre su zavareni spojevi napravljeni MIG postupkom i ispitani su u pogledu mehaničkih osobina i osobina zamora. Fokus izučavanja je bio na eksperimentalnoj i numeričkoj analizi, sa posebnim osvrtom na zonu pod uticajem toplote.

Ključne reči: mikrolegirani čelik povišene čvrstoće, J -integral, J - R kriva, Parisov zakon, proširena metoda konačnih elemenata, integritet, vek.

Naučna oblast: Tehnološko inženjerstvo

Uža naučna oblast: Inženjerstvo materijala

LIST OF PUBLICATION RELATED TO THE DOCTORAL THESIS

1. Aleksić B., Aleksić V., **Hemer A.**, Milović Lj., Grbović A.: Determination of the Region of Stabilization of Low-Cycle Fatigue HSLA Steel from Test Data, In: Proceedings of the 17th International Conference on New Trends in Fatigue and Fracture, Eds: Ricardo R. Ambriz, David Jaramillo, Gabriel Plascencia and Moussa Nait Abdelaziz, Springer, 2018, pp. 101-113.
2. Aleksić B., Grbović A., **Hemer A.**, Milović Lj., Aleksić V.: Evaluation of Stress Intensity Factors (SIFs) Using Extended Finite Element Method (XFEM), In: Proceedings of the 17th International Conference on New Trends in Fatigue and Fracture, Eds: Ricardo R. Ambriz, David Jaramillo, Gabriel Plascencia and Moussa Nait Abdelaziz, Springer, 2018, pp. 355-369
3. Aleksić B., Grbović A., Milović Lj., **Hemer A.**, Aleksić V.: Numerical simulation of fatigue crack propagation: A case study of defective steam pipeline, Engineering Failure Analysis, Vol. 106, December 2019, 104165. ISSN 1350-6307; IF: 2,203.
<https://doi.org/10.1016/j.engfailanal.2019.104165>
4. **Hemer A.**, Milović Lj., Grbović A., Aleksić B., Aleksić V.: Numerical determination and experimental validation of the fracture toughness of welded joints, Engineering Failure Analysis, Vol. 107, January 2020, 104220. ISSN 1350-6307; IF: 2,203.
<https://doi.org/10.1016/j.engfailanal.2019.104220>
5. Aleksić V., Milović Lj., Aleksić B., Bulatović S., Burzić Z., **Hemer AM**: Behavior of Nionical-70 in Low-cycle fatigue, Integrity and life of structures, Vol. 17, No. 1, 2017, pp. 61-73. ISSN 1451-3749.
6. Aleksić V., Milović Lj., Aleksić B., **Hemer AM**: Indicators of HSLA steel behavior under low cycle fatigue loading, 21 st European Conference on Fracture, ECF21, Procedia Structural Integrity 2, 2016, pp. 3313-3321.
7. Aleksić B., Milović Lj., Grbović A., **Hemer A.**, Aleksić V., Zrilić M.: Experimental and numerical investigation of the critical values of J-integral for the steel of steam pipelines, ECF 22-Loading and Environmental Effects on Structural Integrity, Serbia 2018, Procedia Structural Integrity 13, 2018, pp. 1589-1594.
8. Aleksić B., Aleksić V., Milović Lj., **Hemer A.**, Prodanović A.: Determination of polynomial depending between hardness and cooling time $8t_8 / 5$ of steel NIONICRAL 70 heat affected zone, - 18th International Conference on New Trends in Fatigue and Fracture NT2F18, July 17-20, 2018, Lisbon, Portugal, pp. 87-90.
9. Aleksić B., **Hemer A.**, Jančić Heinemann R., Dimitrijević M., Milović Lj., The analysis of SEM photographs of fractured surfaces of steel P91 and compared with the mechanical properties such as impact energy (toughness), Program & Book of Abstracts, Fifteenth Young Researchers' Conference (15yrc 2016), Materials Science and Engineering, December 7-9, 2016, Serbian Academy of Sciences and Arts, Belgrade, Serbia, p. (6-5).

TABLE OF CONTENTS

1. INTRODUCTION	1
1.1. Literature overview	3
2. fracture mechanics	8
2.1. Fundamentals of elastic-plastic fracture mechanics	11
2.1.1. Crack opening displacement	11
2.1.2. Rice's contour integral	12
2.1.3. The application of J-integral to crack initiation	13
2.2. FATIGUE	14
2.2.1. Material resistance under variable loading (fatigue)	14
2.2.2. Fracture mechanics analysis of fatigue	17
3. EXPERIMENTAL RESEARCH	21
3.1. Tensile tests	21
3.2. CHARPY testing	28
3.3. Fatigue testing results	30
3.4. Fracture Mechanics testing	35
3.4.1 Fracture toughness testing of WM	36
3.4.2 Fracture toughness testing of HAZ	57
3.4.3. Fracture toughness testing of PM	78
4. NUMERICAL SIMULATION OF THE FRACTURE TOUGHNESS OF WELDED JOINTS – STATIC LOADING	82
4.1. Finite Element Calculation of <i>J</i> -integral values	83
4.1.1. Specimen made of WM	84
4.1.2. Specimen made of PM	86
4.2. Results and discussion	86
5. FATIGUE CRACK GROWTH IN DIFFERENT WELDMENT ZONES	88
5.1. Materials and FEM input parameters	89
5.2. Numerical simulation by the XFEM	89
6. WELDED JOINT INTEGRITY ASSESSMENT BASED ON ANALYTICAL FRACTURE MECHANICS	98
6.1. Analytical basis	99
6.2. Results	101
6.3. Comparison of analytical and numerical analysis	106
6.4. Discussion	108
7. CONCLUSIONS	109
LITERATURE	111

1. INTRODUCTION

In the recent decades, significant advancement was made in steel manufacturing, resulting in steel classes with much higher tensile strength, hardness and ductility, but also with better weldability compared to conventional structural steels. Modern welded steel structures, primarily aimed at working under dynamic load conditions and at low temperatures, are made of high strength steels, with improved mechanical properties, with guaranteed toughness at work temperatures and solid weldability. Thanks to modern steels, welded structures now have decreased mass, are more compact, and the driving power of mobile elements is decreased, all of which contributes to reduced manufacturing time and total production costs.

Since the weld metal (WM) still represents nothing more than a cast alloy whose strength mainly depends on its chemical composition, differences in mechanical properties between the plates and the filler materials are getting greater. Designers and welding technologists are faced with the problem of selecting the appropriate level of mismatching between the parent material (PM) and the WM, without compromising the mechanical properties of the welded joint as a whole.

The risk of welded structure failure is mainly related to the properties of its welded joints. Classic design rules avoid the necessity of considering this, since materials are generally selected based on their strength, under the basic assumption that the system will only be subjected to elastic deformation. Actually, welded joints are the locations of stress concentration, which is locally manifested by the presence of arbitrary defects, resulting from the welding process. In this way, the real threat of structural failure depends on the material in the vicinity of stress concentrations, regardless of the nature of failure, which could be due to fatigue, brittle fracture or extensive creeping. Thus, local properties of welded joints and the risk of existing defects represent two main factors which affect the safety of a welded structure.

A reliable and safe work life of load-bearing elements of welded structures is limited by the process of crack initiation and propagation due to dynamic exploitation conditions. Considerable attention is devoted to the problems involving safe exploitation, with a requirement that every predictable failure is prevented through thorough analyses before construction, via strict control during development and testing before manufacturing. Also, it should be kept in mind that failure actually represents crack growth, thus particular focus is on crack initiation and propagation.

The aim of this research is to study and predict fatigue crack growth in individual welded joint constituents for high strength steel subjected to static and dynamic load, which would enable a reliable assessment of its remaining work life, in the presence of defects.

Investigations within the framework of the proposed topic of this doctoral thesis were divided in the following stages:

- Literature review, including the available and relevant references
- Cutting of test specimens from welded plates, for the purpose of static and dynamic testing
- Experimental tests (determining of mechanical properties of welded joint constituents and the elastic-plastic fracture mechanics parameters);
- Development of the numerical model for fatigue crack growth, using the extended finite element method/

The doctoral thesis contains the following chapters:

1. Introduction, Theoretical part. Within the Introduction, the topic of this research will be defined, along with the main research goals. In Theoretical part, literature data gathered from relevant references related to the behavior of welded structure made of high strength steels in the presence of cracks under working load will be shown, along with crack acceptability criteria for welded joints in such structures.

2. Fracture Mechanics. Fundamental concepts of fracture mechanics are presented and discussed in relation to this work. Focus is placed on static elastic-plastic crack growth problems (*J-integral*) and fatigue crack growth (Paris law). Corresponding fracture mechanics parameters are also presented and discussed.

3. Experimental part. This chapter will define the steel used, along with the conditions and testing methods used for determining of its mechanical properties and fracture mechanics parameters.

4. Numerical simulation. This chapter will explain how the load and boundary conditions for the models were defined, how the finite elements were selected and how the finite element mesh was made for the purpose of simulating fatigue crack growth through all three regions of a welded joint (PM, WM and heat-affected zone HAZ). The results and discussion section will show the results of experimental and numerical analyses and their comparison, followed by a detailed discussion.

5. Fatigue crack growth in different zones Remaining life assessment in the presence of defects. This section of the thesis will involve an analytical calculation of the fatigue life, based on fracture mechanics parameters, and mainly related to the Paris law. The results will then be discussed and compared to the ones obtained by numerical simulation.

6. Conclusion. The conclusion will sum all of the obtained results and point out the most important conclusions resulting from experimental and numerical analyses.

7. Literature. This chapter will provide a list of scientific and expert literature that was used during the writing of this thesis, along with scientific papers which have resulted from it.

1.1. Literature overview

This chapter will present the results of specific papers which dealt with the topic in question, mainly related to fatigue and the application of steels P460NL1 [1.1, 1.2] and Protac 500, [1.3, 1.4], combined with the finite element method. Literature shown here will include papers from international conferences, journal and doctoral theses. These papers will provide insight into how this specific topic was selected for the thesis. More accurately, papers presented in this chapter will be focused on the following:

- Experimental and numerical analysis of specimens made of steels P460NL1, with particular focus on the HAZ
- Determining of Paris law coefficients C and m, via experiments
- Fatigue crack growth
- Application of relevant standards in fatigue analysis

Mechanical properties and fatigue crack growth rate in armour steel welded joints

The first paper presented in this chapter is an extract from the doctoral thesis of A. Čubrilo, from 2018 [1.3]. The subject of this thesis is fatigue in welded joints made of armour steel, with a focus on the negative effects of hydrogen, which represents yet another difference between this steel and P460NL1, since the latter has much better resistance to cold cracks. The thesis contains experimental analyses very similar to the ones from this work, and which were used as an inspiration for the investigations which will be shown here in the following chapters.

This experiment also involved shielded metal arc welding, using the MIG procedure with various gas mixtures – 2.5% CO₂ + argon, and 1.5% O₂ + argon. Both mixtures are suitable for welding of armour steels, wherein the first mixture is combined with ferritic or austenitic filler material, and the second one is used when welding is performed using the flux core arc welding procedure. Even though the welding procedures used in these two dissertations are essentially similar, there are certain considerable differences, due to required mechanical properties of the welded joints (armour steels require high levels of strength and hardness, P460NL1 requires high ductility. It should also be pointed out that in the case of armour steels, carbon content is of great importance, along with preventing of hydrogen diffusion into the HAZ, which is achieved by using austenitic filler materials, which are much more effective at dissolving hydrogen. This suggests the great importance of microstructures of all welded joint regions, which is, among other things, influenced by the adequate selection of welding technology.

The experimental stage of this thesis involved micro-hardness tests which determined that the microstructure of the welded joint in question was predominantly made of quenched and tempered martensite (with tempering temperature of 280°C and quenching temperature of 920°C), as can be seen in Fig. 1.1.

During welding of armour steels, identical preheating and interpass temperatures are used, with values ranging from 80 to 120°C. This temperature range ensures much higher amounts of upper and lower bainite compared to martensitic phase in the coarse-grain region, which limits the hardness of this region to 540 HV, wherein the hardness at a 15.9 mm distance from the weld axis must not be below 509 HV, in accordance with the relevant standard. In this case, slightly higher preheating (150°C) and interpass temperatures (160°C) were selected, in order to keep the cooling rate between 1-5°C per second, which was necessary in order to obtain a microstructure within the aforementioned boundaries (the upper hardness limit is necessary in order to decrease the tendency towards cold cracking).

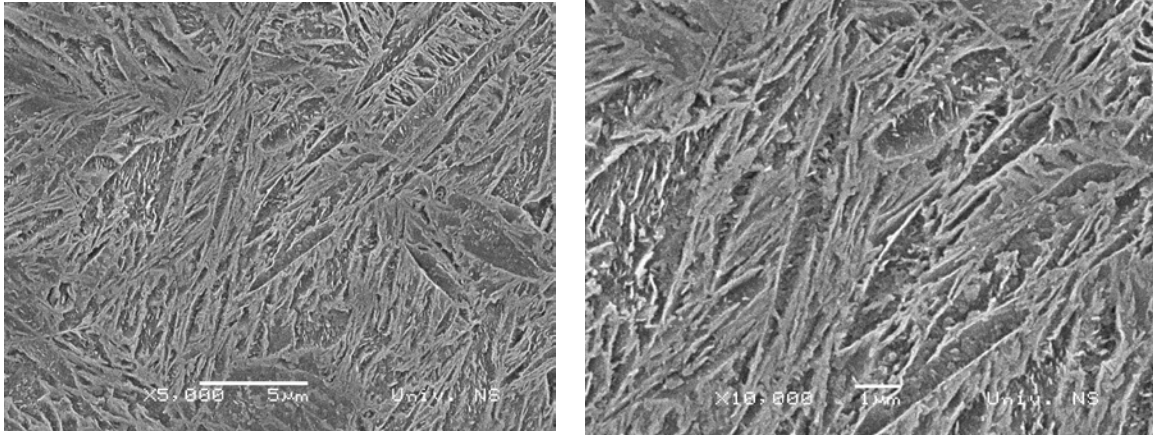


Figure 1.1 Microstructure of the armour steel Protac 500 [1.3]

Welded plates had dimensions of 200 x 100 x 11 mm, wherein groove edge angles were 27.5° , since it is common practice for these materials to use smaller angles, i.e. to weld them in narrow grooves, [1.4]). The multipass weld configuration is shown in Fig. 1.2, along with dimensions. As can be seen from the figure, a total of four passes were done. Welding temperatures were measured using thermocouples, similar to the procedure shown in [4]. Thermocouple scheme is given in Fig. 1.3. Each thermocouple was placed in a way that ensures it will measure the temperature during each individual welding pass.

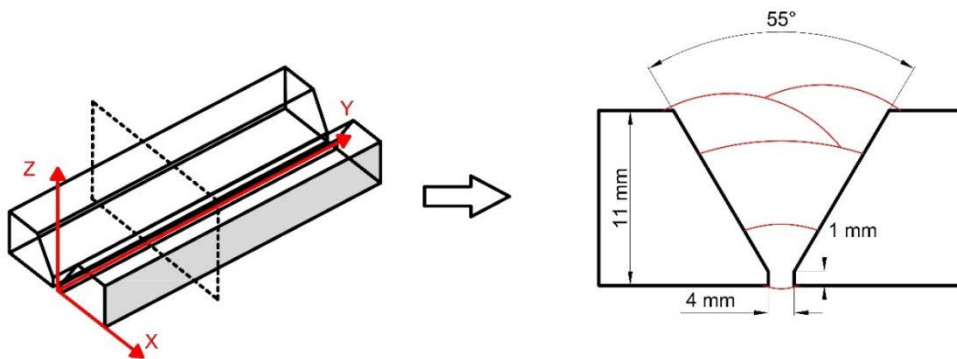


Figure 1.2. Armour steel Protac 500 welding scheme [1.3].

Hardness tests were performed after the welding activities, using a Micro Vickers Hardness Tester HVS device, manufactured by Laizhou Huazhin Testing Instrument Co. Ltd, with a force of 500 g. First measuring was performed at a 2 mm distance from the upper surface, and once the required hardness level was achieved, the welding of the remaining plates was carried out. Following this stage, a more detailed measuring of hardness was performed, in order to determine its distribution along the welded joint. An example of hardness measuring locations can be seen in Fig. 1.4 below.

Experimental investigation also involved toughness tests in the HAZ, using V-notched specimens. These tests were performed at temperatures of 40°C , -20°C , 0°C and 20°C . Impact energy depends on the microstructure and chemical composition of steels, where in the case of armour steels, this energy increases with heat input during the welding (due to an increase in cooling time $\Delta t_{6/2}$, needed for steel to cool from 600 to 200°C). It can be concluded from this that heat input also affects fracture toughness, in terms of crack initiation to crack propagation energy ratio.

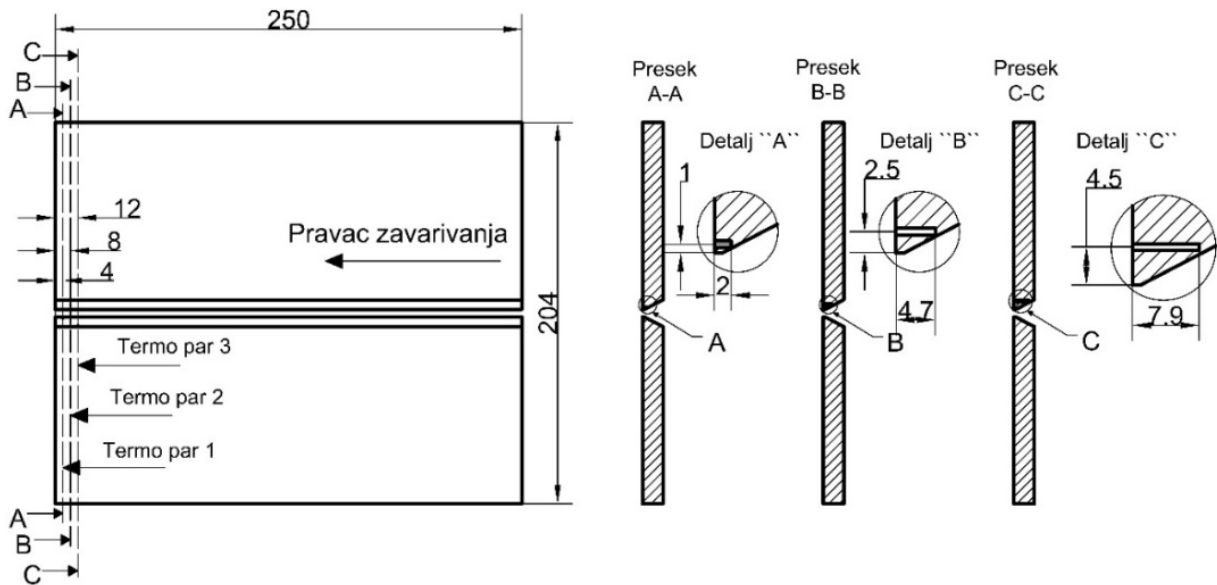


Figure 1.3. Thermocouple placement relative to the welding direction [1.2].

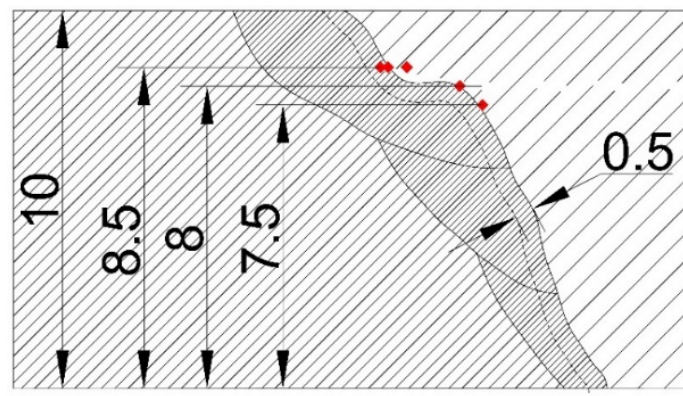


Figure 1.4. Hardness measuring location distribution [1.3].

Total impact energy values for specimens with notch in the PM ranged from 27.9 to 34.2 *J*, wherein the share of crack initiation energy was significantly higher than the crack propagation energy, being around 75-97% of total impact energy, depending on the test temperature. Fusion line impact energy was significantly higher at all temperatures, ranging from 40.0 to 75.3 *J*, wherein the ratio of crack initiation to crack propagation energy varied greatly, from 6:1 to 1:3. Crack initiation energy had a higher share at 20 and -40°C temperatures, whereas crack propagation energy was dominant in the remaining cases. In the case of specimens with the notch in the WM, total impact energy was between 61.5 and 84.4 *J*, wherein crack propagation energy was 1.5 to 3 times greater than crack initiation energy, at all temperatures. It can be observed that the values were far less different in the case of the WM, without extreme values which can be attributed to welded joint heterogeneity. Such values of total impact energy are typical for high-strength materials, and expectedly lower than the values obtained by testing of micro-alloyed high-strength steels [1.1], due to microstructural differences.

Regarding fatigue crack growth rate testing, the experiment was performed in accordance with ASTM E647 standard, which defines the measuring of crack growth rate da/dN , along with calculating of the stress intensity factor, ΔK . Crack growth rate was measured in all welded joint regions, using constant load amplitude during crack growth and with an increasing stress intensity

factor threshold. This test was performed using RUMUL Fractomat 7609/213 (same as in [1.1], which will be shown later in this chapter). In this case, RUMUL RMF-A10 foils were used, due to the size of the test specimens (with standard dimensions of 200 x 20 x 10 mm). All of these tests were performed at room temperature.

Based on test results obtained for fatigue crack growth rate, including $a-N$ and $da/dN - \Delta k$ diagrams, Paris law coefficients were determined, by fitting of corresponding curves, i.e. by approximating the stable crack growth part of the curve and determining its slope (m) and intersection with the y axis (coefficient C). Figs. 1.5 and 1.6 show these curves, wherein crack growth rate vs. SIF threshold curves, are shown in logarithmic scale.

Obtained coefficients were determined as the mean value for two tests, whereas ΔK was around $20 \text{ MPa}\sqrt{m}$, in the case of a crack in the PM. Values of C and m coefficients in this case were 10^{-9} m/cycle and 3.36, respectively. These coefficients were determined for specimens with the crack in the HAZ in similar manner, and they were 10^{-8} and 3.79. In addition to these two cases, a case wherein the crack was in the HAZ and the WM, and the resulting values were somewhat different – 3×10^{-13} for C and 5.68 for m , with the latter value being significantly higher than what is typically encountered in literature, which confirms the need for these coefficients to be experimentally determined whenever possible.

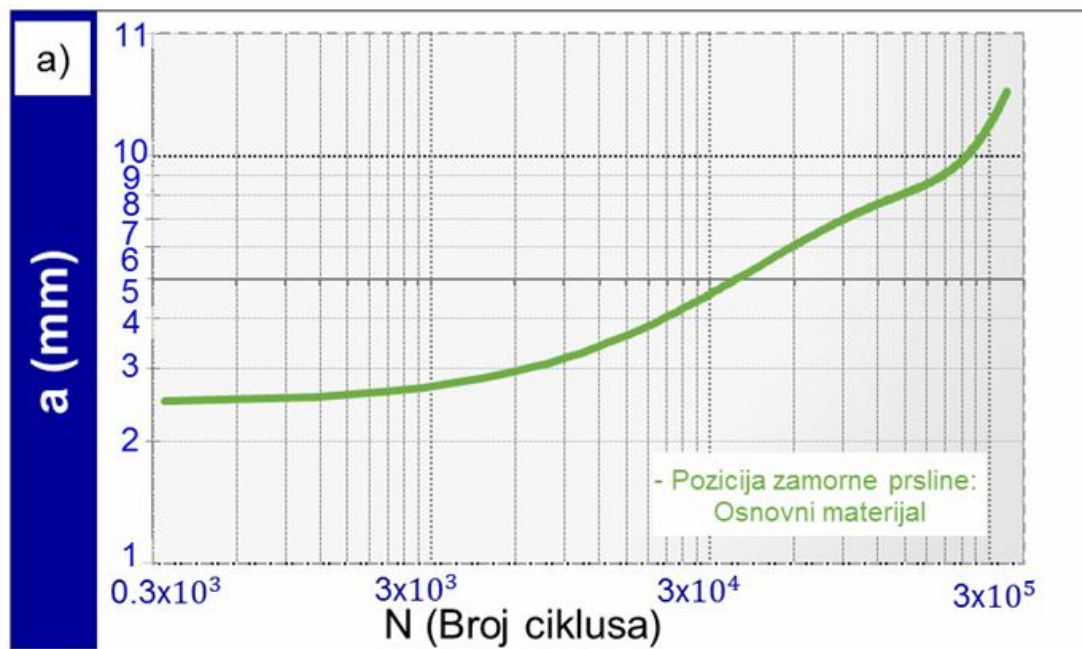


Figure 1.5. Crack length vs. number of cycles cure for a PM specimen [1.3].

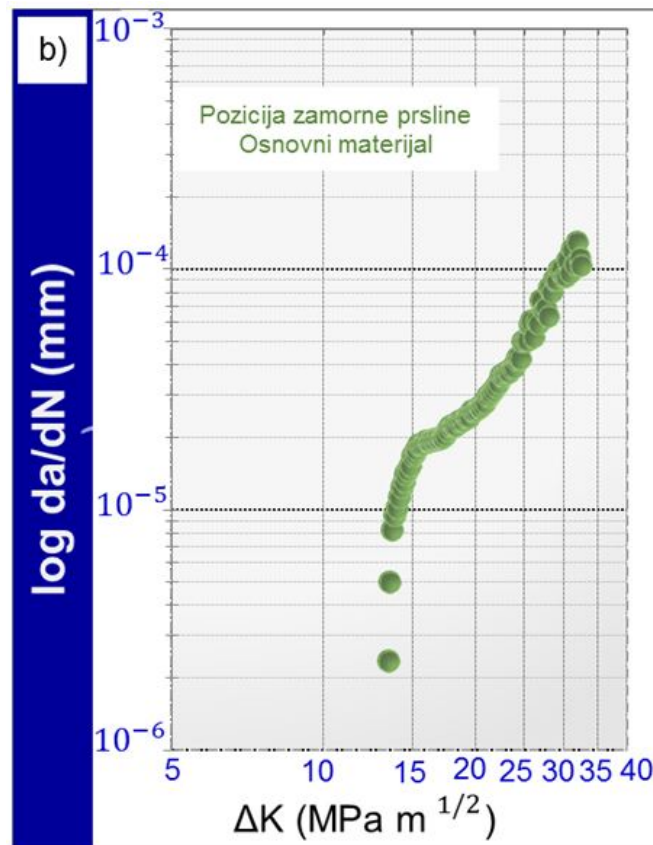


Figure 1.6. Crack growth rate – SIF threshold diagram for a PM specimen [1.3].

It can be seen from the above that C and m values can greatly vary even for specimens made of the same material, taken from the same plate, depending on the crack location, i.e. the microstructures through which it will pass during its propagation. Finally, Paris coefficients were also determined for specimens with the crack in the WM, following the same principles as the other cases, and their values were $C = 4 \times 10^{-11}$ and $m = 5.25$.

Based on the previously presented test results, it was concluded that the fatigue crack growth rate was highest in the WM, followed by the HAZ-WM combination, whereas it was lowest in the PM, as expected. Crack growth rate in the WM, i.e. the austenitic filler metal which was used in order to increase resistance to crack initiation, was much higher compared to the remaining region, due to significant stress concentration in this part of the welded joint.

This example was given with the goal of demonstrating the experimental procedure of testing of specimens with fatigue cracks, along with interpreting the results in terms of determining of Paris law coefficients C and m , which was also one of the main goals of this thesis. Additionally, other experiments which were similar to the ones that will be shown here were presented. Furthermore, the experimental approach to determining of Paris law coefficients was once again confirmed as a necessary step in such investigations.

2. FRACTURE MECHANICS

One of the fundamental requirements of any engineering structure is that it should not fail in service [2.1]. Several possible modes of failure must be considered in design. In addition to failure by environmental corrosion, the main modes of mechanical failure are:

- Failure after plastic deformation (yielding and necking),
- Failure by fast fracture (cracking),
- Fatigue failure (fatigue crack growth).

Plastic collapse is known as the failure mechanism of a tin can. In an ideally elastic/plastic solid which exhibited no work-hardening, complete plastic instability would occur in a simple tension test when the applied tensile stress overcomes yield strength. In general, this behavior is not observed in welded joints, because their capacity for work-hardening enables them to deform in a stable manner before failure. Only if a metal has been heavily cold-worked before testing will the onset of yielding immediately produce plastic instability (i.e. continuing deformation under constant load) and then only if the test is controlled by loading-rate (a soft testing system) rather than by displacement-rate (a hard system).

Early principles of structural design ensured that yield strength was nowhere exceeded in a structure, but later, it has become recognized that localized yielding can be permitted, if the large deformations of the total structure are prevented. This is of special importance for welded structures [2.1-2.4].

The engineer usually follows a design code which ensures that the calculable stresses in his structure shall nowhere exceed the material's yield strength, divided by an appropriate figure for the safety, or "ignorance" factor, is usually between 1.5 and 2, depending on the application, and, would compensate local enhancement of calculated stresses [2.5]. The safety factor applied to the material's yield strength can assist in the prevention of failure by general yielding: if higher applied stresses are to be put on a structure of given geometrical shape, material of higher uniaxial strength must be used.

Fast fracture is a failure mechanism which involves the unstable propagation of a crack. Once the crack has started to grow, the loading system is such that it produces accelerating growth. In the history of failure by fast fracture, it has almost always been produced by applied stresses less than the design stress. This has enhanced the catastrophic nature of the fractures and has led to the general description of them as brittle. The microscopic mechanisms by which the cracks propagate may be between low strain cleavage and intergranular fracture to fully ductile shear separation (in thin sheet). The engineering definition of brittle must be retained and it must refer to the onset of instability when the applied stress is less than the general yield stress [2.1, 2.16]. Although brittle fractures in steels occur particularly at low temperatures and in thick sections, disastrous fractures, 'brittle' in the engineering sense, are also possible in thin sheets. If a component is to fracture in a brittle manner (before general yield) it must contain a stress concentrator, because it is necessary to confine the cracking mechanism to a small region. For that it is interesting to know how the fracture can be produced ahead of a pre-existing crack or other stress concentrator.

Service failures of steel welded structures generally involve brittle fracture due to the presence of fabrication imperfections or even defects, or crack growth (e.g. fatigue cracks) in service. Ductile fracture is due to the growth of cracks to large, whereas plastic-collapse is a rare event. Ductile failure in the absence of crack-like defects is experienced only when accidental overloads exceed design stresses.

Complete elimination of small cracks is an unrealistic expectation for most structures, especially for complex welded structures. Modern design of steel structures is based on the combined use of classical design and structural integrity design. Classical design is used to size the structure, based on formulae and codes for material resistance. Structural integrity design is the basis for precluding structural failure, due to brittle fracture or premature fatigue, or corrosion cracking, or creep. In simple mechanical terms, classical design represents smooth-body design. Regions of geometric changes or notches are assumed to yield locally. Structural integrity design recognizes that tensile ductility can't protect cracked-body structures completely. The important factor for preventing fracture is sufficient crack-tip fracture toughness. Steels that feature low crack-tip ductility can develop fracture for conditions of relatively small cracks and low elastic stress levels. Conversely, steels of high crack-tip ductility can resist fracture for conditions of large cracks and high stress levels. Fracture-safe design is achieved by preventing fracture initiation from part-through (surface) cracks or by preventing fracture extension for through-thickness cracks. The primary structural integrity principles are:

1. Resolving fracture problems by fracture analysis, as a first step in design.
2. Reliable definition and control of the defect quality of the structure, to preclude premature initiation and growth of cracks.
3. Use of fracture mechanics analysis procedures and modeling to define crack-growth rates, if crack growth is of design interest.

Structural integrity design requires consideration of factors that determine structural performance. It includes service environment, structural function, metallurgical properties, fabrication quality, inspection requirements, quality control, and factors that are specific to weldments [2.6-2.7]. All of these factors interact with the fracture mechanics aspects because of their influence on crack size, stress and fracture properties. The knowledge and practical application of fracture mechanics are, for that, required in modern design.

Fracture mechanics test methods define the intrinsic resistance to the extension of brittle fracture for through-thickness cracked test specimens. Fracture mechanics provides the basis for calculating the stress required for brittle fracture initiation, due to the presence of any other crack-like defect of a particular size and geometry. Engineering extensions of fracture mechanics provide for defining stress-related fracture resistance for conditions of semi-ductile and ductile fracture by conservative simplifications. The practical design use of fracture mechanics is highly dependent on experience which was evolved by structural integrity technology specialists. Engineering experience in the safe design of structures and in failure analysis is an important aspect for all practical applications of fracture mechanics.

Structural failures are mainly the result of improper consideration or neglect of critical structural integrity design factors. Failure analyses for a wide variety of structures have provided statistical information about the relative importance of specific design factors for particular types of structures. For example, the primary reasons for the failure of weldments normally involve combinations of factors that are different from those generally responsible for the failure of castings and forgings. Structural failures by brittle fracture are always due to the presence or growth of fracture-critical cracks. Failure analyses in terms of fracture mechanics calculations of critical crack sizes document this fact as the mechanical reason for the failures, and in terms of metallurgical and fabrication factors disclose the engineering errors that resulted in the presence or development of the fracture-critical cracks. Evidence of brittle fracture, by visual examination of fracture surfaces, can confirm that the steel was fracture-sensitive at the temperature of service. However, most structures built of fracture-sensitive steels do not fail. Fracture initiation may result from the presence of cracks due to fabrication. Fracture initiation may also result from the development of fatigue cracks. This is the evidence that fatigue design aspects were not properly resolved, with consideration of the fracture-sensitivity of the steels. Fracture initiation may result from accidental damage. This aspect may

indicate that damage considerations were not included in design, if damage is normally expected. Fracture initiation may develop due to the presence of hard-brittle heat-affected zone (HAZ) in weld regions. This is evidence of inadequate specification of weld fabrication requirements and improper inspection. The relative simplicity of design adjustments that would have prevented structural failures is documented by experience in redesign of failed structures. Most cases of structural failures must be resolved by redesign of replacement structures. Usually adjustment of a single design factor provides the required solution.

The design phase is the point for considering structural integrity factors in technical and economic balance. The designer must rely on the advice of other specialists; the final decisions must be made at the design desk assuring the fracture-safe design.

2.1. Fundamentals of elastic-plastic fracture mechanics

It is almost impossible to analyze fracture phenomenon in many structural materials by linear elastic fracture mechanics because non-linear deformations ahead of the crack tip cannot be neglected. If so, it is better to crack opening displacement (COD) or *J-integral* as elastic-plastic fracture mechanics approach and parameters, since they describe behavior of elastic-plastic materials better than stress intensity factor, K [1]. When ahead the crack tip significant plastic zone is developed, it is not possible to describe stress state by single parameter, as it is critical stress intensity factor K_{Ic} , but events ahead the crack tip can be better described by COD or *J-integral* opened under tensile loading.

2.1.1. Crack opening displacement

Crack opening displacement is introduced by Wells in 1969 [2.8], as an empirical parameter, although based on derived formulae for v displacement component. Crack opening displacement (COD) can be used as a measure of fracture toughness of ductile materials. Ductile behavior is characterized by blunting of a crack. Two positions are used for COD definition: crack mouth opening displacement (CMOD), parameter measured on crack free surface, and crack tip opening displacement (CTOD), the value corresponding to distance, δ , of opposite sides of a crack tip in loaded components, that were at zero distance in unloaded situation

Many practical methods are developed for COD measurement or calculation, since it is convenient crack parameter for experimental and numerical analysis [2.17]. COD can be experimentally determined using standard specimens, single edge notched specimen for bending, SEN(B), and compact tension (CT) specimen. Numerical evaluation of COD is based on elastic-plastic approach by finite element method (FEM) analysis using singular finite elements around crack tip, initially sharp crack and its blunting under loading.

The plastic zone, surrounded by elastically deformed material causes the larger compliance of specimen, compared to the crack size. This effect is expressed by plastic zone radius r_y :

$$r_y = \frac{\alpha}{2\pi} \cdot \frac{K_I^2}{\sigma_Y^2} \quad (2.1)$$

With coefficient $\alpha=1$ for plane stress, and $\alpha=(1/3 \div 1/4)$ for plane strain condition. The plastic zone is small if surrounded by singular stress field described by stress intensity factor K_I ; otherwise, it is large. The term "general yielding" says that plastic zone extended through the thickness, up to opposite edge, and "full scale yielding" denotes total plasticity of the specimen.

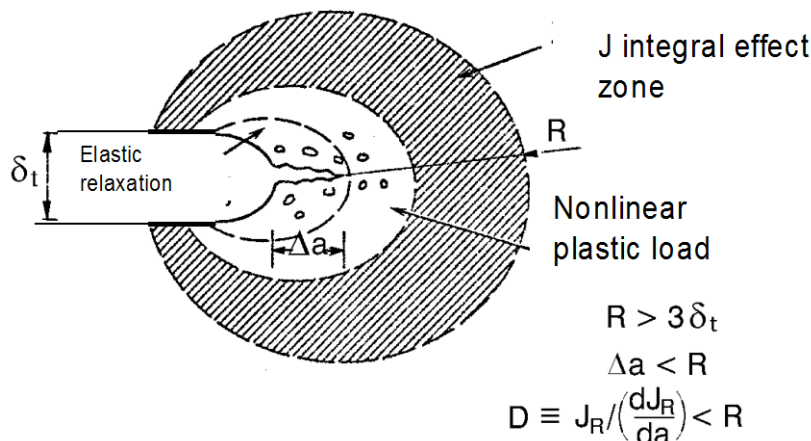


Figure 2.1. The *J-integral* effect and fracture process zone [2.15]

HRR zone (Hutchinson-Rice-Rosengren) size is defined by radius R . In this zone stress-strain state is described by J -integral as fracture mechanics parameter. Radius D defines process zone; it is usually small and comparable with initial crack opening displacement, Fig. 2.1.

Crack opening displacement (COD) can deliver the answer to question if for known crack size the residual ligament is sufficient for general yielding before fracture or not. If the opposite edge is close to crack tip, plastic zone will develop in the ligament before critical COD (δ_c) is achieved. If not, the fracture will be brittle. In both cases COD can reach the same value. For plane stress and tensile stress, Cottrell defined COD in the form:

$$\delta_c = \frac{8R_{eh}a}{\pi E} \ln \left[\sec \left(\frac{\pi \sigma_{cr}}{2R_{eh}} \right) \right] \quad (2.2)$$

With σ_{cr} as stress at fracture, and R_{eh} as yield strength. Critical value of COD (δ_c) corresponds to crack initiation and it differs from the value of unstable crack growth.

2.1.2. Rice's contour integral

Theoretical background of path independent J -integral, introduced by Rice in 1968 [2.9] as energy parameter, enabled its application in the elastic plastic regime, as well as in the elastic regime, making it the most useful fracture mechanics parameter. By definition J -integral is given as:

$$J = \oint_{\Gamma} \left(W dy - T_i \frac{\partial u_i}{\partial x} ds \right) \quad (2.3)$$

With $W = \int \sigma_{ij} d\varepsilon_{ij}$ - strain energy density; Γ - integration path; ds - element of segment length; $T_i = \sigma_{ij} n_j$ - traction vector on the contour; u_i - displacement vector, Fig. 2.2.

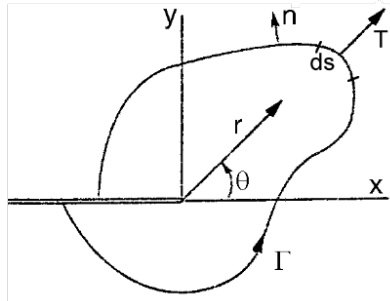


Figure 2.2. Contour path of J -integral

Rice has shown that J -integral is path independent if necessary conditions are fulfilled. This is required for its calculation, because its value is the same for the contours close to the crack tip, for contours outside plastic zone as well as for path along specimen sides.

J -integral can also be presented as the energy, released on crack tip for unit area crack growth, Bda , by following expression

$$JBda = B \oint_{\Gamma} W dy da - B \oint_{\Gamma} T_i \frac{\partial u_i}{\partial x} ds da \quad (2.4)$$

Here B is the specimen thickness. The member $B \oint_{\Gamma} W dy da$ denotes the energy obtained (and released) along the contour Γ for crack increase, da , for non-linear elasticity. Second member represents the work of traction forces on contour displacement for crack extension da . The value $JBda$ is total energy at crack tip available for crack growth Δa , equal to the value G :

$$J = G = \frac{K^2}{E'}; \quad E' = E \text{ for plane stress; } E' = \frac{E}{1-\nu^2} \text{ for plane strain} \quad (2.5)$$

In plastic region, W is not strain energy density, being dissipated inside the material, so J is not the energy at the crack, available for crack growth.

To have J -singular field around the crack tip, some requirements have to be fulfilled. Ahead the crack tip there is a region, called "fracture process zone", in which material is significantly deformed, with occurrence of voids, slip lines and other forms beyond the continuum mechanics application, Fig. 2.3. The size of process zone could be small compared to body dimensions; for plane strain condition process zone must be small compared to specimen thickness, as experimentally proved, in general as

$$B, b, a < 25 \frac{J}{\sigma_o} \quad (2.6)$$

Where $b = W - a$ stands for specimen ligament.

2.1.3. The application of J-integral to crack initiation

The behavior of elastic-plastic material during stable crack growth can be described by the relationship between fracture mechanics parameter (K , COD, J -integral) vs. crack extension, Δa , Fig. 2.3. In brittle fracture no energy is spent for crack growth, and corresponding relation for J - Δa is given by horizontal straight line, that intersects the ordinate at the level J_{Ic} . This level corresponds to critical energy consummation for crack initiation. For ductile material, in initial stage of load increase and energy release, deformation is expressed by increase of existing crack opening, but not with its extension. This corresponds to steep line in J - Δa relationship, representing crack tip blunting stage. In critical point the slope of the line is changed, because next crack opening increase is connected with crack extension and its length increase [2.10]. Point of deflection in the initial stage is taken as J_{Ic} , a measure of fracture toughness. It is possible to calculate, based on this value, the value of critical stress intensity factor (plane strain fracture toughness), K_{Ic} .

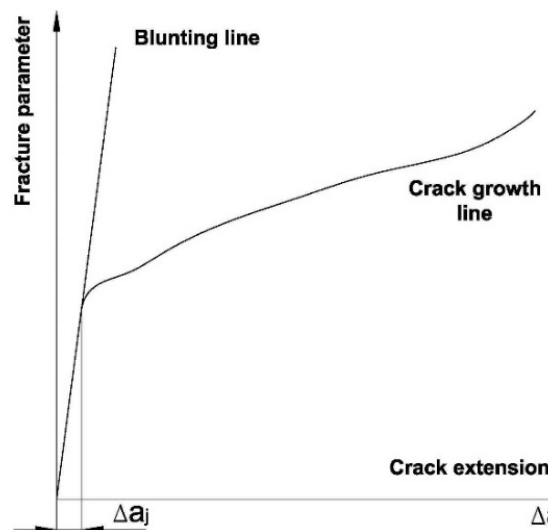


Fig. 2.3. Crack growth resistance curve (R -curve)

It can also be seen in Fig. 2.4 that CTOD can be used for description of material behavior in the crack tip region, so the point B can be expressed by $(CTOD)_{cr}$ as well. For elastic-plastic materials CTOD can be related to J -integral:

$$\delta = \frac{J}{mR_e} \quad (2.7)$$

Where m is a coefficient, with the value between 1 and 2.6; lower values correspond to plane stress and ideal plasticity, and higher values to the plane strain.

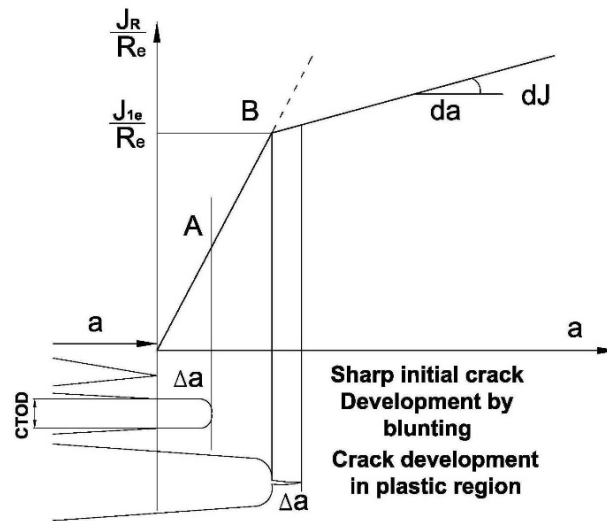


Figure 2.4. Scheme of stable crack growth

2.2. FATIGUE

2.2.1. Material resistance under variable loading (fatigue)

A century ago structural design was based on concepts of static strength only. This was adequate since there were few sources of repetitive stressing than today, and parts were designed with large safety factors. With the development and use of power machinery, unexplainable failures of ductile materials well below the tensile strength, but exhibiting no gross plastic deformation, arose and were ascribed as “fatigue”. They usually occurred after long time of service. Later experiments showed that important factor is stress repetition, and not time, and that “fatigue failures” are “repeated stress failures.” Improvements in design require components to operate at high levels of both static and repeated stress; resist of fatigue is a major concern, as it is the most common cause of service failure.

Fatigue failures are characterized by very small plastic flow, and are transgranular as compared to intergranular which is typical for stress rupture failures. The fatigue process may be divided into three main stages: crack initiation, crack propagation to critical size, and unstable fracture of the remaining section [2.11]. The crack initiated at a surface flaw or stress concentration, and spread during cycling until the section is sufficiently reduced for a final tensile fracture to occur. The second stage region, propagation, has a flat surface and frequently has markings which focus on the origin or nucleus of failure. The third stage region has a more jagged texture representing a tensile fracture. Many fatigue tests of metals have provided the following general behavior of metal structures:

- Failure at much lower than the ultimate tensile stress occurs in most metals that exhibit ductility in static tests, and the magnitude of alternating stress range is the controlling fatigue life parameter.

- Failure depends upon the number of repetitions of a given range of stress rather than the time under load. The loading rate is of lower importance except at elevated temperature.

- Most metals have a safe range of stress, called the “endurance or fatigue limit,” below which failure does not occur irrespective of the number of stress cycles.

- Notches, grooves, or other discontinuities of section, producing stress concentration, including those associated with surface finishes greatly decrease the stress range that can be sustained for a given number of cycles.

- The range of stress necessary to produce failure in a fixed number of cycles usually decreases as the mean tension stress of the loading cycle is increased.

Fatigue failure involves the cumulative effect of numerous small-scale events taking place over many cycles of stress and strain and under various service environments. In Table 2.1 fatigue data for design are given for the nomenclature, depicted in Fig. 2.5.

Table 2.1. Nomenclature for fatigue loading cycle (Fig. 2.5)

Stress cycle	The smallest section of the stress-time function, repeated periodically and identically
Nominal stress, σ	The stress calculated by simple theory without taking into account variations in stress due to geometry, such as holes, grooves, fillets
Maximum stress, σ_{max}	The highest algebraic value of stress in the cycle
Minimum stress, σ_{min}	The lowest algebraic value of stress in the cycle
Stress range, σ_r	The algebraic difference between the maximum and minimum stress in one cycle, $\sigma_r = \sigma_{max} - \sigma_{min}$
Alternating stress amplitude, σ_a	One half the stress range, $\sigma_a = \sigma_r/2$
Mean stress, σ_m	The algebraic mean of the maximum and minimum stress in one cycle, $\sigma_m = (\sigma_{max} + \sigma_{min})/2$
Stress ratio, R	The algebraic ratio of the minimum stress to the maximum stress in one cycle, $R = \sigma_{min}/\sigma_{max}$
Stress ratio, A	The algebraic ratio of the stress amplitude to the mean stress, $A = \sigma_a/\sigma_m$
Stress cycles, n	The number of cycles endured at any stage of life
Fatigue life, N	The number of stress cycles which can be sustained for a given condition.
σ - n diagram	A plot of stress, σ , versus number of cycles to failure, n
Endurance limit, σ_E	The value of stress below which a material can presumably endure an infinite number of cycles. This is the stress at which the σ vs. n diagram becomes horizontal or asymptotic thereto

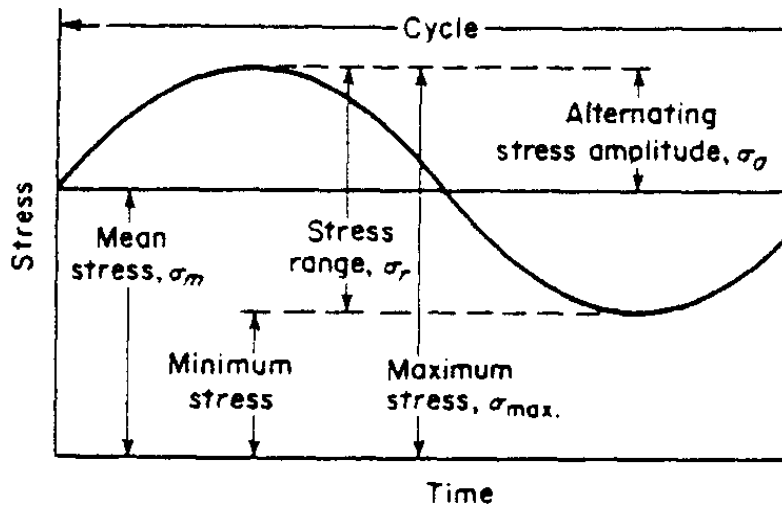


Figure 2.5. Fatigue cycle nomenclature

There are several methods of applying the load in endurance testing. The specimen may be subjected to direct tension and compression, to bending, to torsion or to their combination. The simplest, and most frequently used method, is the rotating reversed bending test. This consists of applying a load at the end of a standard cantilever fatigue test specimen which is rotated at constant rate, thereby creating full reversed bending stresses with each revolution. Data from such tests are usually reported as stress σ vs. number of cycle's n curves, Fig.2.6, usually plotting σ_{max} against $\log n$. In this manner the endurance limit is disclosed by a definite break in the curve. At the beginning σ_{max} decreases rapidly with increase in n , then the curve approaches asymptotically a stress value which shows no further decrease with increase in number of cycles; a value at which an unlimited number of cycles can be endured without failure. This is the endurance limit, σ_E . The endurance limit of ferritic steels in air at room temperature is reached at $10^6 \sim 10^7$ cycles.

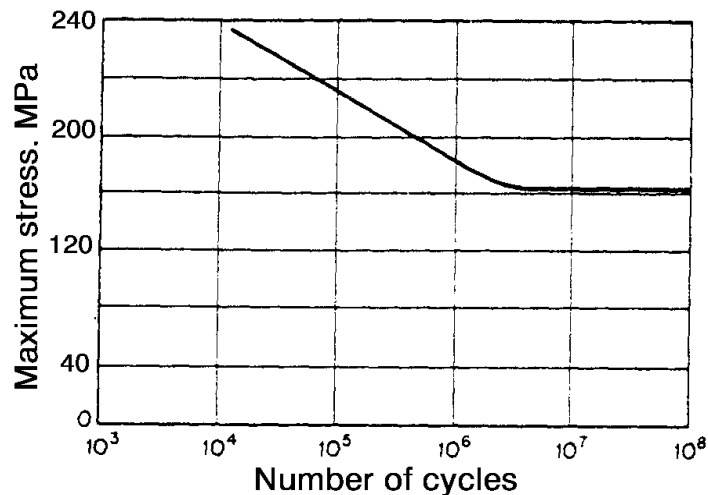


Figure 2.6. Typical σ vs. n diagram

2.2.2. Fracture mechanics analysis of fatigue

Crack growth caused by variable loads below the quasistatic failure load levels is referred to as material fatigue [14]. Majority of damages and failures of installation parts and structures during exploitation is a result of fatigue. More often than not, these damages can be attributed to the state of the material, but a lot of them are still a consequence of poor design choices, mainly related to low quality welded joints. This suggests that the tendency towards fatigue of a part of a machine or structure or a welded joint does not only depend on its material fatigue strength, but also on its geometry. Thus, when tasked with increasing the durability of a machine or structure in terms of

fatigue, it should be taken into account that simply selecting the most fatigue resistant materials is not enough, and is more often than not an inefficient solution, wherein new and improved design solutions represent a better alternative.

An example which will be considered here will involve fatigue crack growth for a constant K -threshold, ΔK , as shown in Fig. 2.7. This type of load is only of academic significance since it never occurs in exploitation conditions. It is, however, interesting during experiments and can be achieved using computer controlled pulsator. It should be noted that the invariability of range ΔK during crack growth does not necessarily imply the invariability of load F (P), or of displacement V_p . Quite contrary, in order to achieve such load, it needs to be decreased in a certain manner during crack propagation.

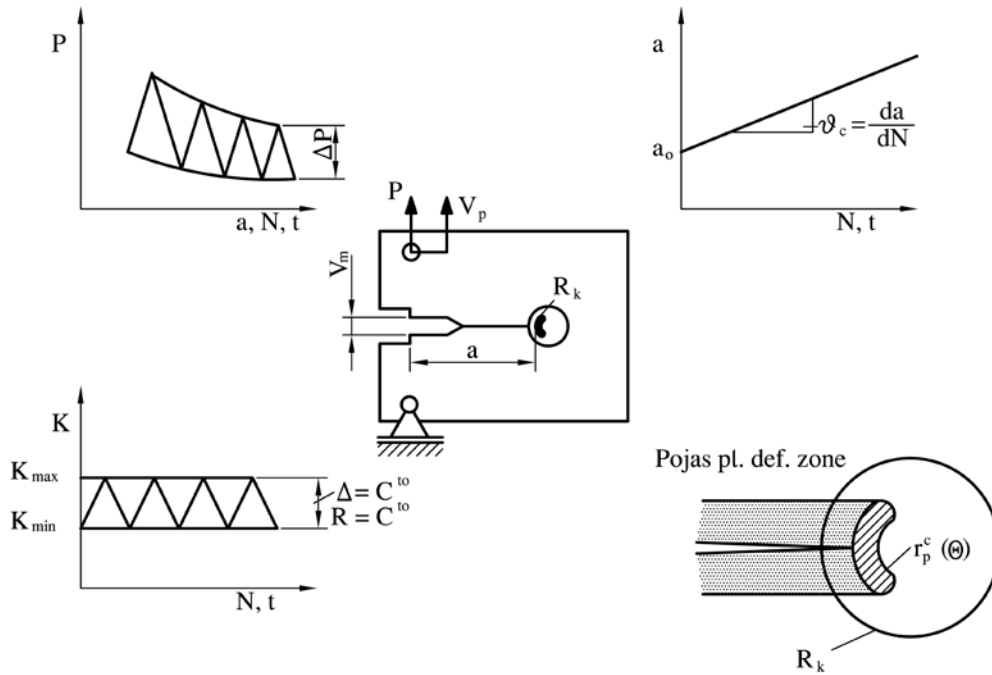


Figure 2.7. Linear crack growth with $\Delta K = \text{const.}$ and small scale yielding $r_p^c \ll R_k$

Since each fatigue cycle forms a corresponding plastic zone ahead of the crack tip $r_p^c(\theta)$, crack propagation constantly leaves a region of plastically deformed material in behind its tip, Fig. 2.7. If the plastic zone $r_p^c(\theta)$ is within a K^* -dominant singularity zone R_k , the small-scale yielding condition is fulfilled, $r_p^c(\theta) < R_k$, thus the value of K -factor for the considered fatigue cycle uniquely describes the stress field at the tip of the current crack. It follows that the crack growth rate da/dN can be expressed as

$$\frac{da}{dN} = f_1(\Delta K, R) \quad (2.8)$$

Where $\Delta K = K_{max} - K_{min}$, is the stress range of the K -factor, and $R = K_{max}/K_{min}$, is its stress ratio.

Since the size of the plastic zone only depends on K_{max} and K_{min} , it follows that the previous expression explicitly takes into account the effect of the plastic zone and the accompanying plastic belt on crack growth rate. It should be emphasized that the influence of various loads on crack growth rate da/dN excludes the application of this concept on similar behaviors. Namely, two configurations made of the same material, subjected to fatigue with same value of ΔK and R will show the same crack growth rate da/dN only if their previous load levels were the same. Fatigue crack growth is a very complex process which depends on a number of variables such as:

- Effective stress intensity factor at the crack tip, defined by the K -factor;

- Type and form of load;
- Working environment (aggressiveness, temperature, humidity);
- Mechanical and metallurgical properties of the material

The need to introduce fracture mechanics to studying of fatigue behavior resulted from crack growth rate analysis during cyclic loading.

Literature contains numerous theoretical and empirically defined dependencies in the form of $da/dN = f(F, a)$, which emphasize the importance of load and crack length. The first and basic parameter which controls fatigue crack growth rate was defined as shown in the equation below:

$$\Delta K = K_{max} - K_{min} = Y(\sigma_{max} - \sigma_{min}) (\pi a)^{1/2} = Y\Delta\sigma (\pi a)^{1/2} \quad (2.9)$$

If $\sigma_{min} < 0$, K_{min} is adopted as 0, since the K -factor does not exist in the case of compressive stresses. Crack growth rate da/dN as a function of ΔK is determined from the corresponding $a-N$ curve. Experimental results are shown on a double-logarithmic scale and are characterized by their S-shape, schematically given in Fig. 2.8:

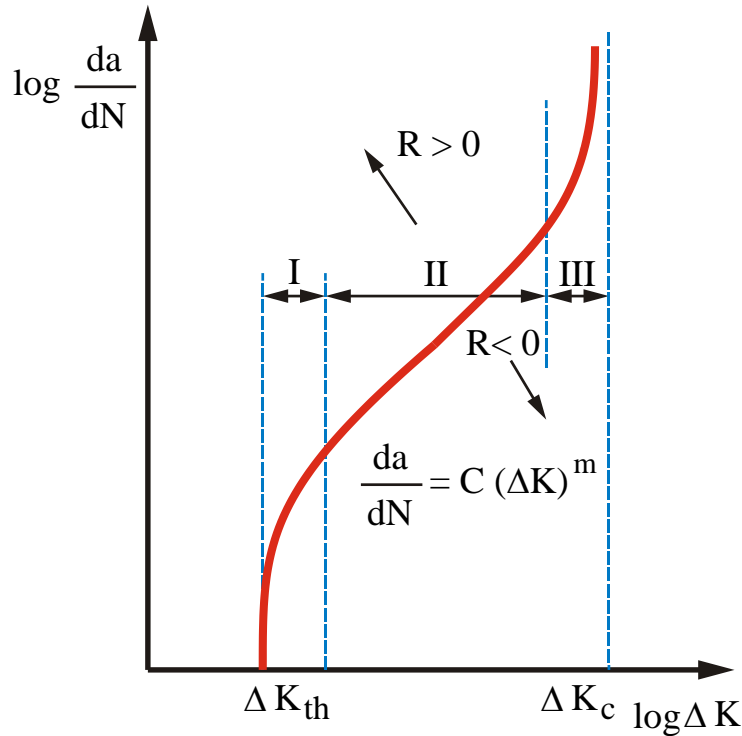


Figure 2.8. Crack growth rate da/dN for $R = 0$ and the position of the S-curve for $R \neq 0$

From the standpoint of crack growth rate mechanism and various influential factors, three regions can be observed on this curve. In region I, the decrease of ΔK leads to a noticeable decrease in crack growth rate. ΔK value for which these rates are around 10^{-10} m/cycle or less defines the sensitivity threshold for the stress intensity factor range, the fatigue threshold, ΔK_{th} . Below the ΔK_{th} , fatigue cracks behave without a tendency towards propagation. In region II, the dependence of $\log(da/dN)$ from $\log \Delta K$ is essentially linear and represented by a straight line which Paris et al [19] had described using the following shape function, [2.12]:

$$\frac{da}{dN} = C \cdot (\Delta K)^m \quad (2.10)$$

In region III, there is a sudden increase in crack growth rate, before the final failure occurs. This apparent instability is related to K -factor maximum value K_{max} approaching its critical value, K_{Ic} , for a given material, which is related to the early stages of brittle fracture. This possibility is prominent in high strength materials with low fracture toughness, where tensile specimen dimensions enable linear-elastic behavior even at K -factor levels close to the fracture toughness K_{Ic} , under plane strain.

Application of the Paris equation was found particularly fruitful in the field of WM and welded joint fatigue. Unlike homogeneous materials, the total number of cycles until failure of a welded joint is generally determined by crack growth rate. The reason for this lies in the geometrical non-homogeneity of welded joints and in the existence of sufficiently small surface roughness in forms of intrusions or slag inclusion with depth no greater than 0.02 – 0.04 mm, especially in the transition between the WM and the PM.

Based on the previously presented analysis of factors which affect fatigue crack growth, it can be seen that, in addition to stress range ΔK , crack growth rate is also affected by other mechanical, geometrical and metallurgical factors, along with the environment. Thus, it is impossible to provide a simple analytical form to describe how all these factors affect fatigue crack growth. Up to this point, however, a number of empirical, semi-empirical or purely theoretical models for fatigue crack growth rate prediction were developed, but they are all characterized by only being applicable to a certain range of ΔK , for specific materials and testing conditions.

Paris equation, represented by equation (2.11), where C and m are material constants, only holds in region II of crack growth (Fig. 2.8), and for a single value of stress ratio $R = K_{max}/K_{min}$. Since crack growth lines in region II for different values of R are almost parallel (Fig. 2.8), their m values will be practically the same, but coefficients C will differ, what can be simply presented as:

$$\frac{da}{dN} = \frac{C_v}{(1-R)^{n_v}} (\Delta K)^{m_R} \quad (2.11)$$

Where C_v and n_v are coefficients determined for $R = 0$. Equation (2.12) was modified by Vaker [2.13], by replacing:

$$K_{max}^{n_v} = \left[\frac{\Delta K}{(1-R)} \right]^{n_v} \quad (2.12)$$

into it, obtaining the following:

$$\frac{da}{dN} = C_v \cdot \Delta K^{m_R - n_v} \cdot K_{max}^{n_v} = C_v \cdot \Delta K^{m_v} \cdot K_{max}^{n_v} \quad (2.13)$$

Where $m_v = m_R - n_v$

Forman et al [2.14] proposed the following expression:

$$\frac{da}{dN} = \frac{C_F (\Delta K)^{m_F}}{(1-R) \cdot K_{Ic} - \Delta K} = \frac{C_F (\Delta K)^{m_F - 1} K_{max}}{K_{Ic} - K_{max}} \quad (2.14)$$

This, in addition to R , includes the effect of quick failure when K_{max} approaches fracture toughness, K_{Ic} . Such behavior is typical for high strength metals with low toughness, where fatigue crack growth test specimens size allows linear-elastic behavior even at K -factor levels close to K_{Ic} .

3. EXPERIMENTAL RESEARCH

In the scope of experimental research tensile testing, Charpy toughness testing as long as Fatigue and Fracture mechanics testing have been performed. Due to the small amount of available testing material all experimental tests have been done on small specimens like Charpy dimensions. Testing was done using the steel 15NiMoCrB4-5 with the following composition, Table 3.1.

Table 3.1. Chemical composition of the investigated material, mass %

C	Si	Mn	P	S	Cu	Al	Cr	Mo	Ni	Nb	N
0,109	0,314	0,828	0,011	<0,00 1	0,251	0,082	0,466	0,469	1,009	0,006	0,001

3.1. Tensile tests

Tensile specimen is shown in Fig. 3.1.

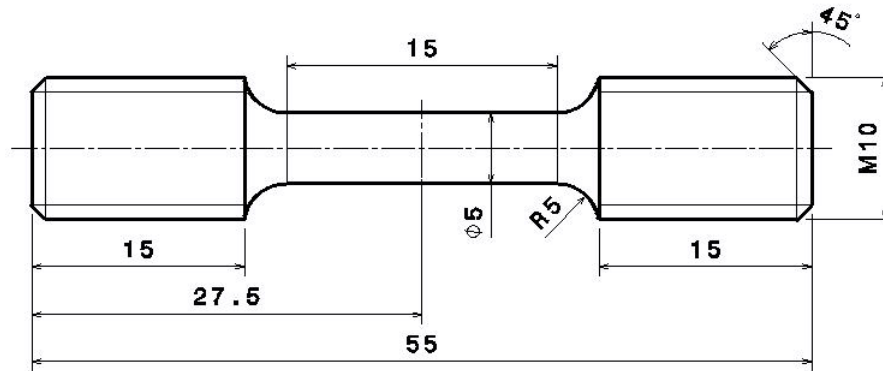


Figure 3.1. View and dimensions for tensile test specimen

Broken specimen form welded joint is shown in Fig. 3.2 where is obvious that the break occurs in PM. Tests were done on Shimadzu electro-mechanical testing machine with load capacity of 100 kN, Reduced diameter was 5 mm and gage length of 15 mm. Tests were done using velocity of 0.2 mm/min. Tests were supported with commercial software for data evaluations. After test was finished results were given tabular and with usual diagrams. Problem by used software is proper definition of linear part in order software to evaluate data rezeriod procedure giving starting point zero load F_0 versus zero elongation Δl . Test data were available in digital form so it was possible to redefine linear part of elastic deformation and rezeriod procedure was done using Excel program.



Figure 3.2. The end of tensile test with broken specimen positioned in the testing jig

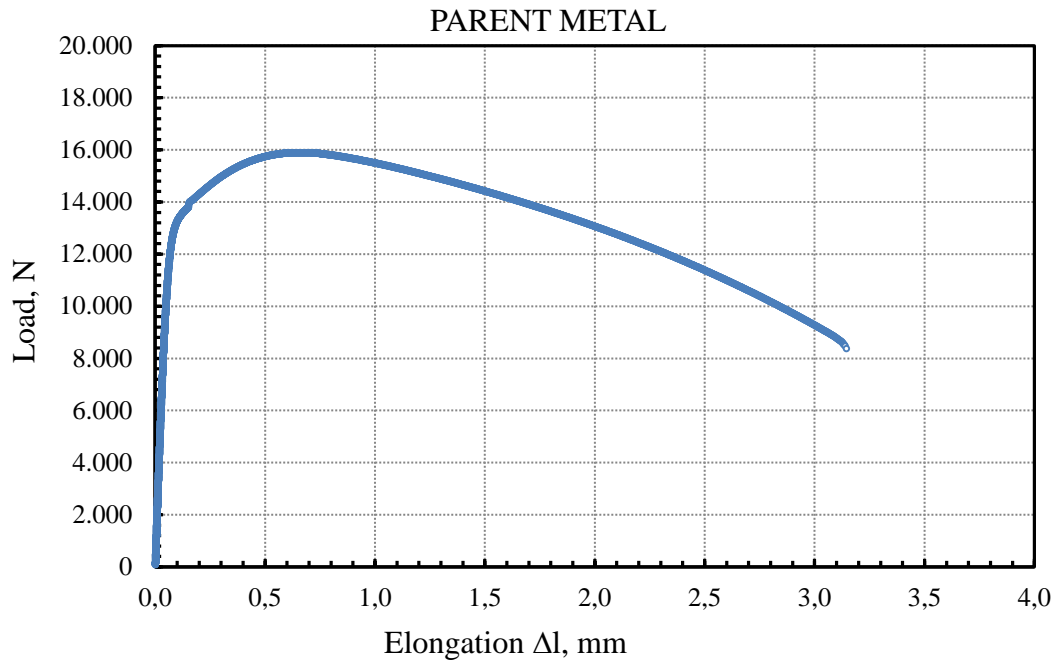


Figure 3.3. Typical diagram of load – elongation for PM specimen

In some cases procedure is not done properly by software, especially if testing new non well known material, and this has to be done manually. From the diagram load – elongation one can choose proper data points which give us possible better linear part. By introducing the linear trend line it is possible from the equation obtained elongation difference make correction to all elongation data forcing the zero point for elongation for zero loads.

Such correction for this test it is not necessary to do because software produces correct rezeroid procedure. Example for such rezeroid procedure is shown in Fig. 3.3.

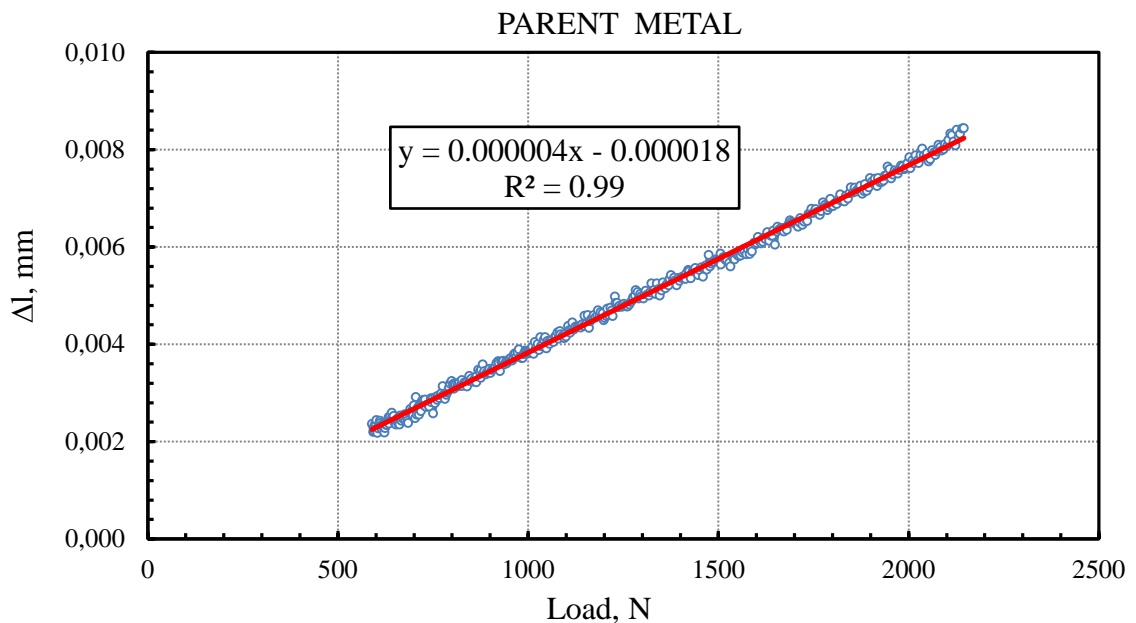


Figure 3.4. Diagram for manual rezeroid procedure

Engineering stress-strain is calculated for specimen diameter of 5 mm and gage length 15 mm and presented on the Fig. 3.4. By taking the data points from linear part of engineering stress – strain curve it is possible to get modulus of elasticity E which is shown on Fig. 3.5. From the diagram it is

possible to see that there is relatively big data scatter probably for not so good extensometer with large measuring capacity for small gage length of 15 mm. To reduce data scatter it is needed extensometer with possibly changing measuring capacity. By taking the data points from linear part of engineering stress – strain curve it is possible to get modulus of elasticity E which is shown on Fig. 3.5.

From the diagram it is possible to see that there is relatively big data scatter probably for not so good extensometer with large measuring capacity for small gage length of 15 mm. To reduce data scatter it is needed extensometer with possibly changing measuring capacity.

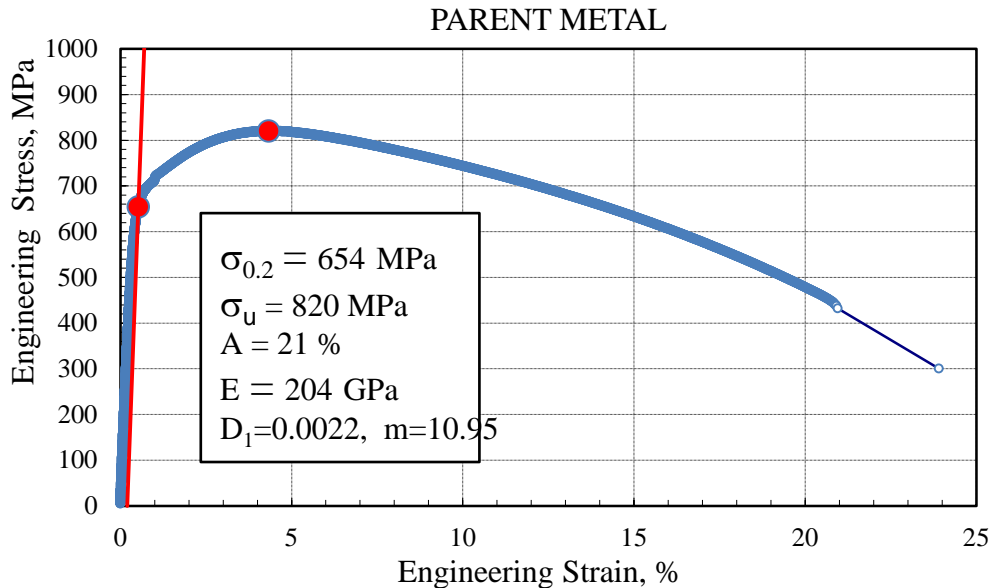


Figure 3.5. Engineering stress – strain curve for specimen made of PM

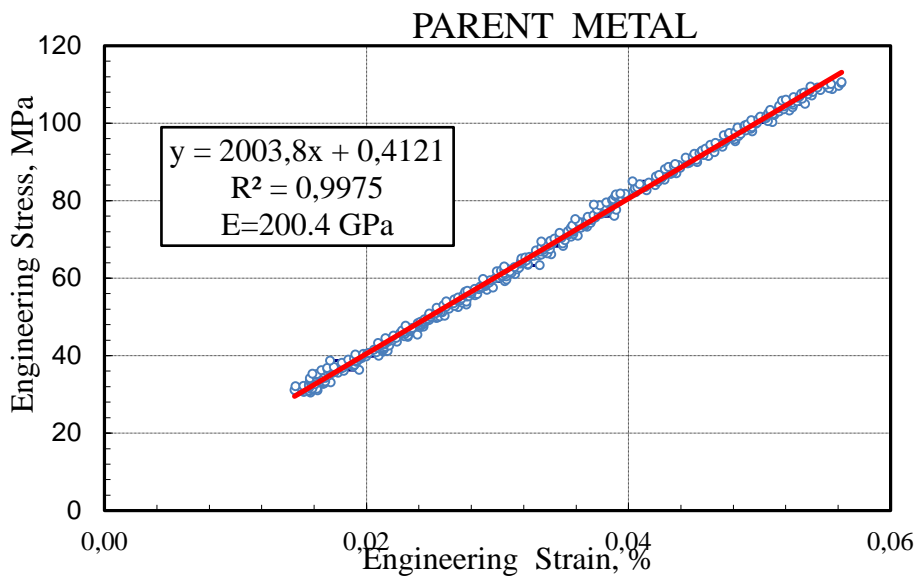


Figure 3.6. Modulus of elasticity obtained from PM tensile test

Yield strength is $\sigma_{0.2} = 654$ MPa and ultimate strain $\sigma_u = 820$ MPa with the value of the break elongation $A = 21\%$. Modulus of elasticity is expected value of $E = 200.4$ GPa close to theoretical values of $E = 210$ GPa. Parameters D_1 and m defined in Ramberg – Osgood relationship expressed true stress – strain between points of yield point and maximum load are $D_1 = 0.0022$ and $m = 10.95$:

$$\varepsilon_{true-plastic} = D_1 \left(\frac{\varepsilon_{true}}{\varepsilon_{0.2-true}} \right)^m \quad (3.1)$$

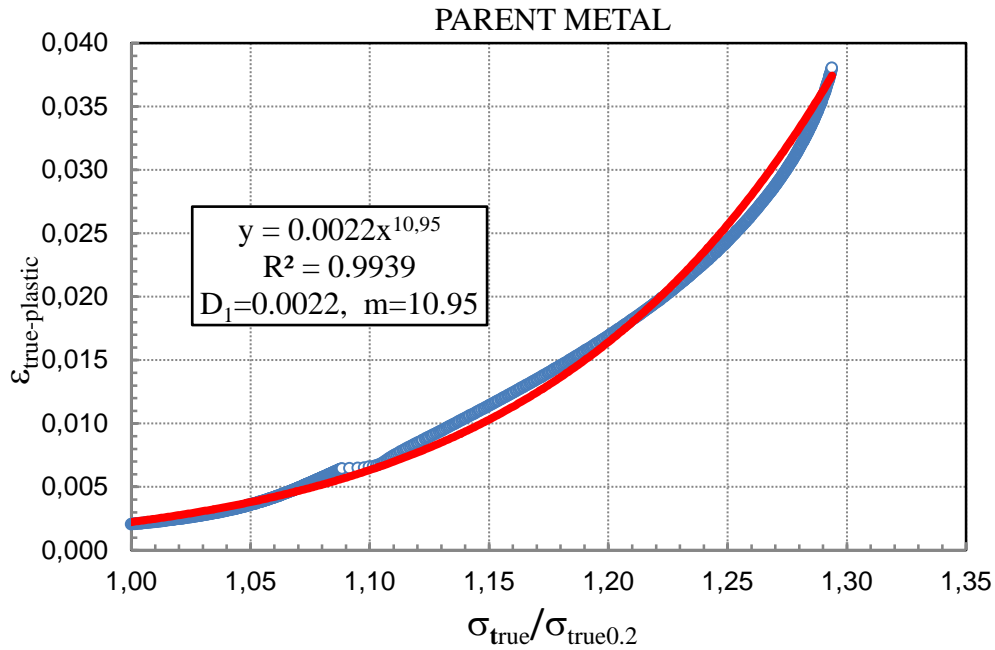


Figure 3.7. Typically Ramberg – Osgood curve for true plastic deformation for PM

In the same way were produced tensile specimens for welded joint, the relationship load – dilatation is given in Fig. 3.7. Yield strength for welded joint at 0.2% deformation is $\sigma_{0.2} = 768$ MPa and ultimate strength of welded joint is $\sigma_u = 837$ MPa, Both points are shown in Fig. 3.8 with blue points. Ramberg – Osgood relationship is different for welded joint with very bad power line fit but with perfect fit using polynomial curve of third order.

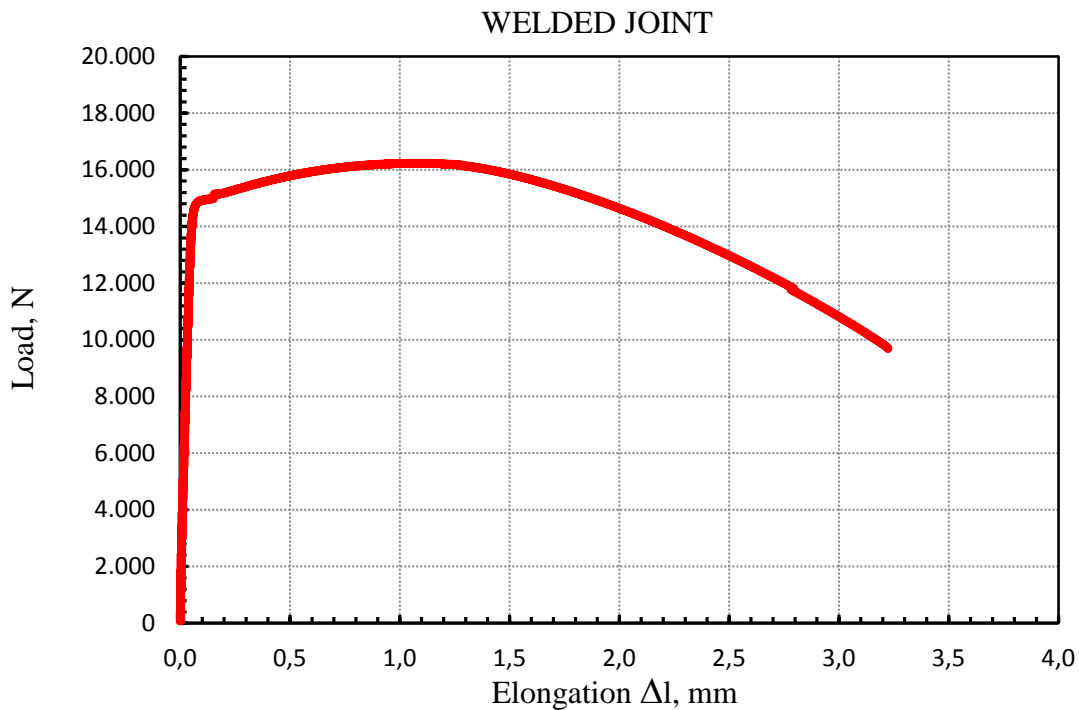


Figure 3.8. Diagram of load – elongation for weld joint specimen

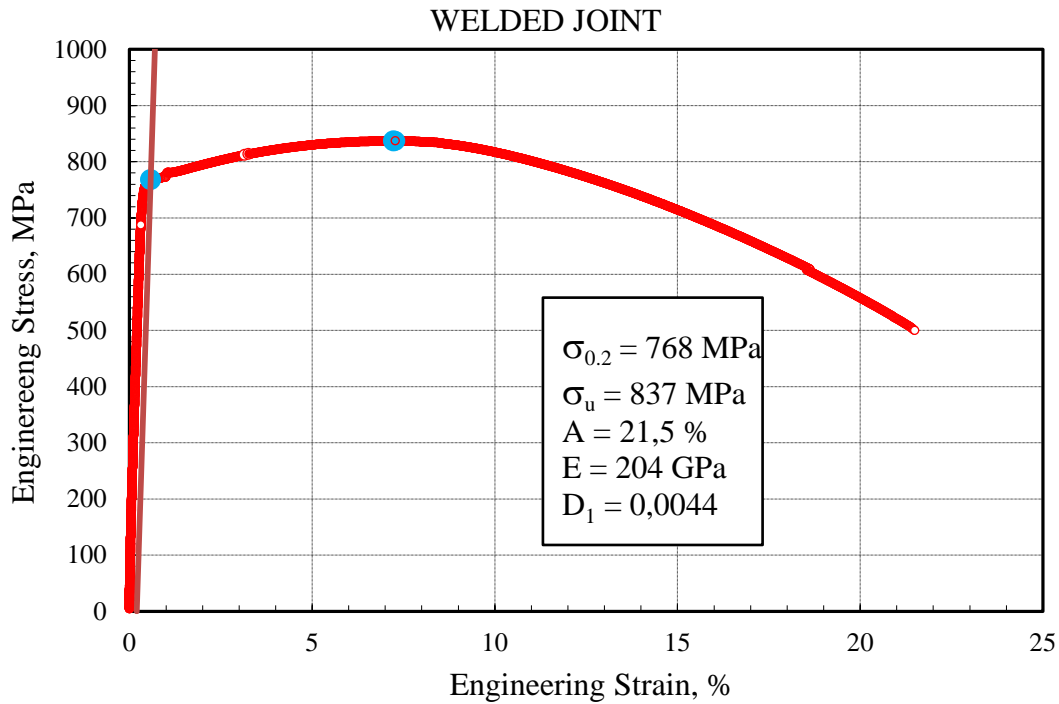


Figure 3.9. Engineering stress – strain curve for specimen made of weld joint

To get better view of base metal and welded joint curve both curves are shown together in Figs. 3.10 and 3.11. Comparing the yield points one can conclude that weld joint is over-matched expressed thru yield points. Matching factor is defined as quotient of yield point of WM and base metal given as:

$$M = \frac{\sigma_{0,2 \text{ weld metal}}}{\sigma_{0,2 \text{ base metal}}} \quad (3.2)$$

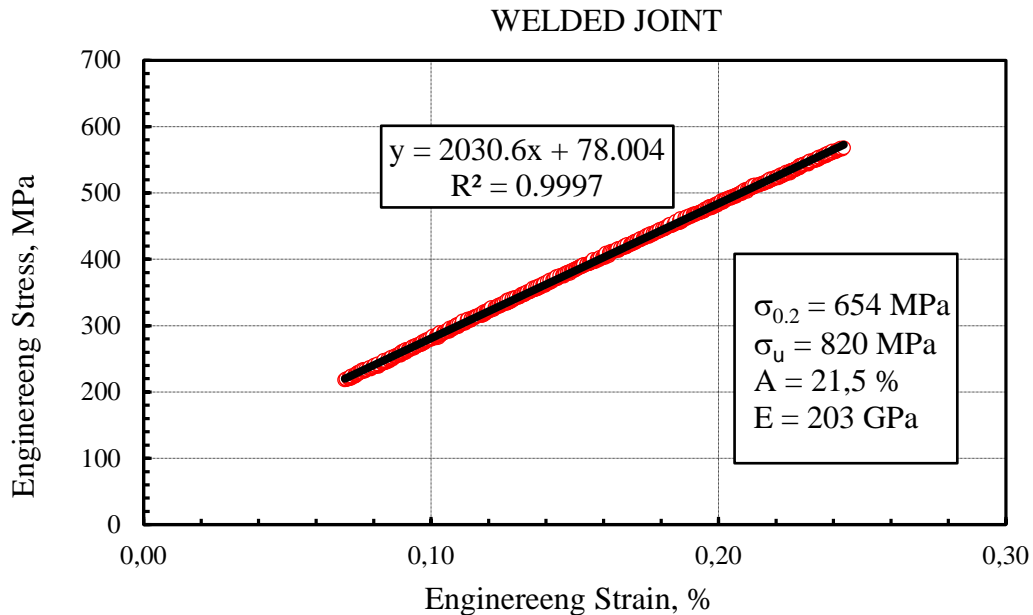


Figure 3.10. Modulus of elasticity obtained on WM tensile test

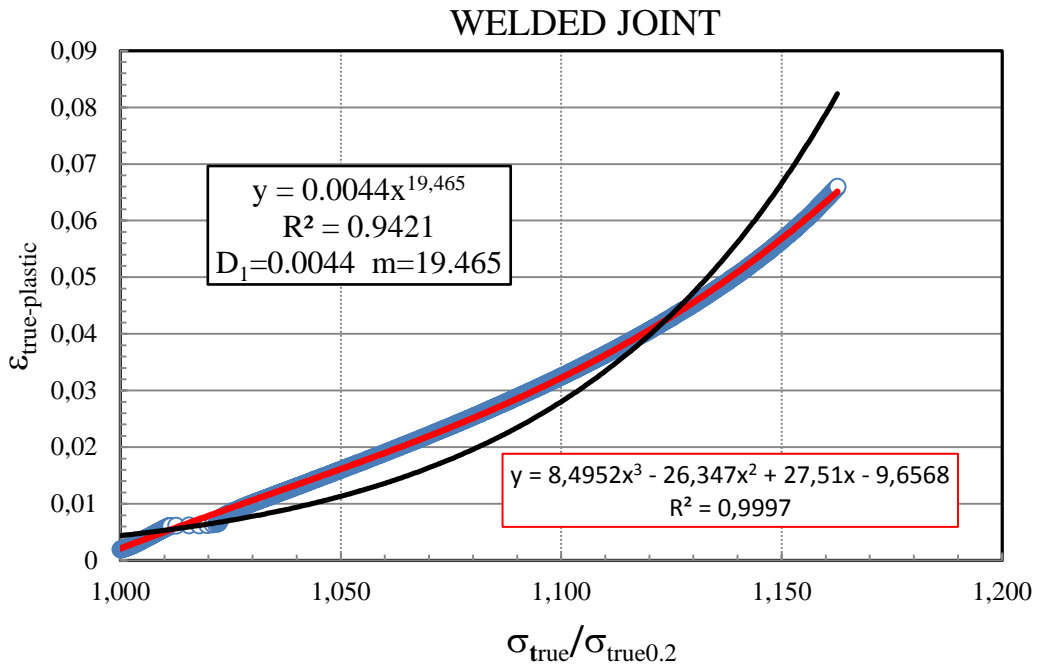


Figure 3.11. Ramberg – Osgood curve for true plastic deformation of the welded joint

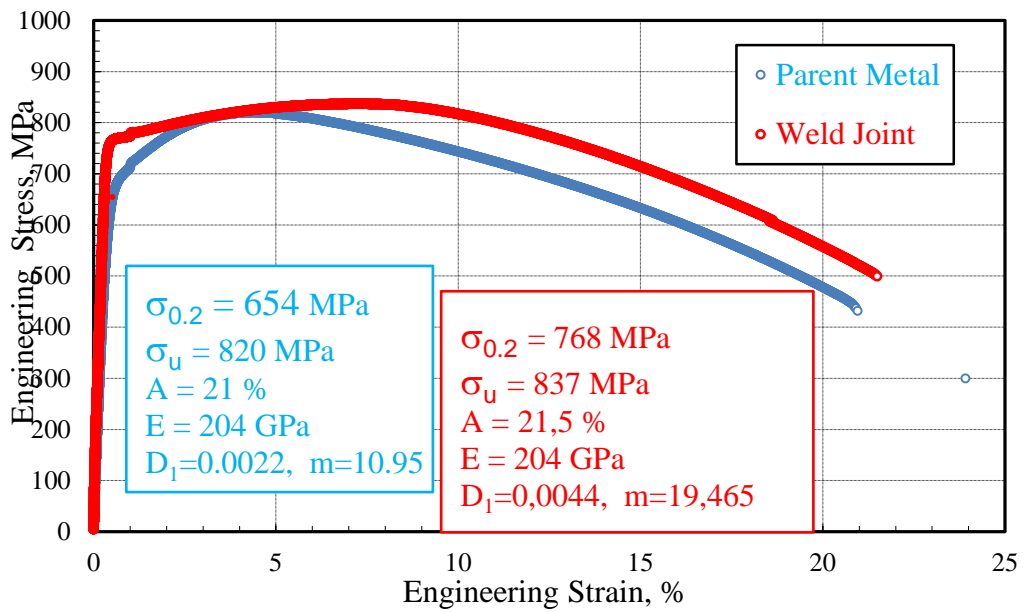


Fig. 3.12. Tensile properties for both specimens are similar.

3.2. CHARPY testing

The Charpy tests have been done on three specimens representing all weld joint constituents: PM, WM and HAZ. One can see from Fig. 3.13-3.19 that PM has the highest toughness, than come HAZ, whereas WM is the most sensitive to impact loading.

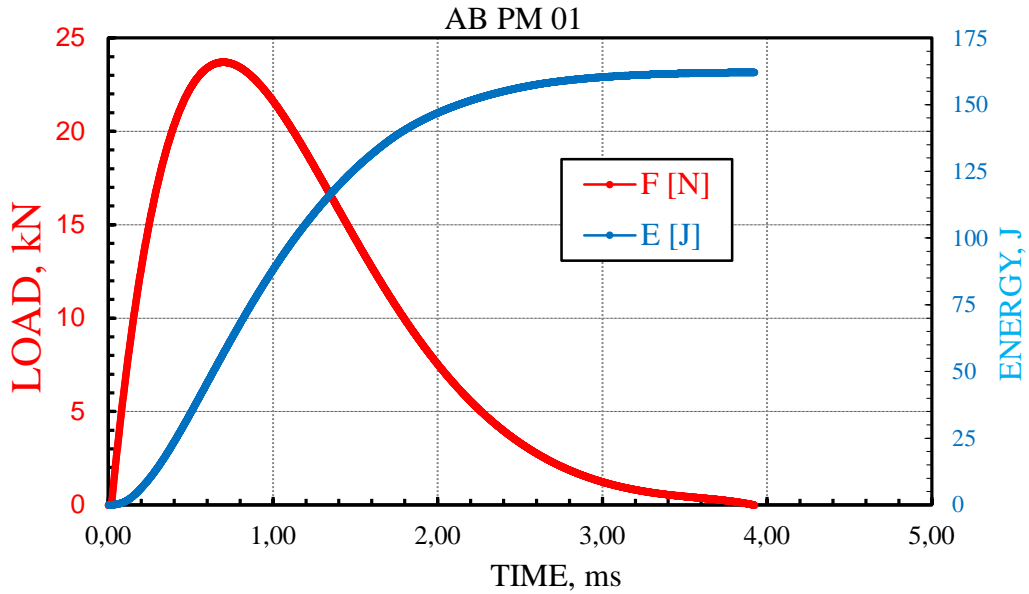


Figure 3.13. Charpy test for PM

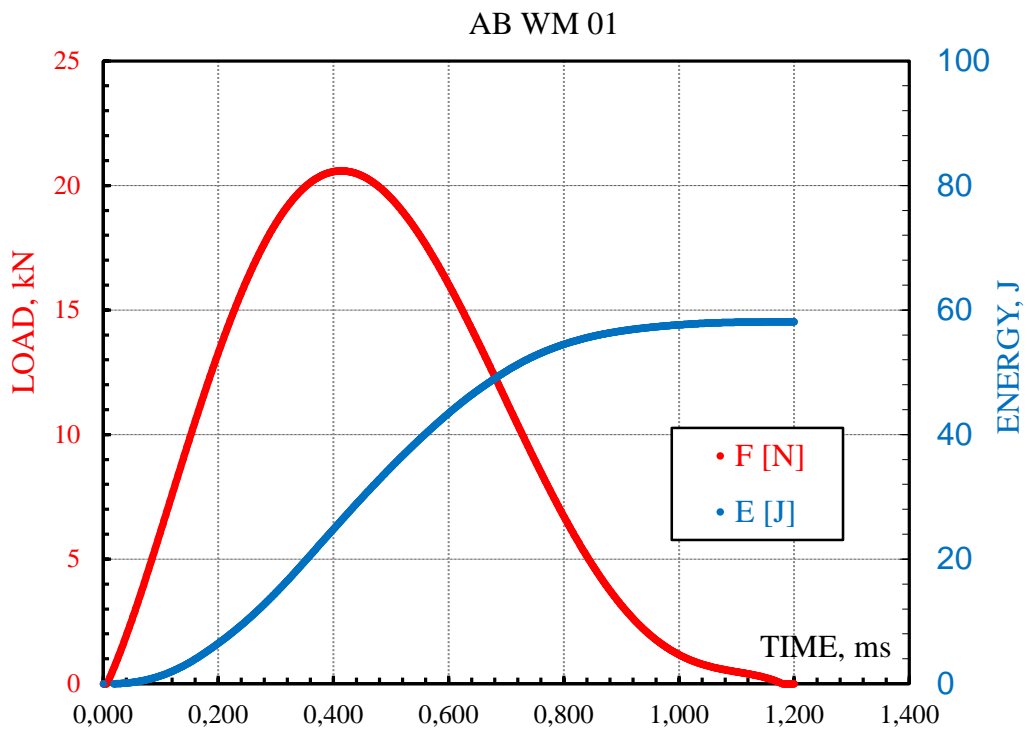


Figure 3.14. Load and Energy distribution for WM

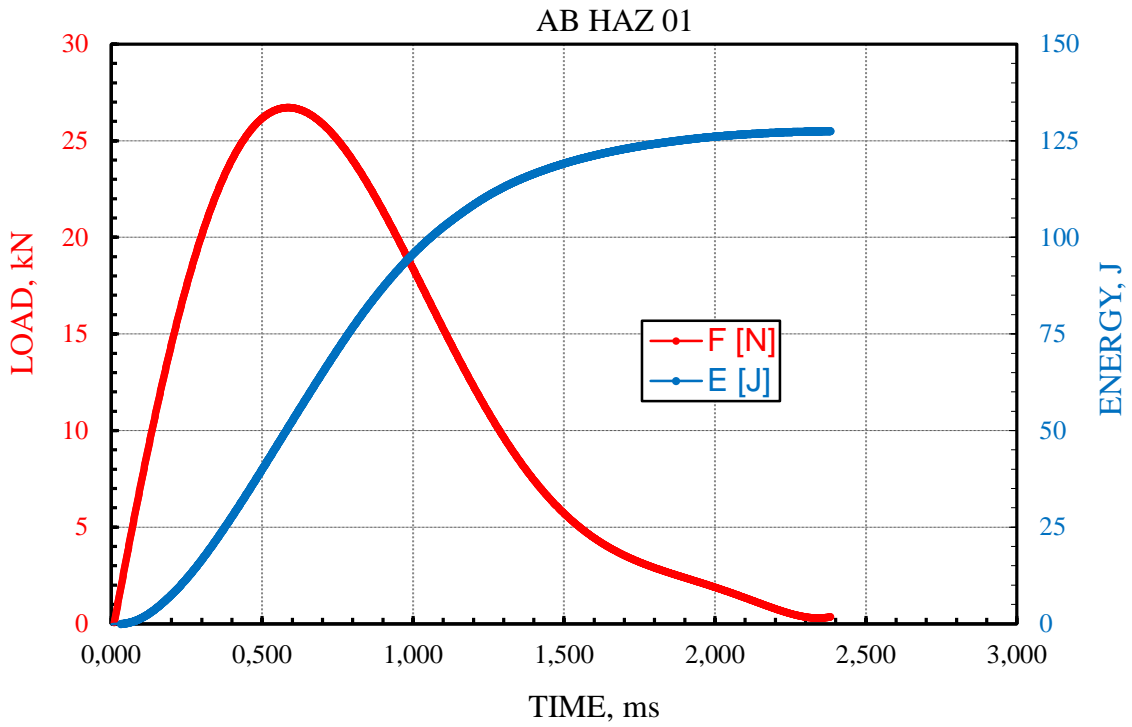


Figure 3.15. Charpy test results for HAZ constituent

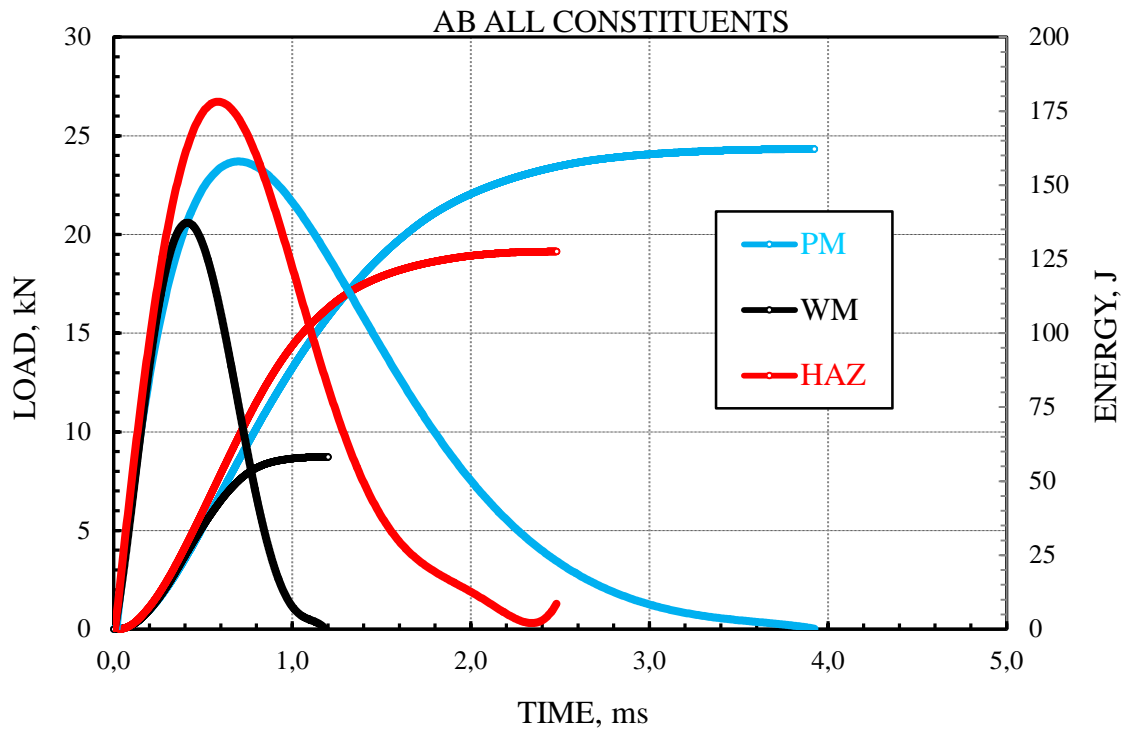


Figure 3.16. Charpy test results shown together PM, WM, HAZ

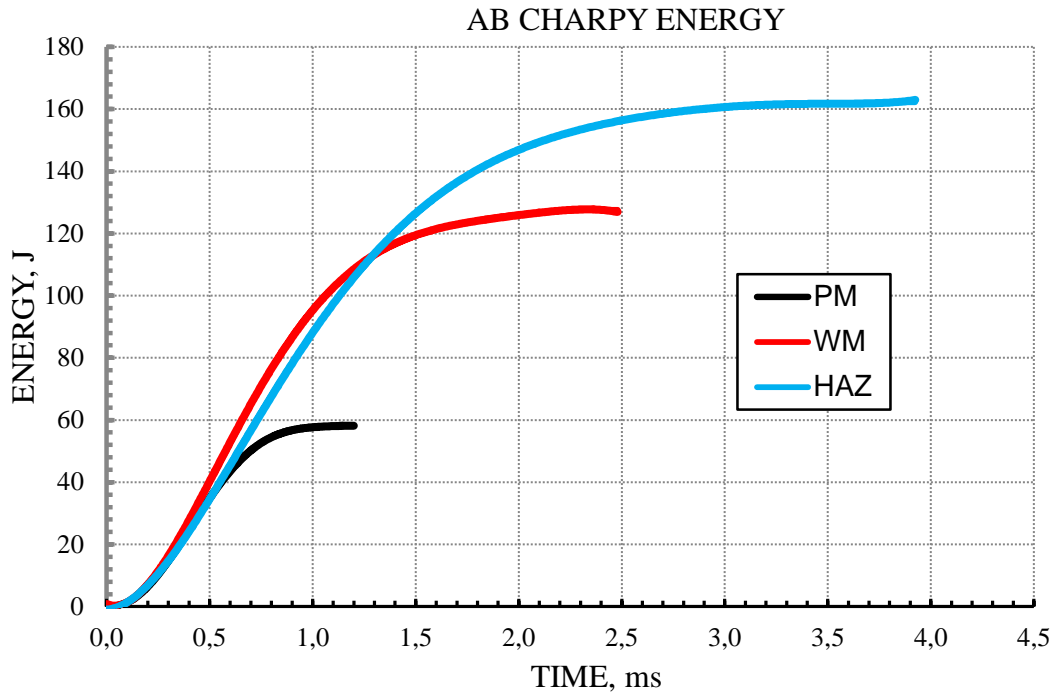


Figure 3.17. Detail of Fig 3.18 - Charpy energy distribution with time for PM, WM, HAZ

3.3. Fatigue testing results

Fatigue testing results for all welded joint results are given in Fig. 3.18-3.26, indicating similar crack resistance behavior as the case of Charpy toughness.

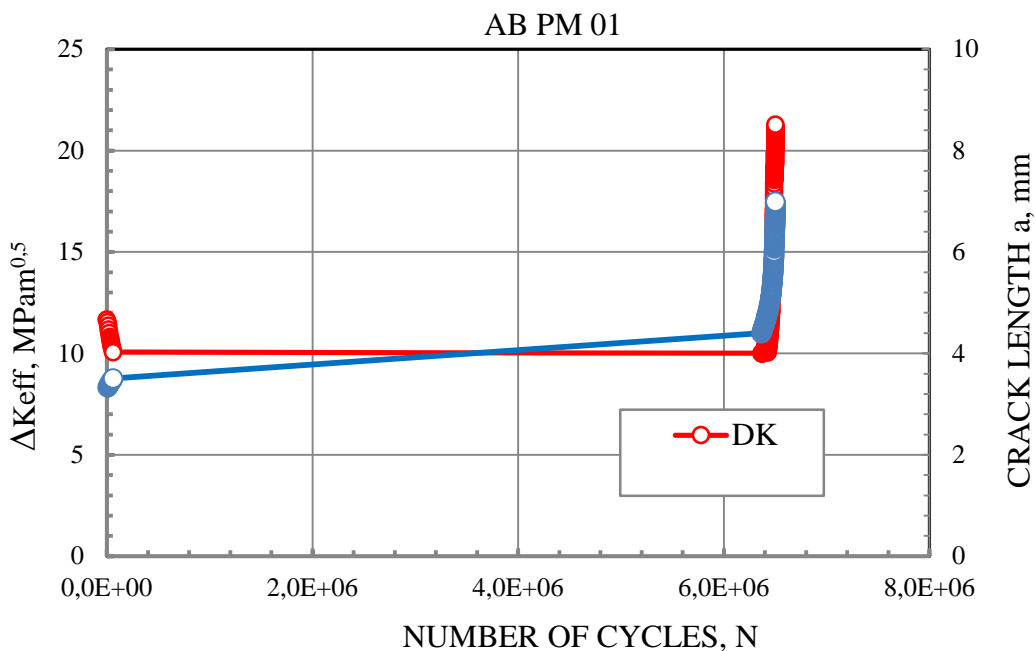


Figure 3.18. Distribution of crack length a and ΔK_{eff} for specimen made of PM

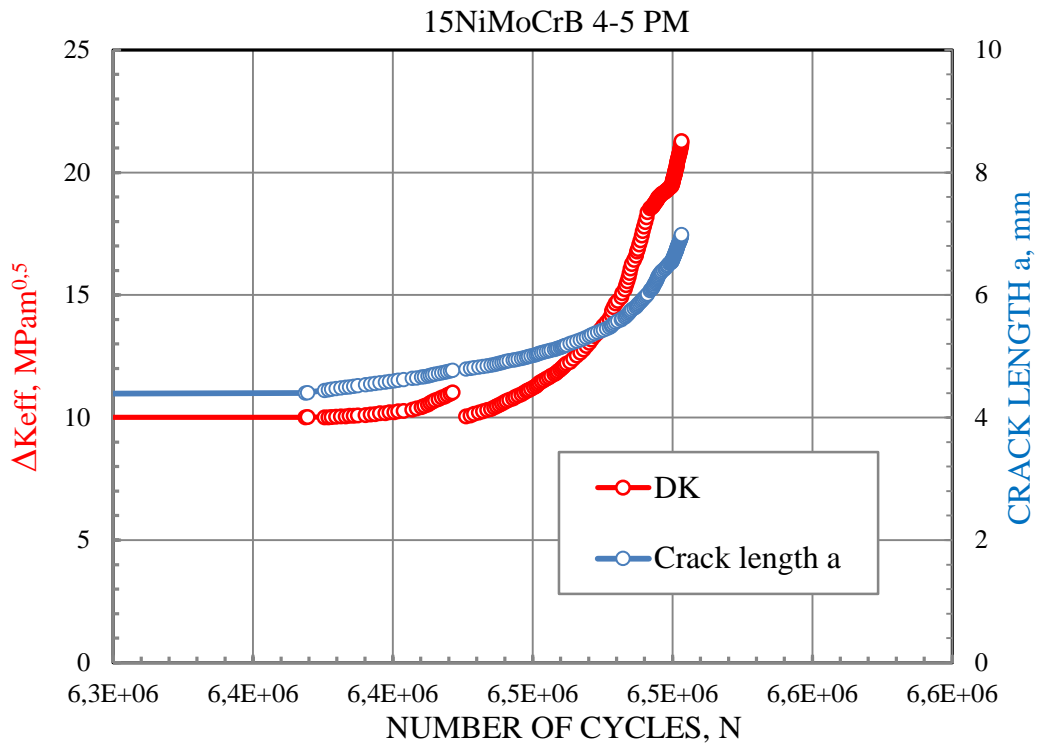


Figure 3.19. Detail of crack length a and ΔK_{eff} for specimen made of PM

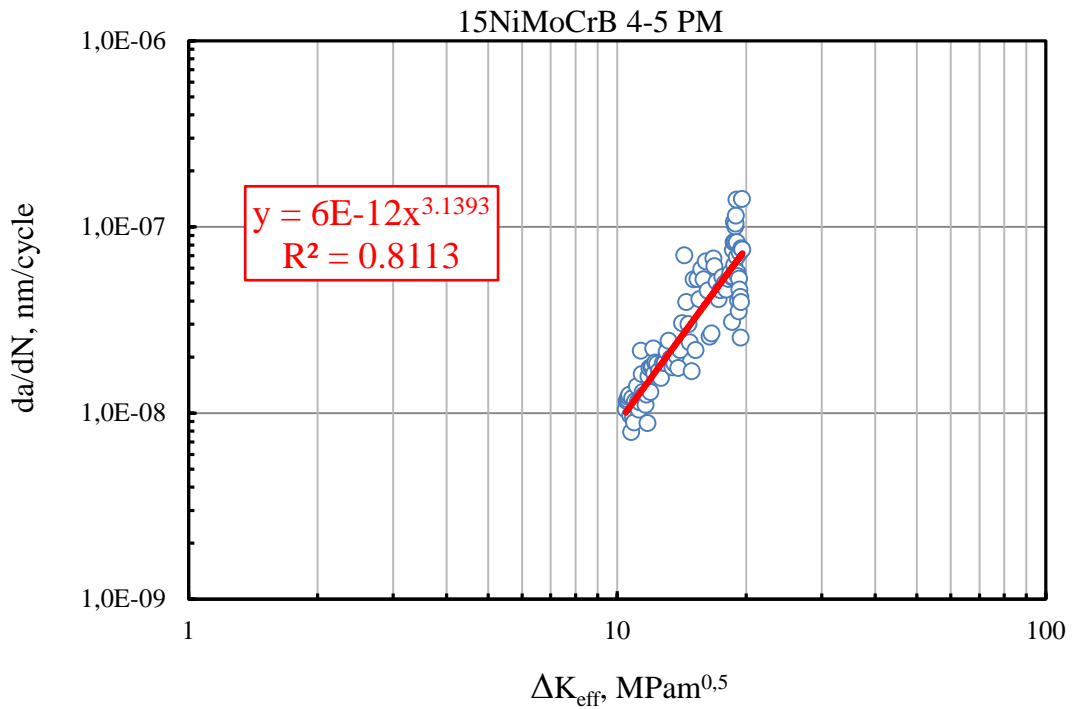


Figure 3.20. Crack growth rate of specimen made of PM

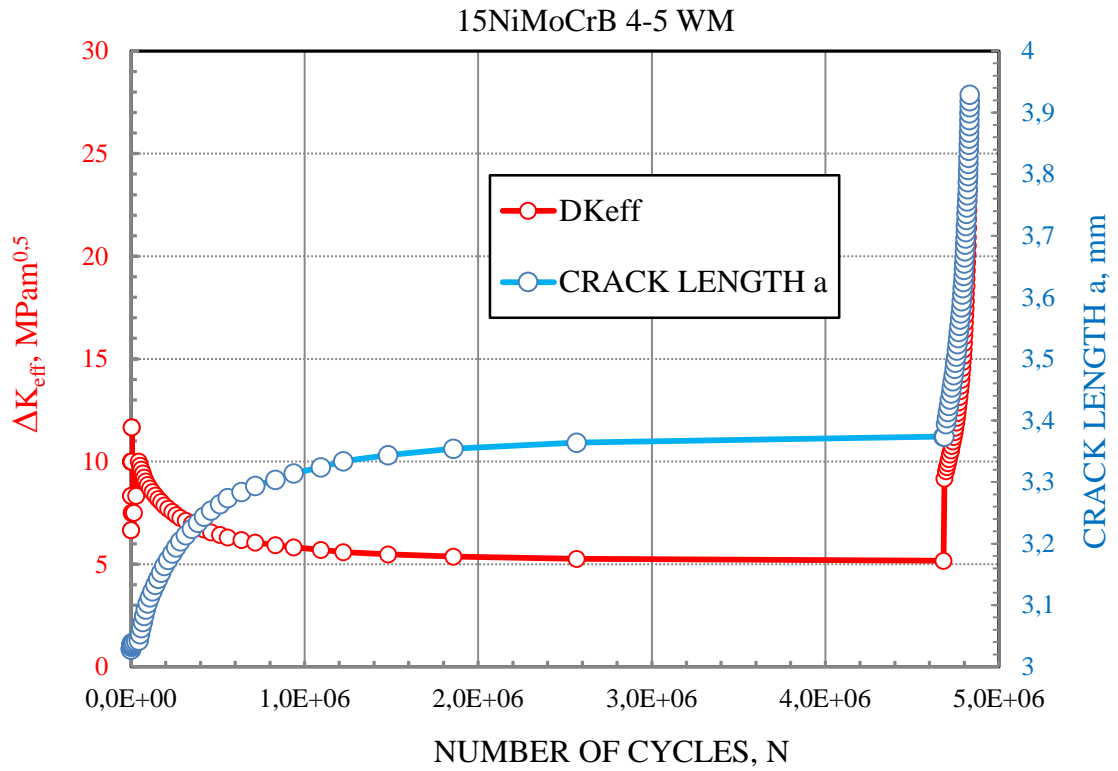


Figure 3.21. Change of crack length a and ΔK_{eff} with number of cycles N

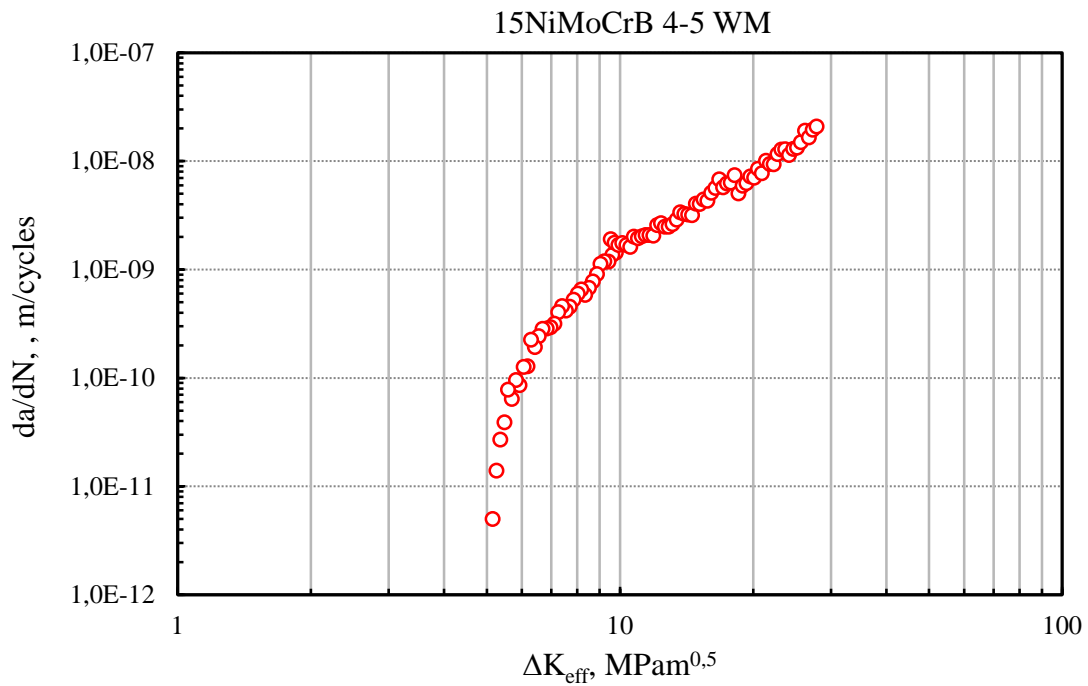


Figure 3.22. Fatigue crack growth for WM welded joint

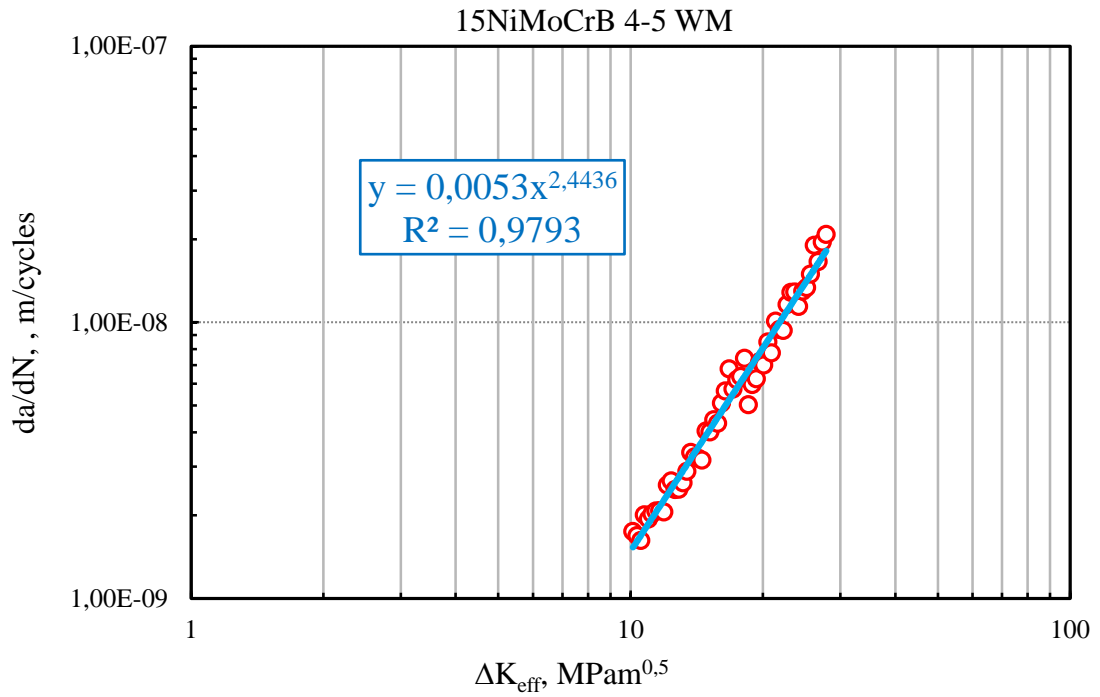


Figure 3.23. Detail of fatigue crack growth to define Paris law

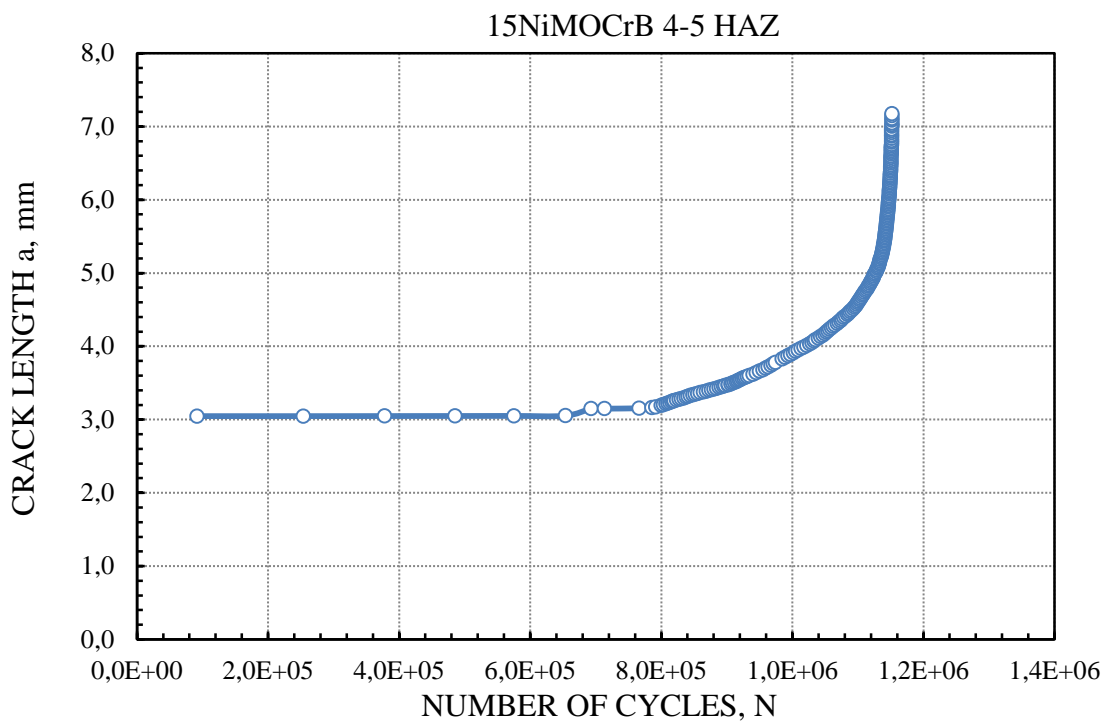


Figure 3.24. Distribution of crack length a with number of cycles for HAZ specimen

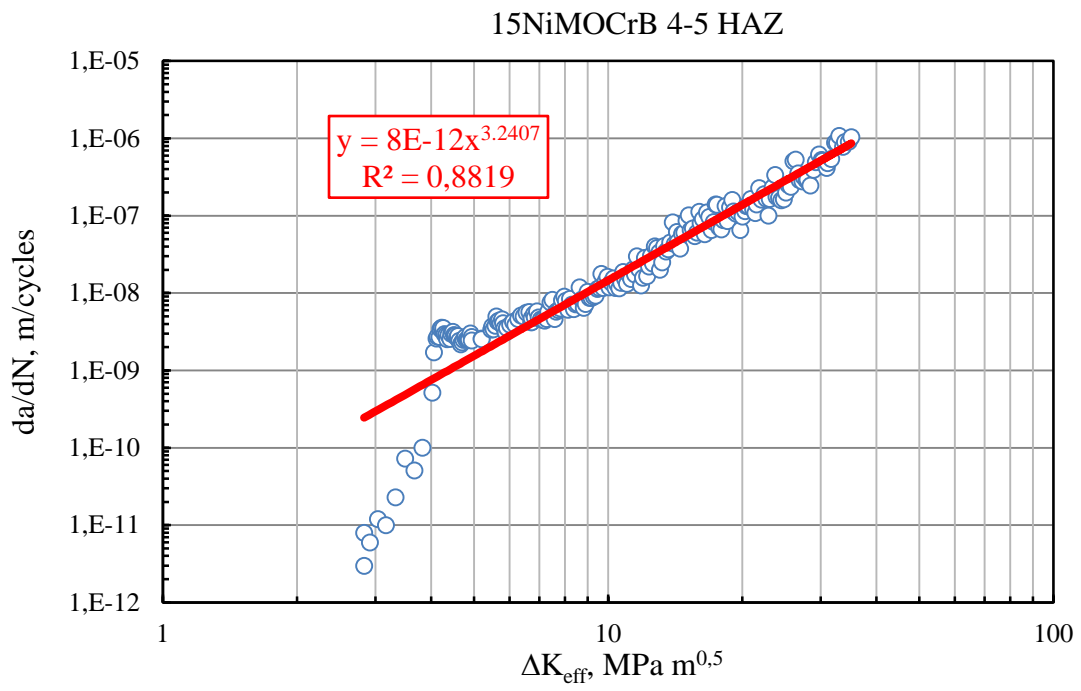


Figure 3.25. Crack growth rate for HAZ specimen given for all data

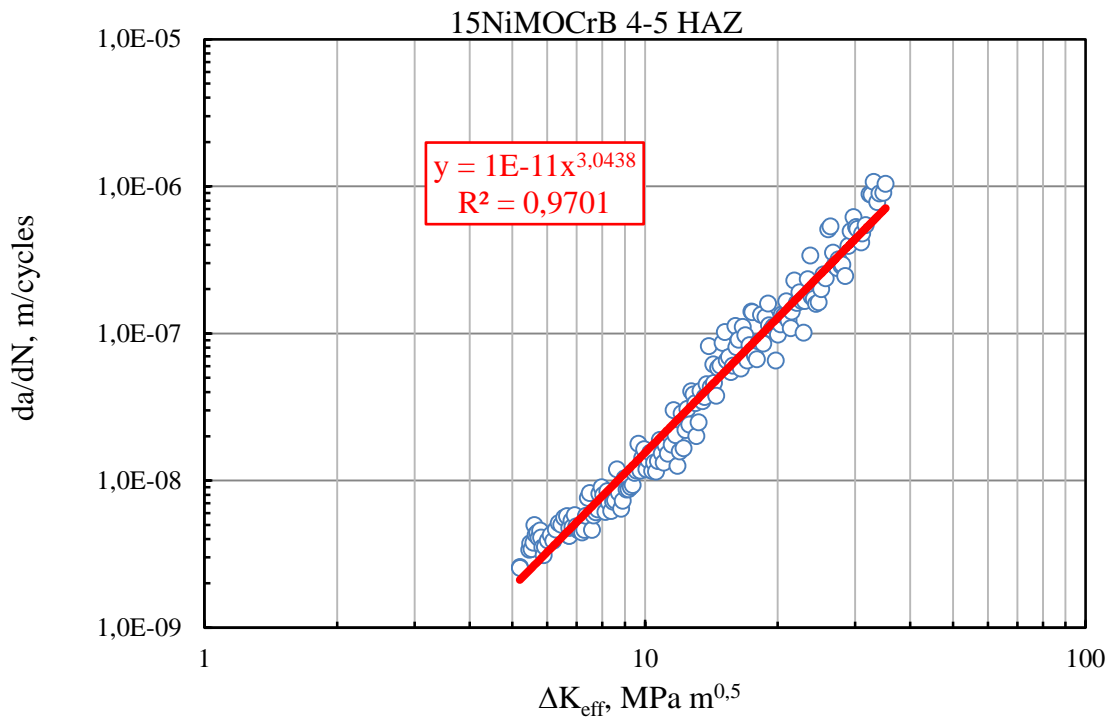


Figure 3.26. Detail of fatigue crack growth rate for Paris law

3.4. Fracture Mechanics testing

Because the available testing material was not enough for usual fracture mechanics tests all fracture toughness test were done on Charpy specimens. All specimens were fatigue pre-cracked on Instron servo-hydraulic machine capacity 100 kN. Crack growth was monitored with microscopy. The fatigue loads were calculated according to the ASTM standard ASTM E399. There were possible different methods for monitoring pre-fatigue crack growth. The goal of pre-cracking was to reach $a/W = 0.4$. Using of tint was disregarded because of later scanning electron microscopy observation.

TPB testing jig was original Instron. Because of the small specimens it was not possible to use standard rollers distance $S = 4 \cdot W = 40$ mm. Instead of this in order to use Crack Mouth Displacement Gage (CMOD gage), the distance between rollers was increased to 45 mm. The consequence of this is the not valid equation for unloading compliance. The calculated values of crack length has to be corrected according to the measured crack lengths at the beginning of the test a_o and final crack length at the end of the test a_f . The used specimens for evaluation of fracture toughness of all constituents from welded joint are showed in the Fig. 3.27.

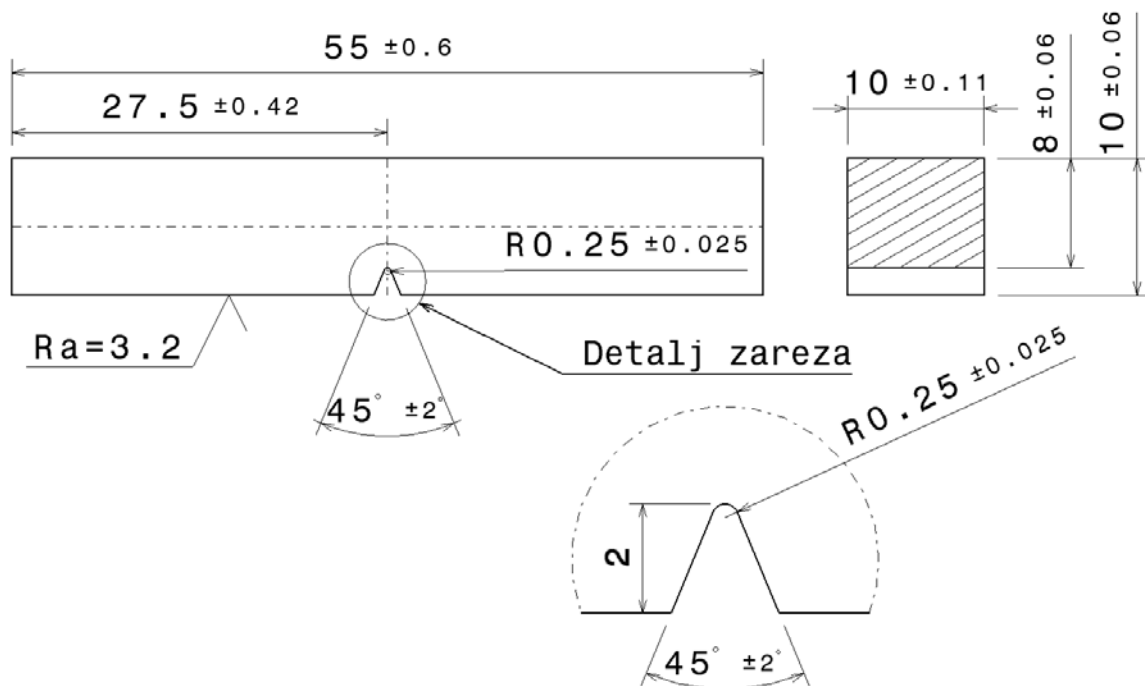


Figure 3.27. Charpy specimen used for fracture mechanics tests

3.4.1 Fracture toughness testing of WM

Fatigue precracked Charpy specimens were tested in Three Point Bending Tests (TPB) using original Instron testing jig. From loading cell digital loading data are evaluated together with the data obtained from CMOD gage. Partial unloading procedure was performed in order to evaluate compliance which will be used to calculate current crack length. Complete TPB test as load versus CMOD is shown in Fig. 3.28-3.29. All details of fracture toughness testing are explained in this chapter, as applied for the WM.

Fracture toughness of WM was evaluated on three Charpy specimens with notch tip positioned in WM middle, Precracking procedure was the same as PM tests, Digital test data were collected using the software which has analog data given in volts transferred in numbers giving N and mm , Change of load with CMOD is given in Fig. 3.29 showing all data points including partial unload-reload procedure.

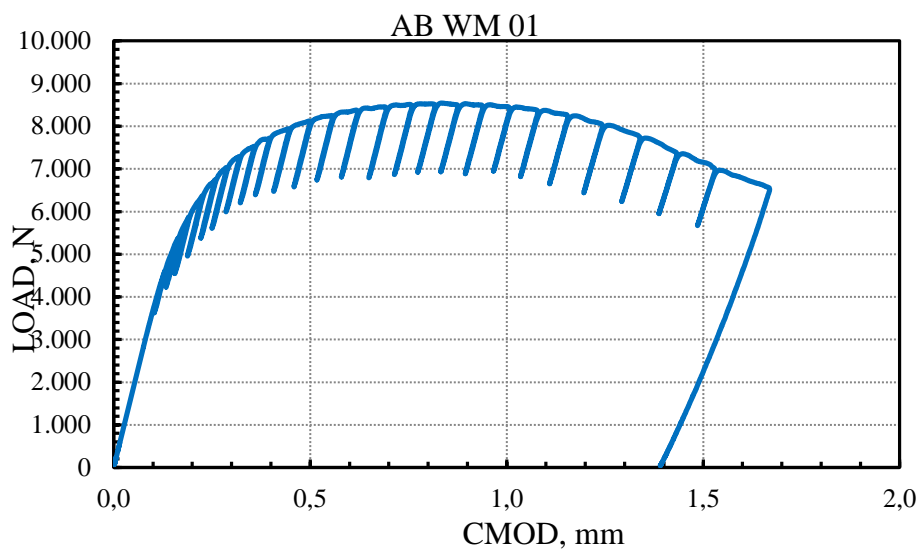


Figure 3.28. Typical diagram of load versus Crack Mouth Opening Displacement

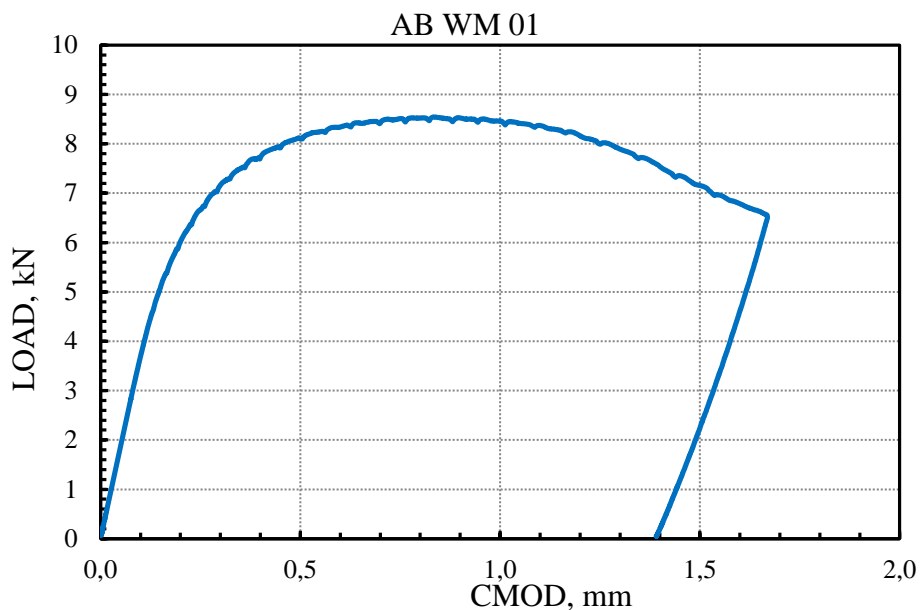


Figure 3.29. Smooth curve F-CMOD with removed partial unloading sequences

Linear part during loading start will be used to do rezeroid procedure to have zero CMOD for zero load. From linear part it is possible to get CMOD data used to correct complete F -CMOD curve. After this using diagram CMOD versus load from fitted linear equation is obtained initial compliance $d(\text{CMOD})/dF$ from which will be calculated initial crack length a_0 , Fig. 3.30. Next one has to mark parts of complete F -CMOD curve which represent unload – reload sequence and also chose the data from linear part and fitting get further compliances used for current crack length calculation. Removing the part unload-reload sequences from complete F -CMOD curve it will give smooth F -CMOD curve, typical for experiments where crack length is calculated using potential drop and Johnson formula. All partial unloading lines are given in Fig. 3.31.

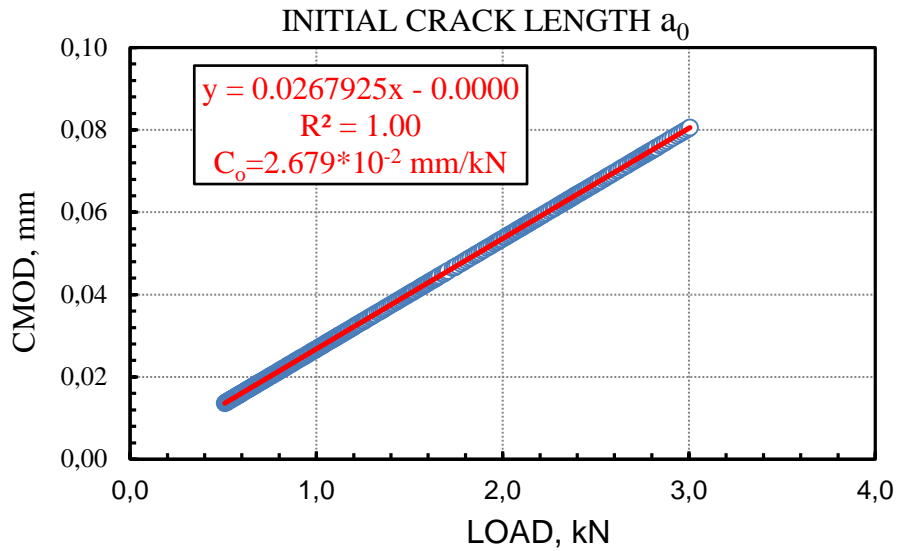


Figure 3.30. Initial compliance for calculating initial crack length a_0

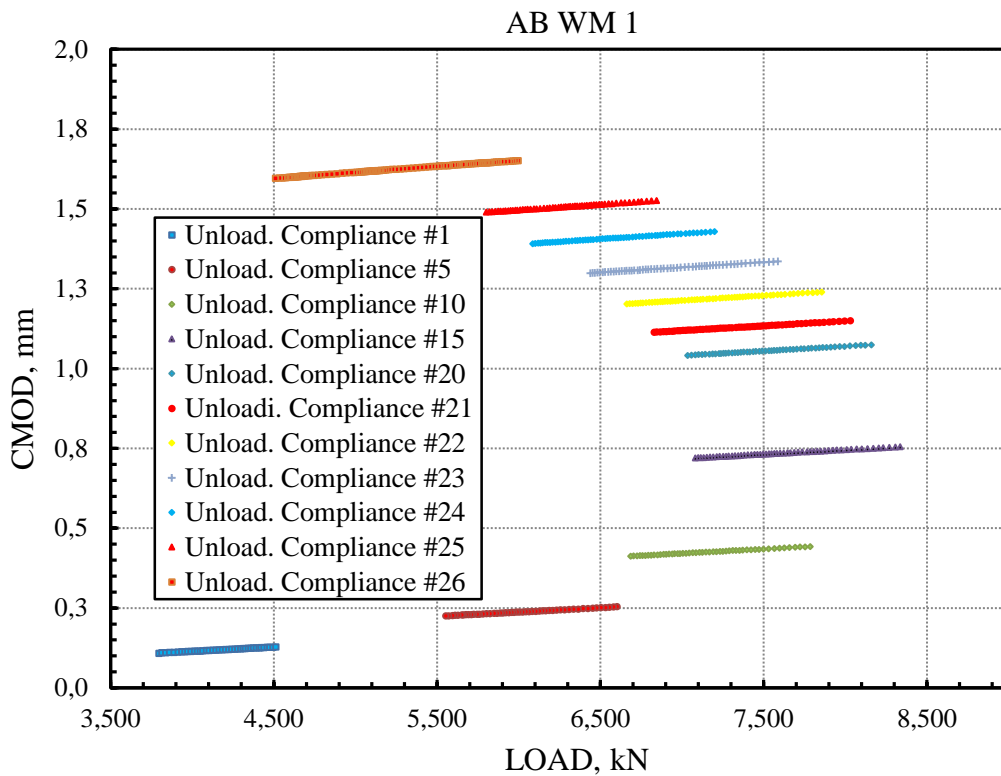


Figure 3.31. Distribution of all partial unloading compliances

To show the changes of compliances during the loading procedure, it is good to put together couple of compliances lines during the experiment. It is possible to see the change of the CMOD for certain load, Fig. 3.32.

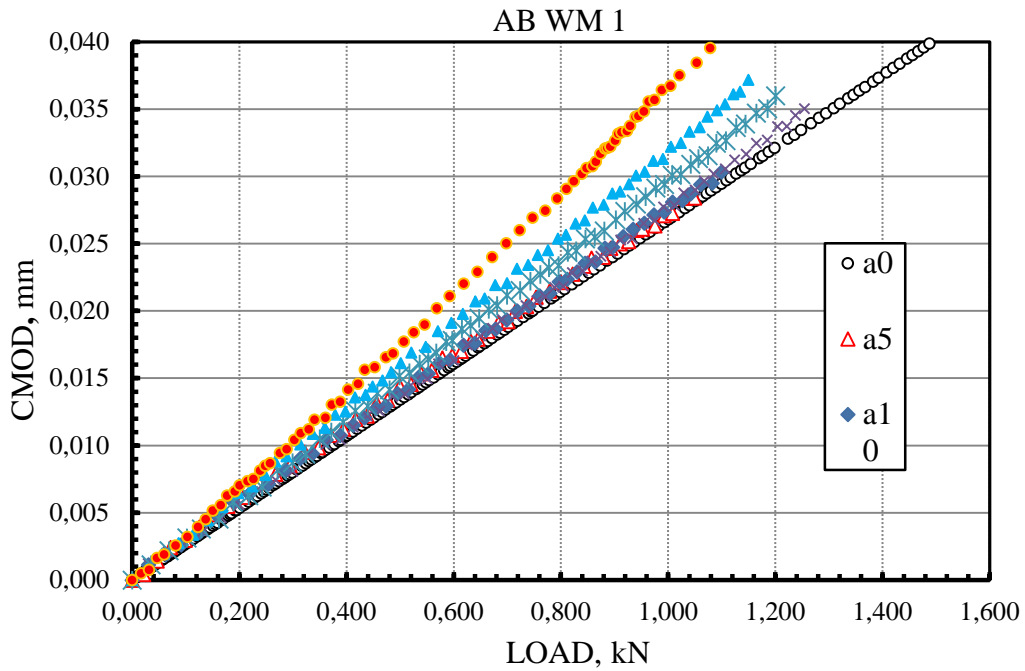


Figure 3.32. CMOD vs. Load

During the test data scatter is common and it is possible to show relationship of compliances with CMOD and use fitting procedure. Such a diagram is shown on Fig, 3.33.

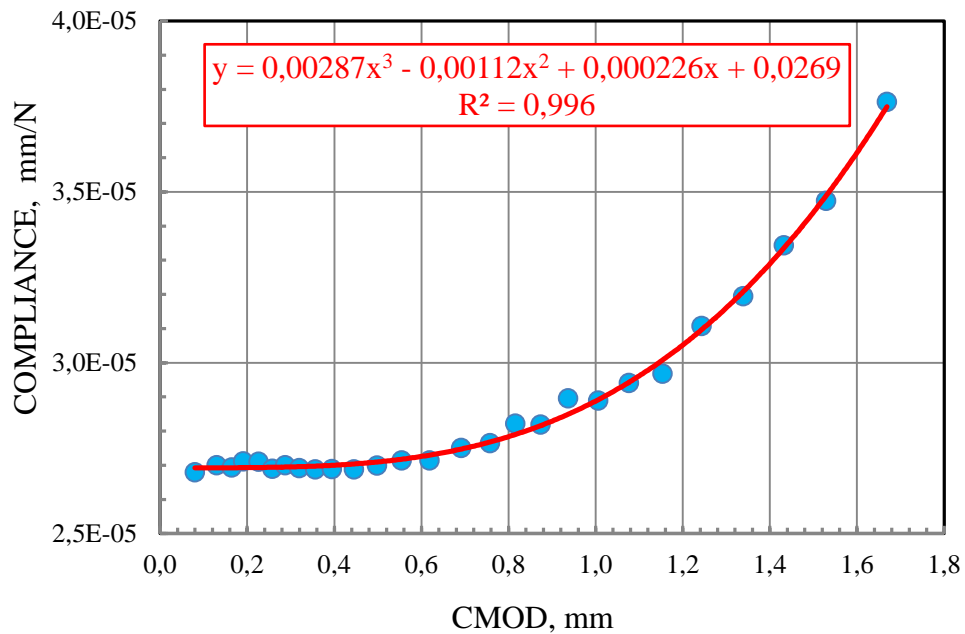


Figure 3.33. Fitting procedure of compliances with CMOD

Data evaluation was done using the Excel software. First step was to calculate relationship a/W value using the formula:

$$\frac{a_i}{W} = \left[0.999748 - 3.9504u + 2.9821u^2 - 3.21408u^3 + 51.51564u^4 - 113.031u^5 \right] \quad (3.3)$$

Where

$$u = \frac{1}{\left[\frac{4B_e W E C_i}{S} \right]^{0.5} + 1} \quad (3.4)$$

For $B_e = 10$ mm, $W = 10$ mm, $S = 45$ mm and $E = 200.4$ GPa, it is possible to calculate crack lengths from evaluated experimental compliance values using formula 3.1 and 3.2, Calculations values are given in Table 3.2

For experimentally obtained crack lengths we need to calculate adequate J values starting with smooth curve *load* – CMOD where sequences of partial unloading reloading are removed. Complete curve has to be divided into small increments using trapezoidal procedure for calculation using the formula

$$\Delta A_i = 0,5(F_i + F_{i+1})(LLD_{i+1} - LLD_i) \quad (3.5)$$

All area increments have to be summarized from zero point to the chosen point of interest as

$$A_{total} = \sum_0^i A_i \quad (3.6)$$

In order to get plastic area of load – load lone displacement it has to be calculated elastic part of energy area using formula

$$A_{elastic} = 0.5C_i F_i^2 \quad (3.7)$$

Where F_i is current load and C_i current compliance. Subtracting the elastic part of *load* – LLD curve plastic area which represent equal energy can be used for plastic contribution to the J -integral, But first to calculate elastic part of J -integral using current K_i which depends on the function $f(a_i/W)$ from following formula

$$f\left(\frac{a_i}{W}\right) = \frac{\left(2 + \frac{a_i}{W}\right) \left(0.886 + 4.64 \frac{a_i}{W} - 13.32 \left(\frac{a_i}{W}\right)^2 + 14.72 \left(\frac{a_i}{W}\right)^3 - 5.6 \left(\frac{a_i}{W}\right)^4\right)}{\left(1 - \frac{a_i}{W}\right)^{3/2}} \quad (3.8)$$

Current stress intensity factor K_i will be calculated form the next formula:

$$K_i = \frac{F_i}{(BB_N W)^{0.5}} f\left(\frac{a_i}{W}\right) \quad (3.9)$$

Having calculated values from formulas 3.6 and 3.7 it is the next step to calculate elastic part of the J -integral from the next formula

$$J_{el} = \frac{K_i^2 (1 - \nu^2)}{E} \quad (3.10)$$

Plastic part of the total *J-integral* depends on the plastic part of the area *load* – LLD which was calculated as $A_{pl} = A_{total} - A_{elastic}$.

$J_{plastic}$ written as J_{pl} is calculated from the formula as defined in ASTM E1820-16 Standard as:

$$J_{pl} = \frac{\eta_{pl(i)} A_{pl(i)}}{B_N b_o} \quad (3.11)$$

$\eta_{pl(i)} = 1.9$ if the load-line displacement is used for A_{pl} , and

If the CMOD record is used for A_{pl} then:

$$\eta_{pl(i)} = 3,785 - 3,101 \left(\frac{a_i}{W} \right) + 2,018 \left(\frac{a_i}{W} \right)^2 \quad (3.12)$$

Complete calculation is given in Table 3.2 and resulting *J-R* curve is presented in Fig. 3.34. Values for *J-integral* are presented for complete data points and separate only data points valid for J_{Ic} evaluation using power fit curve. Experimental data are giving J_{Ic} value 550 N/mm, the value which has to be checked according to the Standard ASTM E1820.

Table 3.2. Evaluation of specimen AB WM1 taking into account from machine obtained experimental data

AB WM 01		CMOD	Load	C_i	u_i	a_i/W	a_i	Δa
		mm	N	mm/N			mm	mm
B , mm	10	0.080	2977	2.679E-05	0.1255	0.554	5.539	0.000
W , mm	10	0.130	4606	2.700E-05	0.1250	0.555	5.553	0.013
S , mm	45	0.164	5368	2.693E-05	0.1252	0.555	5.548	0.009
a_{o-mes} , mm	3.915	0.191	5870	2.711E-05	0.1248	0.556	5.559	0.020
a_{f-mes} , mm	5.079	0.226	6367	2.710E-05	0.1248	0.556	5.559	0.020
a_{o-calc} , mm	5.539	0.257	6740	2.690E-05	0.1253	0.555	5.546	0.007
a_{f-calc} , mm	6.092	0.287	7030	2.700E-05	0.1250	0.555	5.553	0.013
$s_{0,2}$, MPa	768	0.319	7284	2.692E-05	0.1252	0.555	5.547	0.008
s_u , MPa	837	0.356	7523	2.688E-05	0.1253	0.555	5.545	0.006
s_{flow} , MPa	802.5	0.395	7718	2.688E-05	0.1253	0.555	5.545	0.006
E , GPa	204	0.445	7922	2.687E-05	0.1253	0.554	5.545	0.005
		0.498	8109	2,699E-05	0.1251	0.555	5.552	0.012
		0.555	8253	2,714E-05	0.1248	0.556	5.561	0.022
		0.618	8373	2,714E-05	0.1248	0.556	5.562	0.022
		0.691	8451	2,751E-05	0.1240	0.558	5.584	0.045
		0.758	8495	2,765E-05	0.1237	0.559	5.593	0.053
		0.815	8518	2,821E-05	0.1227	0.563	5.626	0.087
		0.874	8505	2,819E-05	0.1227	0.563	5.625	0.086
		0.937	8491	2,895E-05	0.1213	0.567	5.670	0.130
		1.006	8442	2,889E-05	0.1214	0.567	5.666	0.127
		1.076	8379	2,940E-05	0.1205	0.570	5.695	0.156
		1.154	8258	2,967E-05	0.1200	0.571	5.711	0.171
		1.243	8019	3,107E-05	0.1176	0.579	5.786	0.247
		1.338	7742	3,194E-05	0.1161	0.583	5.831	0.292
		1.432	7365	3,343E-05	0.1138	0.591	5.905	0.366
		1.529	7008	3,473E-05	0.1119	0.597	5.966	0.427
		1.669	6528	3,763E-05	0.1080	0.609	6.092	0.553

Table 3.2. Continuation

$f(a_i/W)$	K_i	A_{total}	$A_{i-elastic}$	$A_{i-plastic}$	J_{el}	J_{pl}	J_{total}
	MPa m ^{0.5}	Nmm	Nmm	Nmm	N/mm	N/mm	N/mm
3.186	42.7	119	119	0	8.1	0.0	8.1
3.200	66.3	312	286	26	19.6	1.1	20.7
3.196	77.2	482	388	94	26.6	4.0	30.6
3.208	84.7	633	467	166	32.0	7.1	39.1
3.208	91.9	848	549	298	37.7	12.7	50.4
3.193	96.9	1056	611	445	41.8	18.9	60.8
3.201	101.3	1262	667	594	45.7	25.3	71.0
3.195	104.7	1491	714	777	48.9	33.1	82.0
3.192	108.1	1765	761	1005	52.1	42.8	94.9
3.192	110.9	2059	801	1259	54.8	53.6	108.5
3.192	113.8	2457	843	1614	57.7	68.7	126.5
3.199	116.8	2880	887	1992	60.8	84.9	145.7
3.210	119.2	3347	924	2422	63.4	103.2	166.6
3.211	121.0	3873	951	2922	65.3	124.5	189.7
3.236	123.1	4487	982	3505	67.6	149.3	216.9
3.246	124.1	5049	998	4052	68.7	172.6	241.3
3.285	125.9	5542	1024	4518	70.7	192.5	263.2
3.284	125.7	6039	1020	5019	70.5	213.8	284.3
3.336	127.5	6577	1044	5533	72.5	235.7	308.2
3.332	126.6	7162	1030	6133	71.5	261.2	332.7
3.367	127.0	7755	1032	6722	71.9	286.4	358.2
3.386	125.8	8397	1012	7385	70.6	314.6	385.2
3.481	125.6	9130	999	8131	70.4	346.3	416.7
3.539	123.3	9883	957	8926	67.8	380.2	448.0
3.638	120.6	10594	907	9687	64.8	412.6	477.5
3.723	117.4	11293	853	10440	61.5	444.7	506.2
3.910	114.8	12243	802	11441	58.8	487.3	546.2

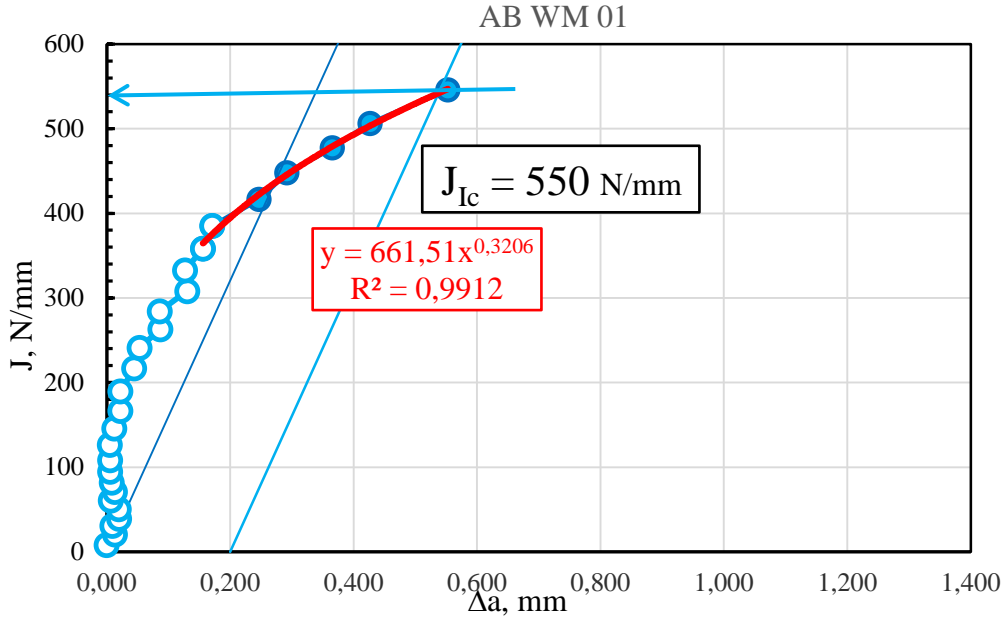


Figure 3.34. $J - R$ curve for AB WM 01 specimen taking into account original crack lengths a_i obtained from the experiment

After the TPB test the specimen was heat tinted for 300°C in furnace for one hour and brittle broken after treatment of 15 min in liquid hydrogen. After the brittle fracture it was possible to measure the initial and final crack length a_o and a_f . For initial crack length a_o using the Standard ASTM E1820 it is possible to calculate initial unloading compliance and compare it with obtained from the experimental data, formula for calculation of initial compliance is given as:

$$C_{(i)} = \frac{1}{EB_e} \left(\frac{S}{W - a_i} \right)^2 \left[1,193 - 1,98 \left(\frac{a_i}{W} \right) + 4,478 \left(\frac{a_i}{W} \right)^2 - 4,443 \left(\frac{a_i}{W} \right)^3 + 1,739 \left(\frac{a_i}{W} \right)^4 \right] \quad (3.13)$$

For given experimental data $a_o = 3.915$ mm, $E = 200.4$ GPa, $W = 10$ mm and $S = 45$ mm the calculated value for unloading compliance is equal to $C_o = 2.332E-05$ mm/N which is different from the experimental value of $C_o = 2.679E-05$ mm/N.

In order to have better distribution of current crack lengths a_i according to the measured values a_o and a_f after brittle fracture of the specimen after the test. Crack length correction has been done with the next formula:

$$a_i = a_{omes} + \frac{a_{fmes} - a_{omes}}{a_{fcalc} - a_{ocalc}} (a_{icalc} - a_{ocalc}) \quad (3.14)$$

Where a_i current crack length, a_{omeas} measured initial crack length, a_{fmeas} measured final crack length, a_{icalc} current calculated crack length, a_{ocalc} calculated initial crack length, a_{fcalc} calculated final crack length. Complete recalculation will be presented in Table 3.3.

Table 3.3. Evaluation of specimen AB WM1 with corrected a_i from the experimental data

AB WM 01		CMOD	Load	C_i	u_i	a_i/W	a_i	a_{i-cor}	Δa
		mm	N	mm/N			mm	mm	mm
B , mm	10	0.080	2,977	2.679E-05	0.125	0.554	5.539	3.915	0.000
W , mm	10	0.130	4,606	2.700E-05	0.125	0.555	5.553	3.943	0.028
S , mm	45	0.164	5,368	2.693E-05	0.125	0.555	5.548	3.934	0.019
a_{o-mes} , mm	3.915	0.191	5,870	2.711E-05	0.125	0.556	5.559	3.957	0.042
a_{f-mes} , mm	5.079	0.226	6,367	2.710E-05	0.125	0.556	5.559	3.956	0.041
a_{o-calc} , mm	5.539	0.257	6,740	2.690E-05	0.125	0.555	5.546	3.929	0.014
a_{f-calc} , mm	6.092	0.287	7,030	2.700E-05	0.125	0.555	5.553	3.943	0.028
$s_{0,2}$, MPa	768	0.319	7,284	2.692E-05	0.125	0.555	5.547	3.932	0.017
s_u , MPa	837	0.356	7,523	2.688E-05	0.125	0.555	5.545	3.927	0.012
s_{flow} , MPa	802.5	0.395	7,718	2.688E-05	0.125	0.555	5.545	3.927	0.012
E , GPa	204	0.445	7,922	2.687E-05	0.125	0.554	5.545	3.926	0.011
		0.498	8.109	2,699E-05	0.125	0.555	5.552	3.941	0.026
		0.555	8.253	2,714E-05	0.125	0.556	5.561	3.961	0.046
		0.618	8.373	2,714E-05	0.125	0.556	5.562	3.961	0.046
		0.691	8.451	2,751E-05	0.124	0.558	5.584	4.009	0.094
		0.758	8.495	2,765E-05	0.124	0.559	5.593	4.027	0.112
		0.815	8.518	2,821E-05	0.123	0.563	5.626	4.098	0.183
		0.874	8.505	2,819E-05	0.123	0.563	5.625	4.095	0.180
		0.937	8.491	2,895E-05	0.121	0.567	5.670	4.189	0.274
		1.006	8.442	2,889E-05	0.121	0.567	5.666	4.182	0.267
		1.076	8.379	2,940E-05	0.120	0.570	5.695	4.243	0.328
		1.154	8.258	2,967E-05	0.120	0.571	5.711	4.275	0.360
		1.243	8.019	3,107E-05	0.118	0.579	5.786	4.435	0.520
		1.338	7.742	3,194E-05	0.116	0.583	5.831	4.530	0.615
		1.432	7.365	3,343E-05	0.114	0.591	5.905	4.685	0.770
		1.529	7.008	3,473E-05	0.112	0.597	5.966	4.813	0.898
		1.669	6.528	3,763E-05	0.108	0.609	6.092	5.079	1.164

Table 3.3. Continuation

$a_{i\ corr}/W$	$f(a_i/W)$	K_i	A_{total}	A_{i-el}	A_{i-pl}	J_{el}	J_{pl}	J_{total}
		MPa m ^{0.5}	Nmm	Nmm	Nmm	N/mm	N/mm	N/mm
0.392	1.936	25.9	119	119	0	3.0	0.0	3.0
0.394	1.951	40.4	312	286	26	7.3	0.8	8.1
0.393	1.946	47.0	482	388	94	9.9	2.9	12.8
0.396	1.958	51.7	633	467	166	11.9	5.2	17.1
0.396	1.958	56.1	848	549	298	14.0	9.3	23.4
0.393	1.943	58.9	1056	611	445	15.5	13.9	29.4
0.394	1.951	61.7	1262	667	594	17.0	18.6	35.5
0.393	1.945	63.8	1491	714	777	18.1	24.3	42.4
0.393	1.942	65.8	1765	761	1005	19.3	31.4	50.7
0.393	1.942	67.5	2059	801	1259	20.3	39.3	59.6
0.393	1.942	69.2	2457	843	1614	21.4	50.4	71.8
0.394	1.950	71.1	2880	887	1992	22.6	62.2	84.8
0.396	1.961	72.8	3347	924	2422	23.7	75.6	99.3
0.396	1.961	73.9	3873	951	2922	24.3	91.2	115.6
0.401	1.987	75.5	4487	982	3505	25.5	109.4	134.9
0.403	1.997	76.3	5049	998	4052	26.0	126.5	152.5
0.410	2.037	78.1	5542	1024	4518	27.2	141.1	168.3
0.410	2.035	77.9	6039	1020	5019	27.1	156.7	183.8
0.419	2.090	79.8	6577	1044	5533	28.4	172.8	201.2
0.418	2.085	79.2	7162	1030	6133	28.0	191.5	219.5
0.424	2.122	80.0	7755	1032	6722	28.5	209.9	238.5
0.428	2.141	79.6	8397	1012	7385	28.2	230.6	258.8
0.444	2.242	80.9	9130	999	8131	29.2	253.9	283.1
0.453	2.305	80.3	9883	957	8926	28.8	278.7	307.5
0.468	2.415	80.0	10594	907	9687	28.6	302.5	331.1
0.481	2.512	79.2	11293	853	10440	28.0	326.0	354.0
0.508	2.731	80.2	12243	802	11441	28.7	357.2	385.9

Obtained results for relevant J - R curve are presented in Fig. 3.35. Finally we are able to fit experimental partial unloading compliance with CMOD distribution and construct the smooth J - R curve which is valid for instability points for prediction of break at pressure vessels and pipes. Recalculated data are given in Table 3.4.

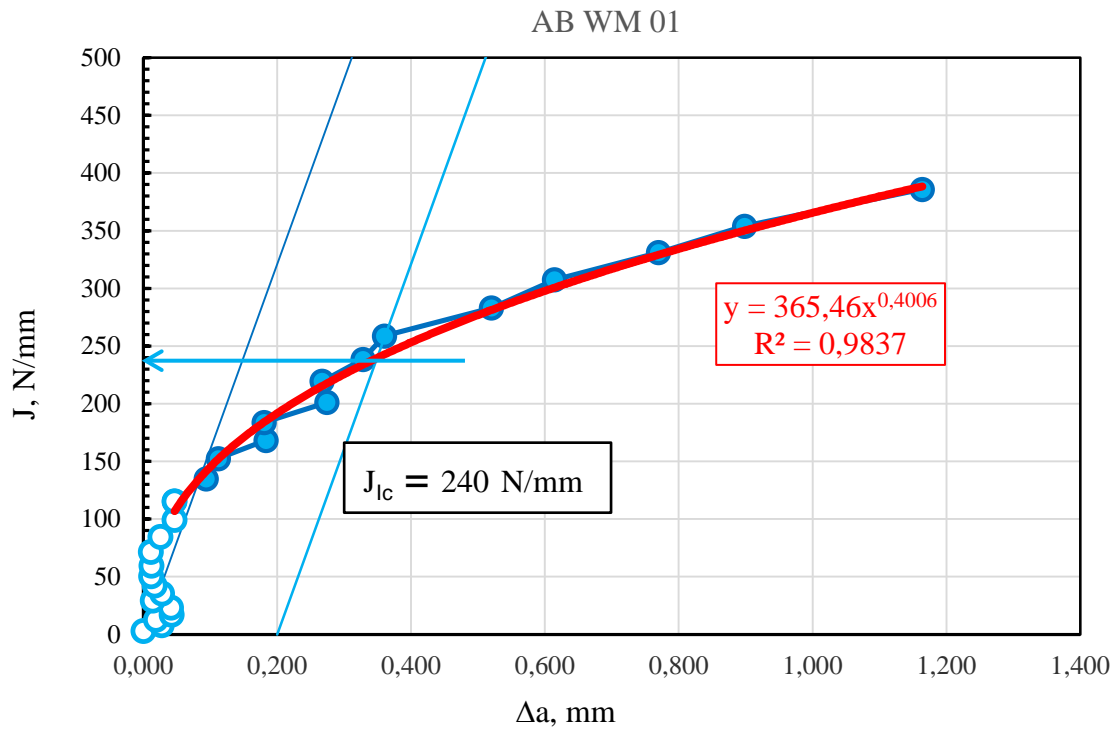


Figure 3.35. J - R curve for AB WM 01 specimen with corrected experimental crack lengths a_i

Table 3.4. *J-R* evaluation using fitting of compliance with CMOD

AB WM 01		CMOD	Load	C_{i-fit}	u_i	a_i/W	a_i	a_{i-cor}
		mm	N	mm/N			mm	mm
B , mm	10	0,080	2,977	2.692E-05	0.125	0.555	5.548	3.915
W , mm	10	0,130	4,606	2.692E-05	0.125	0.555	5.548	3.916
S , mm	45	0,164	5,368	2.693E-05	0.125	0.555	5.548	3.916
a_{o-mes} , mm	3.915	0,191	5,870	2.693E-05	0.125	0.555	5.548	3.916
a_{f-mes} , mm	5.079	0,226	6,367	2.693E-05	0.125	0.555	5.548	3.917
a_{o-calc} , mm	5.539	0,257	6,740	2.694E-05	0.125	0.555	5.549	3.918
a_{f-calc} , mm	6.092	0,287	7,030	2.695E-05	0.125	0.555	5.549	3.919
$s_{0,2}$, MPa	768	0,319	7,284	2.696E-05	0.125	0.555	5.550	3.920
s_u , MPa	837	0,356	7,523	2.698E-05	0.125	0.555	5.551	3.922
s_{flow} , MPa	802.5	0,395	7,718	2.700E-05	0.125	0.555	5.552	3.926
E , GPa	204	0,445	7,922	2.704E-05	0.125	0.555	5.555	3.931
		0.498	8,109	2,710E-05	0.125	0.556	5.559	3.939
		0.555	8,253	2,718E-05	0.125	0.556	5.564	3.950
		0.618	8,373	2,730E-05	0.124	0.557	5.571	3.965
		0.691	8,451	2,747E-05	0.124	0.558	5.582	3.989
		0.758	8,495	2,768E-05	0.124	0.559	5.595	4.016
		0.815	8,518	2,790E-05	0.123	0.561	5.608	4.045
		0.874	8,505	2,816E-05	0.123	0.562	5.623	4.079
		0.937	8,491	2,849E-05	0.122	0.564	5.643	4.121
		1.006	8,442	2,892E-05	0.121	0.567	5.668	4.174
		1.076	8,379	2,943E-05	0.120	0.570	5.697	4.237
		1.154	8,258	3,008E-05	0.119	0.573	5.733	4.315
		1.243	8,019	3,097E-05	0.118	0.578	5.781	4.418
		1.338	7,742	3,208E-05	0.116	0.584	5.838	4.543
		1.432	7,365	3,336E-05	0.114	0.590	5.901	4.679
		1.529	7,008	3,488E-05	0.112	0.597	5.973	4.834
		1.669	6,528	3,750E-05	0.108	0.609	6.087	5.079

Table 3.4. Continuation

Δa	$a_{i\text{ cor}}/W$	$f(a_i/W)$	K_i	A_{total}	A_{i-el}	A_{i-pl}	J_{el}	J_{pl}	J_{total}
mm			MPa m ^{0.5}	Nmm	Nmm	Nmm	N/mm	N/mm	N/mm
0.000	0.392	1.936	25.9	119	119	-1	3.0	0.0	3.0
0.001	0.392	1.936	40.1	312	286	27	7.2	0.8	8.0
0.001	0.392	1.936	46.8	482	388	95	9.8	3.0	12.7
0.001	0.392	1.937	51.2	633	464	169	11.7	5.3	17.0
0.002	0.392	1.937	55.5	848	546	302	13.7	9.4	23.2
0.003	0.392	1.937	58.8	1056	612	444	15.4	13.9	29.3
0.004	0.392	1.938	61.3	1262	666	596	16.8	18.6	35.4
0.005	0.392	1.939	63.6	1491	715	776	18.0	24.2	42.3
0.007	0.392	1.940	65.7	1765	763	1002	19.2	31.3	50.5
0.011	0.393	1.942	67.4	2059	804	1255	20.3	39.2	59.5
0.016	0.393	1.945	69.3	2457	848	1609	21.4	50.2	71.7
0.024	0.394	1.949	71.1	2880	891	1989	22.6	62.1	84.7
0.035	0.395	1.954	72.6	3347	926	2421	23.5	75.6	99.1
0.050	0.397	1.963	74.0	3873	957	2917	24.4	91.1	115.5
0.074	0.399	1.976	75.1	4487	981	3506	25.2	109.5	134.7
0.101	0.402	1.991	76.1	5049	999	4051	25.8	126.5	152.3
0.130	0.404	2.007	76.9	5542	1012	4529	26.4	141.4	167.8
0.164	0.408	2.026	77.5	6039	1019	5021	26.8	156.8	183.6
0.206	0.412	2.050	78.3	6577	1027	5549	27.4	173.3	200.6
0.259	0.417	2.081	79.0	7162	1030	6132	27.9	191.5	219.3
0.322	0.424	2.118	79.9	7755	1033	6722	28.4	209.9	238.3
0.400	0.432	2.166	80.5	8397	1026	7371	28.9	230.2	259.1
0.503	0.442	2.232	80.5	9130	996	8134	28.9	254.0	282.9
0.628	0.454	2.314	80.6	9883	961	8922	29.0	278.6	307.6
0.764	0.468	2.411	79.9	10594	905	9689	28.5	302.5	331.0
0.919	0.483	2.527	79.7	11293	857	10437	28.3	325.9	354.2
1.164	0.508	2.731	80.2	12243	799	11444	28.7	357.3	386.0

The value $J_{Ic} = 240$ N/mm, Fig. 3.36, is the same for corrected crack lengths and fitted compliance values. All other specimens will be evaluated with corrected a_i values and for some cases will be used fitted compliance values. On basis of fitted compliance values obtained J - R curve is presented in Fig. 3.37. For specimen AB WM 02 relevant diagrams are presented in Figures 3.38-3.41 and Tables 3.5-3.6.

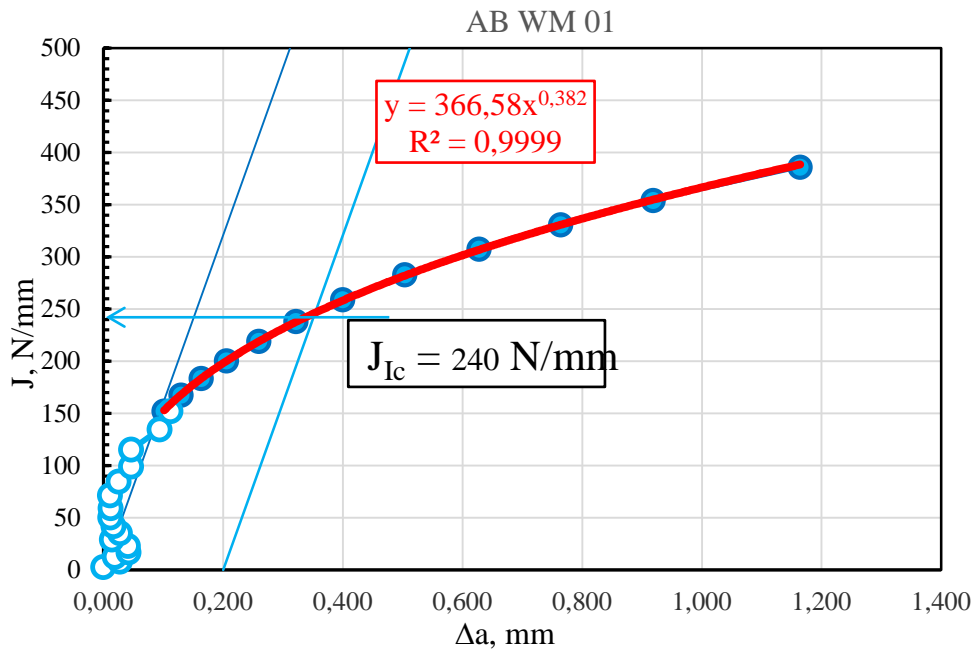


Figure 3.36. $J - R$ curve for AB WM 01 specimen for fitted compliances with CMOD change

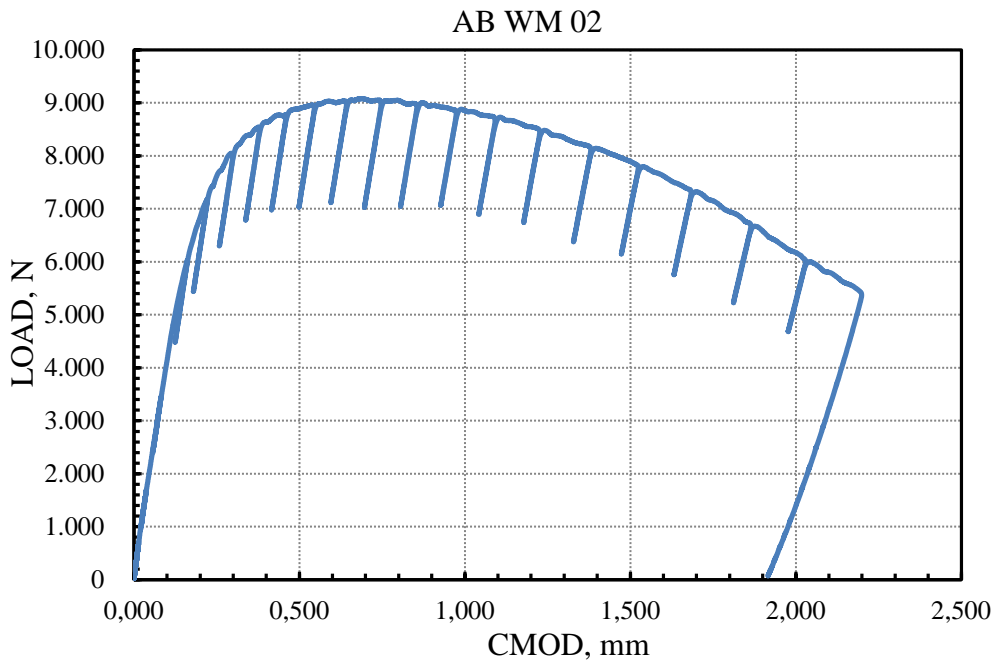


Figure 3.37. Distribution of load with CMOD for specimen AB WM 02

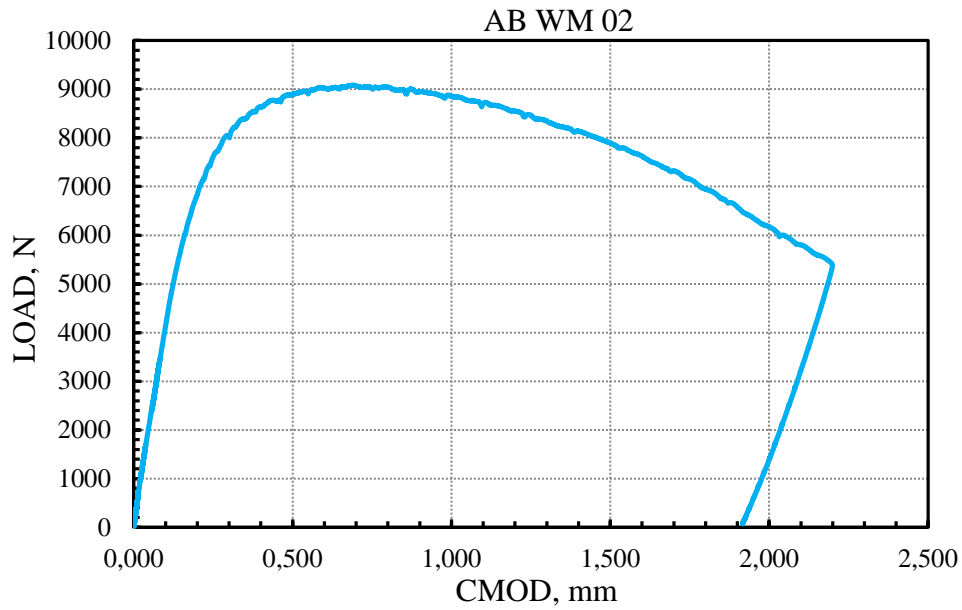


Figure 3.38. Load vs, CMOD without unloading compliance sequences.

Table 3.5. Evaluation of specimen AB WM 02 with corrected crack lengths

AB WM 02		F	$CMOD$	$Compl., C_i$	u_i	a_i	a_i - $cor,$	Δa_i
		N	mm	mm/N		mm		mm
B, mm	10	4347	0.106	2.523E-05	0.129	5.437	3.848	0.000
W, mm	10	6027	0.162	2.413E-05	0.131	5.360	3.713	-0.135
S, mm	45	7179	0.222	2.464E-05	0.130	5.396	3.776	-0.072
a_{o-mes}, mm	3.848	8045	0.296	2.459E-05	0.130	5.393	3.770	-0.078
a_{f-mes}, mm	5.487	8534	0.378	2.486E-05	0.130	5.411	3.803	-0.045
a_{o-calc}, mm	5.437	8749	0.459	2.496E-05	0.129	5.419	3.815	-0.033
a_{f-calc}, mm	6.370	8947	0.544	2.523E-05	0.129	5.437	3.848	0.000
$s_{0,2}, MPa$	768	9012	0.642	2.608E-05	0.127	5.494	3.948	0.100
s_u, MPa	837	9025	0.746	2.644E-05	0.126	5.517	3.989	0.141
s_{flow}, MPa	802.5	8908	0.855	2.685E-05	0.125	5.543	4.034	0.186
E, GPa	204	8831	0.974	2.789E-05	0.123	5.607	4.147	0.299
		8703	1.091	2.856E-05	0.122	5.647	4.217	0.369
		8437	1.226	2.910E-05	0.121	5.678	4.272	0.424
		8152	1.380	3.084E-05	0.118	5.774	4.440	0.592
		7794	1.524	3.206E-05	0.116	5.837	4.552	0.704
		7334	1.683	3.431E-05	0.113	5.946	4.743	0.895
		6711	1.863	3.730E-05	0.108	6.079	4.975	1.127
		6005	2.029	4.077E-05	0.104	6.216	5.216	1.368
		5408	2.198	4.517E-05	0.100	6.370	5.487	1.639

Table 3.5. Continuation

$a_{i,cor}/W$	A_{i-el}	A_{i-pl}	$f(a_i/W)$	K_i	J_{el}	J_{pl}	J_{total}
	Nmm	Nmm		MPa m ^{0,5}	N/mm	N/mm	N/mm
0.385	238	1	1.901	37.2	6.2	0.0	6.2
0.371	438	96	1.833	49.7	11.0	3.0	14.0
0.378	635	300	1.864	60.2	16.2	9.3	25.4
0.377	796	712	1.861	67.4	20.3	22.0	42.2
0.380	905	1,287	1.878	72.1	23.2	39.7	62.9
0.382	955	1,940	1.884	74.2	24.5	59.9	84.5
0.385	1,010	2,634	1.901	76.5	26.1	81.3	107.5
0.395	1,059	3,470	1.953	79.2	28.0	107.2	135.2
0.399	1,077	4,396	1.976	80.2	28.7	135.8	164.5
0.403	1,065	5,388	2.001	80.2	28.7	166.4	195.1
0.415	1,088	6,426	2.065	82.1	30.0	198.5	228.5
0.422	1,082	7,464	2.106	82.5	30.3	230.5	260.9
0.427	1,036	8,676	2.139	81.2	29.4	267.9	297.4
0.444	1,025	9,965	2.245	82.4	30.3	307.8	338.0
0.455	974	11,170	2.321	81.4	29.5	345.0	374.5
0.474	923	12,433	2.458	81.1	29.4	384.0	413.3
0.498	840	13,786	2.642	79.8	28.4	425.8	454.2
0.522	735	14,948	2.855	77.2	26.6	461.7	488.2
0.549	660	15,991	3.128	76.1	25.9	493.9	519.7

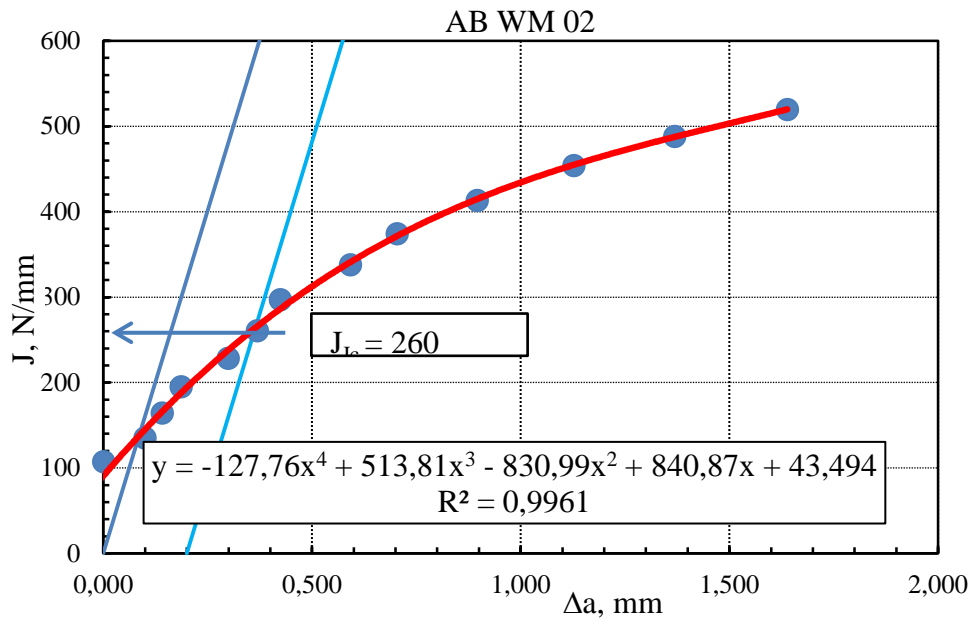


Fig. 3.39. J - R curve for specimen AB WM 02 using corrected crack lengths with measured after brittle fracture.

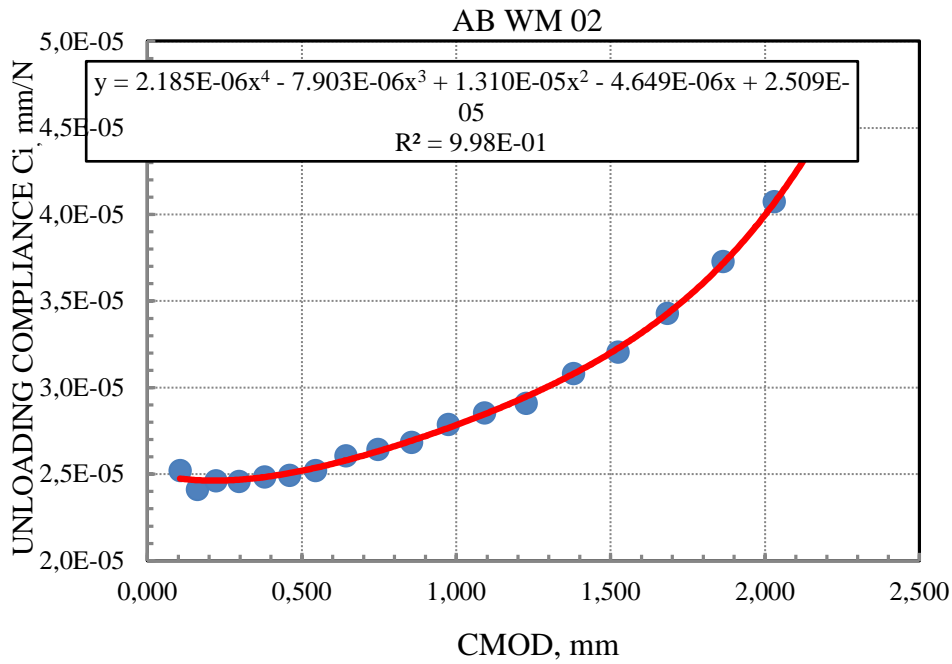


Figure 3.40. Fitting of compliances with CMOD distribution

Table 3.6. Assessment of specimen AB WM 02 using compliance fitting with CMOD

AB WM 02		F	$CMOD$	$C_{compliance}, C_i$	u_i	a_i/W	a_i	$a_i - cor,$
		N	mm	mm/N			mm	mm
B , mm	10	4347.2	0.106	2.474E-05	0.1299	0.540	5.397	3.848
W , mm	10	6027.4	0.162	2.466E-05	0.1301	0.540	5.397	3.848
S , mm	45	7179.1	0.222	2.463E-05	0.1302	0.540	5.396	3.845
a_{o-mes} , mm	3.848	8045.3	0.296	2.468E-05	0.1300	0.540	5.399	3.851
a_{f-mes} , mm	5.487	8533.6	0.378	2.483E-05	0.1297	0.541	5.410	3.868
a_{o-calc} , mm	5.397	8749.1	0.459	2.506E-05	0.1292	0.543	5.425	3.895
a_{f-calc} , mm	6.373	8947.2	0.544	2.536E-05	0.1285	0.545	5.446	3.930
$s_{0,2}$, MPa	768	9011.9	0.642	2.579E-05	0.1276	0.547	5.475	3.978
s_u , MPa	837	9024.9	0.746	2.632E-05	0.1264	0.551	5.509	4.036
s_{flow} , MPa	802.5	8908.2	0.855	2.693E-05	0.1252	0.555	5.548	4.101
E , GPa	204	8831.4	0.974	2.767E-05	0.1237	0.559	5.594	4.177
		8703.2	1.091	2.846E-05	0.1222	0.564	5.641	4.257
		8437.1	1.226	2.947E-05	0.1203	0.570	5.699	4.355
		8152.2	1.380	3.080E-05	0.1180	0.577	5.772	4.476
		7793.6	1.524	3.227E-05	0.1156	0.585	5.848	4.604
		7334.1	1.683	3.426E-05	0.1126	0.594	5.944	4.766
		6710.6	1.863	3.716E-05	0.1086	0.607	6.073	4.982
		6005.1	2.029	4.065E-05	0.1043	0.621	6.212	5.215
		5407.7	2.198	4.528E-05	0.0994	0.637	6.373	5.487

Table 3.6. Continuation

Δa_i	A_{i-el}	A_{i-pl}	$a_{i,cor}/W$	$f(a_i/W)$	K_i	J_{el}	J_{pl}	J_{total}
mm	Nmm	Nmm			MPa m ^{0,5}	N/mm	N/mm	N/mm
0.000	234	6	0.385	1.901	37.2	6.2	0.2	6.3
0.000	448	86	0.385	1.901	51.6	11.9	2.7	14.5
-0.003	635	300	0.384	1.899	61.4	16.8	9.3	26.1
0.003	799	709	0.385	1.902	68.9	21.2	21.9	43.1
0.020	904	1288	0.387	1.912	73.4	24.0	39.8	63.8
0.047	959	1936	0.389	1.925	75.8	25.6	59.8	85.4
0.082	1015	2629	0.393	1.944	78.3	27.3	81.2	108.5
0.130	1047	3482	0.398	1.970	79.9	28.5	107.5	136.0
0.188	1072	4401	0.404	2.002	81.3	29.5	135.9	165.4
0.253	1069	5385	0.410	2.038	81.7	29.8	166.3	196.1
0.329	1079	6435	0.418	2.083	82.8	30.6	198.7	229.3
0.409	1078	7468	0.426	2.130	83.4	31.0	230.6	261.7
0.507	1049	8663	0.435	2.191	83.2	30.9	267.5	298.4
0.628	1023	9967	0.448	2.270	83.3	30.9	307.8	338.7
0.756	980	11164	0.460	2.357	82.7	30.5	344.8	375.3
0.918	921	12434	0.477	2.476	81.7	29.8	384.0	413.8
1.134	837	13789	0.498	2.647	79.9	28.5	425.9	454.4
1.367	733	14950	0.522	2.854	77.1	26.5	461.7	488.3
1.639	662	15989	0.549	3.128	76.1	25.9	493.8	519.7

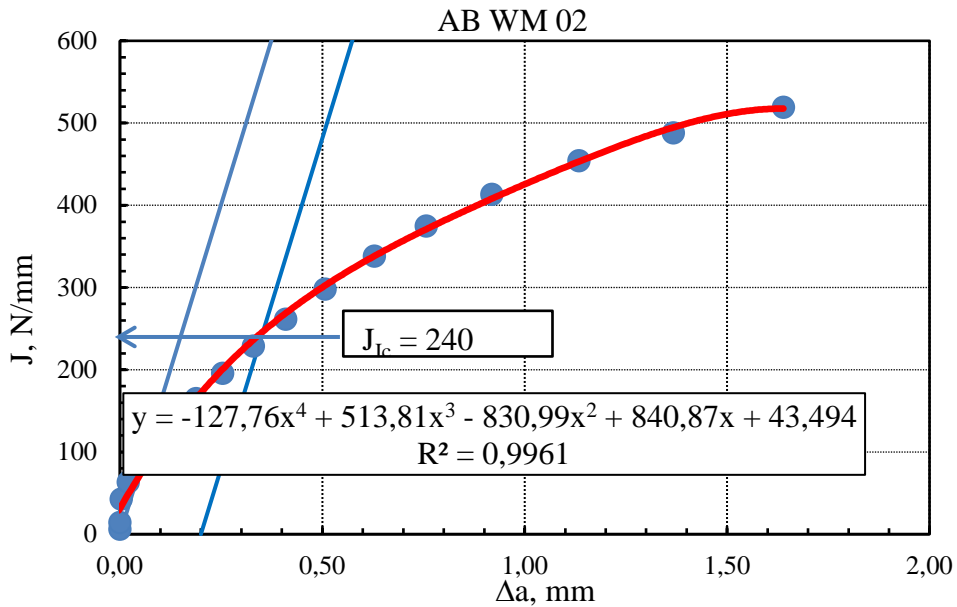


Figure 3.41. J - R curve for specimen AB WM 02 using compliance fitting procedure

Specimen AB WM 03 will be shortly presented with corrected crack lengths, Tab. 3.7, Fig. 3.42.

Table 3.7. Short assessment of AB WM 03 specimen with corrected crack lengths

AB WM 03		<i>CMOD</i>	<i>F</i>	<i>C_i</i>	<i>a_{i-cor}</i>	Δa_{cor}
		mm	N	mm/N	mm	mm
<i>B</i> , mm	10	0.108	3886.2	2.851E-05	3.923	0.000
<i>W</i> , mm	10	0.179	5525.8	2.684E-05	3.923	0.000
<i>S</i> , mm	45	0.226	6271.8	2.696E-05	3.938	0.015
<i>a_{o-mes}</i> , mm	3.923	0.271	6790.2	2.699E-05	3.941	0.018
<i>a_{f-mes}</i> , mm	5.243	0.316	7173.6	2.674E-05	3.951	0.028
<i>a_{o-calc}</i> , mm	5.542	0.372	7516.2	2.719E-05	3.964	0.041
<i>a_{f-calc}</i> , mm	6.255	0.425	7830.9	2.726E-05	3.972	0.049
<i>s_{0.2}</i> , MPa	768	0.485	8003.8	2.729E-05	3.975	0.052
<i>s_u</i> , MPa	837	0.548	8200.3	2.711E-05	3.975	0.052
<i>s_{flow}</i> , MPa	802.5	0.618	8316.2	2.751E-05	4.000	0.077
<i>E</i> , GPa	204	0.689	8384.9	2.790E-05	4.044	0.121
		0.762	8418.3	2.818E-05	4.075	0.152
		0.844	8379.6	2.852E-05	4.112	0.189
		0.943	8270.1	2.959E-05	4.225	0.302
		1.045	7978.2	3.083E-05	4.351	0.428
		1.156	7645.8	3.187E-05	4.451	0.528
		1.268	7170.0	3.396E-05	4.642	0.719
		1.388	6601.1	3.594E-05	4.808	0.885
		1.526	6040.6	3.857E-05	5.013	1.090
		1.684	5593.2	4.183E-05	5.243	1.320

Table 3.7. Continuation

A_{total}	A_{iel}	A_{ipl}	$a_{icor.}/W$	$f(a_i/W)$	K_i	J_{el}	J_{pl}	J_{total}
N·mm	N·mm	N·mm			MPa m ^{0.5}	N/mm	N/mm	N/mm
214	215	-1	0.392	1.940	33.9	5.1	0.0	5.1
553	410	143	0.392	1.940	48.2	10.4	4.5	14.9
832	530	301	0.394	1.948	55.0	13.5	9.4	22.9
1129	622	506	0.394	1.950	59.6	15.8	15.8	31.7
1443	688	755	0.395	1.955	63.1	17.8	23.6	41.4
1856	768	1088	0.396	1.962	66.4	19.7	34.0	53.7
2267	836	1431	0.397	1.967	69.3	21.4	44.7	66.2
2740	874	1866	0.398	1.968	70.9	22.4	58.3	80.8
3253	911	2342	0.398	1.968	72.6	23.5	73.2	96.8
3832	951	2880	0.400	1.982	74.2	24.5	90.1	114.6
4425	981	3444	0.404	2.006	75.7	25.6	107.7	133.2
5041	998	4043	0.408	2.024	76.7	26.2	126.4	152.6
5738	1001	4737	0.411	2.045	77.1	26.5	148.1	174.6
6563	1012	5551	0.423	2.111	78.6	27.5	173.6	201.1
7400	981	6419	0.435	2.188	78.6	27.5	200.7	228.2
8265	931	7333	0.445	2.253	77.5	26.8	229.3	256.1
9104	873	8231	0.464	2.384	76.9	26.4	257.3	283.7
9927	783	9144	0.481	2.508	74.5	24.7	285.9	310.7
10805	704	10101	0.501	2.674	72.7	23.6	315.8	339.4
11727	654	11072	0.524	2.881	72.5	23.4	346.2	369.6

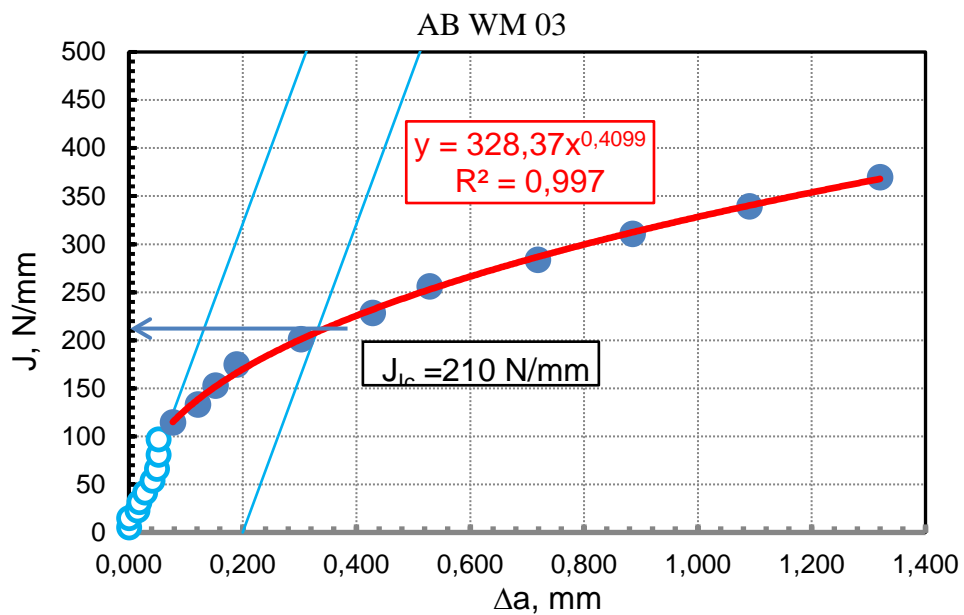


Figure 3.42. Experimental J - R curve for AB WM 03 with corrected crack lengths

It is also convenient to put together all WM specimens to get confidence in appropriate procedure assessment used, to present two curves: Load vs. CMOD and J – R curves, Fig. 3.43-3.44.

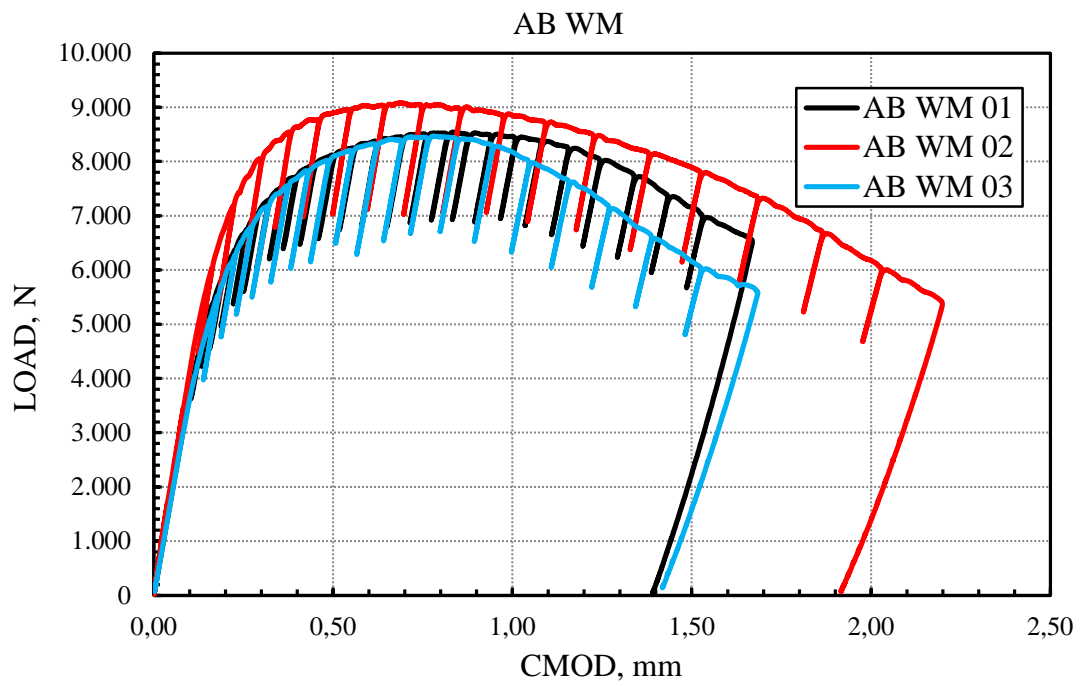


Figure 3.43. Load vs. CMOD distribution for all three WM specimens

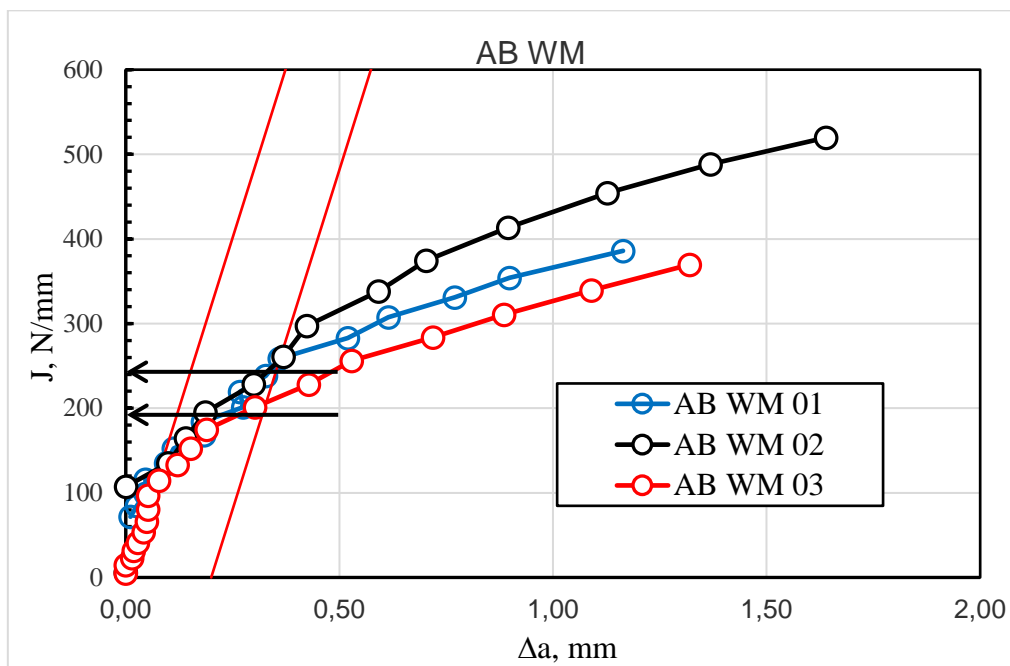


Figure 3.44. The J - R curves for all WM specimens evaluated with crack lengths correction

3.4.2 Fracture toughness testing of HAZ

Results for fracture toughness testing with crack positioned in HAZ will be present in a shorter form because complete procedure is shown for WM specimens. They are presented also for 3 specimens in Figs. 3.45-3.48 and Tables 3.8-3.14.

Table 3.8. Data assessment of specimen AB HAZ 01 with corrected crack lengths

AB HAZ 01		<i>CMOD</i>	<i>Load</i>	<i>Compliance</i>	u_i	a_i	$a_{i\text{cor}}$	Δa_i
		mm	N	mm/N		mm	mm	mm
B , mm	10	0.122	4508	2.6796E-05	0.1239	5.589	3.982	0.000
W , mm	10	0.221	6694	2.7419E-05	0.1226	5.627	4.045	0.063
S , mm	45	0.296	7478	2.8172E-05	0.1212	5.672	4.118	0.136
$a_{o\text{-mes}}$, mm	3.982	0.368	7933	2.7840E-05	0.1218	5.653	4.086	0.104
$a_{f\text{-mes}}$, mm	5.3	0.455	8286	2.7872E-05	0.1218	5.655	4.089	0.107
$a_{o\text{-calc}}$, mm	5.363	0.548	8560	2.7758E-05	0.1220	5.648	4.078	0.096
$a_{f\text{-calc}}$, mm	6.040	0.648	8773	2.8143E-05	0.1212	5.671	4.115	0.133
$\sigma_{0.2}$, MPa	768	0.747	8945	2.8462E-05	0.1206	5.689	4.146	0.164
σ_u , MPa	837	0.856	9057	2.8547E-05	0.1205	5.694	4.154	0.172
σ_{flow} , MPa	802.5	0.972	9124	2.8820E-05	0.1200	5.710	4.180	0.198
E , GPa	204	1.102	9157	2.9021E-05	0.1196	5.722	4.198	0.216
		1.219	9177	2.8642E-05	0.1203	5.700	4.163	0.181
		1.369	9081	2.8970E-05	0.1197	5.719	4.194	0.212
		1.521	8964	2.9707E-05	0.1184	5.760	4.261	0.279
		1.706	8775	3.0652E-05	0.1168	5.811	4.344	0.362
		1.895	8518	3.1121E-05	0.1160	5.836	4.384	0.402
		2.080	8288	3.2160E-05	0.1143	5.889	4.471	0.489
		2.288	8044	3.2861E-05	0.1132	5.924	4.527	0.545
		2.499	7808	3.4507E-05	0.1108	6.002	4.654	0.672
		2.713	7582	3.7214E-05	0.1071	6.120	4.846	0.864
		2.954	7288	3.9956E-05	0.1038	6.229	5.024	1.042
		3.219	6981	4.1611E-05	0.1019	6.291	5.123	1.141
		3.511	6656	4.1993E-05	0.1015	6.304	5.146	1.164
		3.816	6361	4.4766E-05	0.0986	6.399	5.300	1.318

Table 3.8. Continuation

a_i/W	$A_{i\text{total}}$	A_{iel}	A_{ipl}	$f(a_i/W)$	K_i	J_{el}	J_{pl}	J_{total}
	N·mm	N·mm	N·mm		MPa m ^{0,5}	N/mm	N/mm	N/mm
0.398	277	272	5	1.972	40.00	7.1	0.2	7.3
0.404	846	614	232	2.007	60.45	16.3	7.3	23.6
0.412	1,383	788	596	2.048	68.93	21.2	18.8	40.0
0.409	1,945	876	1,069	2.030	72.46	23.4	33.7	57.2
0.409	2,650	957	1,693	2.032	75.75	25.6	53.5	79.1
0.408	3,433	1,017	2,416	2.025	78.01	27.1	76.3	103.4
0.412	4,302	1,083	3,219	2.047	80.80	29.1	101.6	130.8
0.415	5,181	1,139	4,043	2.064	83.08	30.8	127.6	158.4
0.415	6,164	1,171	4,993	2.069	84.32	31.7	157.6	189.3
0.418	7,219	1,200	6,019	2.084	85.56	32.7	190.0	222.7
0.420	8,417	1,217	7,200	2.095	86.32	33.2	227.3	260.6
0.416	9,489	1,206	8,283	2.074	85.66	32.7	261.5	294.2
0.419	10,863	1,195	9,668	2.092	85.49	32.6	305.3	337.9
0.426	12,235	1,194	11,042	2.132	86.02	33.0	348.6	381.6
0.434	13,877	1,180	12,697	2.184	86.24	33.2	400.9	434.0
0.438	15,519	1,129	14,390	2.210	84.69	32.0	454.3	486.3
0.447	17,072	1,105	15,968	2.266	84.51	31.9	504.1	536.0
0.453	18,774	1,063	17,710	2.304	83.40	31.0	559.2	590.2
0.465	20,447	1,052	19,396	2.392	84.05	31.5	612.4	643.9
0.485	22,103	1,070	21,034	2.537	86.56	33.4	664.1	697.5
0.502	23,888	1,061	22,827	2.682	87.98	34.5	720.7	755.2
0.512	25,784	1,014	24,770	2.770	87.01	33.8	782.0	815.8
0.515	27,774	930	26,844	2.790	83.56	31.1	847.5	878.7
0.530	29,766	906	28,861	2.936	84.03	31.5	911.2	942.7

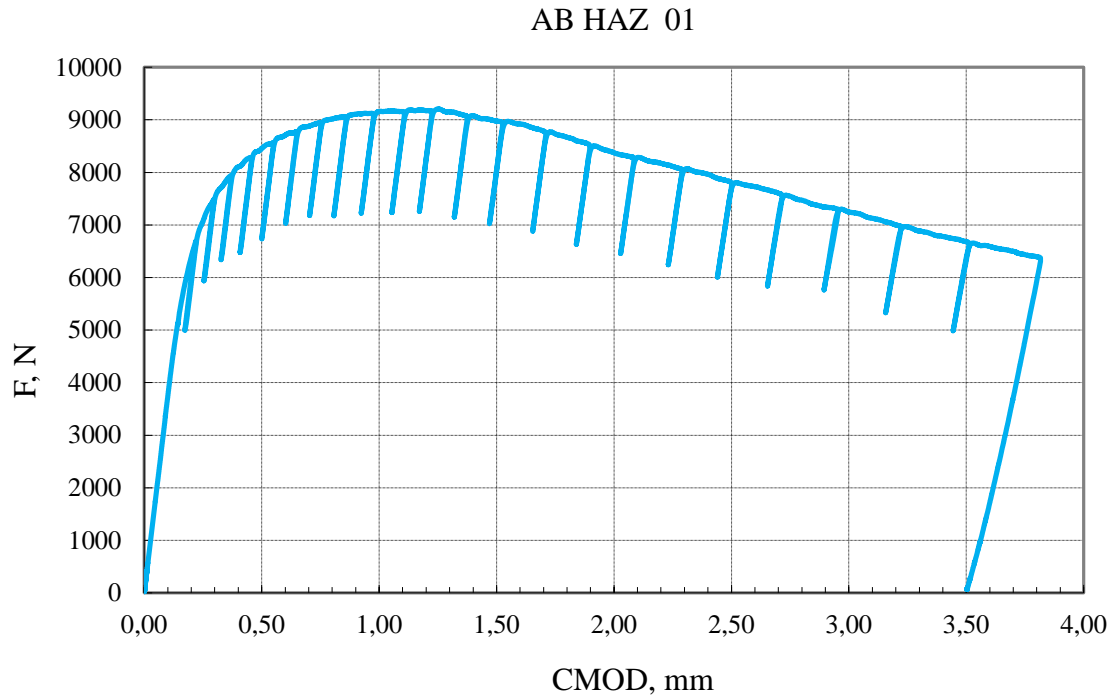


Figure 3.45. Load vs, CMOD for AB HAZ 01 specimen

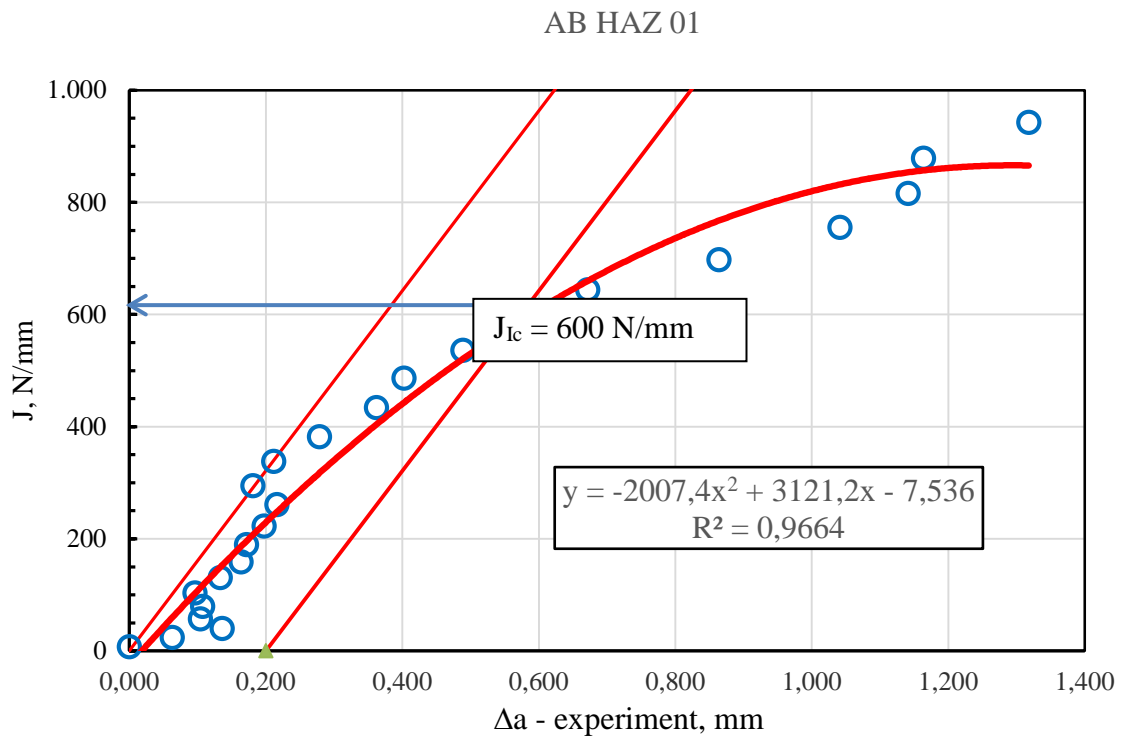


Figure 3.46. $J - R$ curve for specimen AB HAZ 01 with crack lengths correction

It is obvious that data scatter is expressed and J_{Ic} value is not easy to evaluate so it will be used fitted compliance with change of CMOD. On the next figures will be shown compliance fit and $J-R$ curve for fitted data.

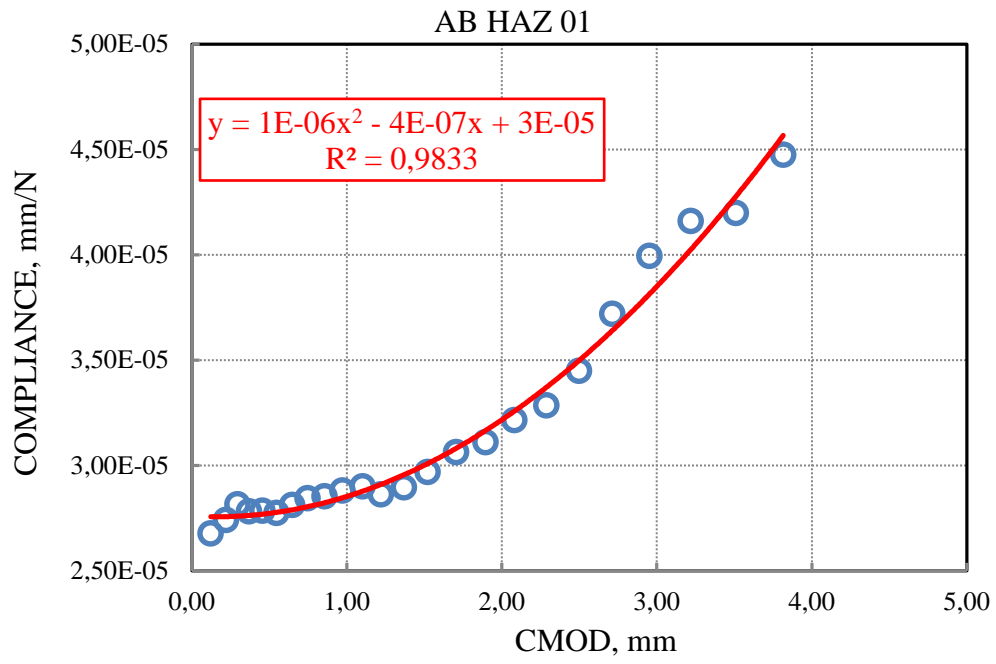


Figure 3.47. Fitted curve for compliance with CMOD

Table 3.9. Specimen AB HAZ 01 assessed with compliance fitting

AB HAZ 01		<i>CMOD</i>	<i>Load</i>	<i>C_i-fit</i>	<i>u_i</i>	<i>a_i-cor</i> ,	Δa_i
		mm	N	mm/N		mm	mm
<i>B</i> , mm	10	0.122	4508	2.748E-05	0.123	3.982	0.000
<i>W</i> , mm	10	0.221	6694	2.749E-05	0.122	3.984	0.002
<i>S</i> , mm	45	0.296	7478	2.752E-05	0.122	3.987	0.005
<i>a_o-mes</i> , mm	3.982	0.368	7933	2.756E-05	0.122	3.992	0.010
<i>a_f-mes</i> , mm	5.3	0.455	8286	2.763E-05	0.122	4.000	0.018
<i>a_o-calc</i> , mm	5.363	0.548	8560	2.773E-05	0.122	4.012	0.030
<i>a_f-calc</i> , mm	6.040	0.648	8773	2.785E-05	0.122	4.027	0.045
$\sigma_{0,2}$, MPa	768	0.747	8945	2.801E-05	0.121	4.044	0.062
σ_u , MPa	837	0.856	9057	2.821E-05	0.121	4.067	0.085
σ_{flow} , MPa	802.5	0.972	9124	2.845E-05	0.121	4.095	0.113
<i>E</i> , GPa	204	1.102	9157	2.877E-05	0.120	4.131	0.149
		1.219	9177	2,910E-05	0.119	4.167	0.185
		1.369	9081	2,957E-05	0.119	4.219	0.237
		1.521	8964	3,010E-05	0.118	4.276	0.294
		1.706	8775	3,084E-05	0.116	4.353	0.371
		1.895	8518	3,168E-05	0.115	4.438	0.456
		2.080	8288	3,260E-05	0.114	4.528	0.546
		2.288	8044	3,374E-05	0.112	4.635	0.653
		2.499	7808	3,501E-05	0.110	4.749	0.767
		2.713	7582	3,643E-05	0.108	4.870	0.888
		2.954	7288	3,816E-05	0.106	5.010	1.028
		3.219	6981	4,025E-05	0.103	5.168	1.186
		3.511	6656	4,276E-05	0.101	5.346	1.364
		3.816	6361	4,563E-05	0.098	5.532	1.550

Table 3.9. Continuation

a_i/W	A_{tot}	A_{iel}	A_{ipl}	$f(a_i/W)$	K_i	J_{el}	J_{pl}	J_{total}
	N·mm	N·mm	N·mm		MPa·m ^{0.5}	N/mm	N/mm	N/mm
0.398	277	279	-2	1.972	40.0	7.1	-0.1	7.1
0.398	846	616	230	1.973	59.4	15.8	7.3	23.0
0.399	1383	770	614	1.975	66.5	19.7	19.4	39.1
0.399	1945	867	1078	1.978	70.6	22.2	34.0	56.3
0.400	2650	949	1701	1.982	73.9	24.4	53.7	78.1
0.401	3433	1016	2417	1.988	76.6	26.2	76.3	102.5
0.403	4302	1072	3230	1.996	78.8	27.7	102.0	129.7
0.404	5181	1120	4061	2.006	80.8	29.1	128.2	157.3
0.407	6164	1157	5007	2.019	82.3	30.2	158.1	188.3
0.410	7219	1184	6034	2.035	83.6	31.1	190.5	221.7
0.413	8417	1206	7211	2.056	84.7	32.0	227.7	259.7
0.417	9489	1225	8264	2.077	85.8	32.8	260.9	293.7
0.422	10863	1219	9644	2.107	86.1	33.1	304.5	337.6
0.428	12235	1209	11026	2.142	86.4	33.3	348.1	381.4
0.435	13877	1187	12690	2.189	86.5	33.3	400.6	434.0
0.444	15519	1149	14369	2.245	86.0	33.0	453.7	486.7
0.453	17072	1120	15952	2.304	85.9	33.0	503.7	536.6
0.463	18774	1092	17682	2.379	86.1	33.1	558.3	591.3
0.475	20447	1067	19380	2.462	86.5	33.4	611.9	645.3
0.487	22103	1047	21056	2.556	87.2	33.9	664.8	698.7
0.501	23888	1014	22874	2.671	87.6	34.2	722.2	756.4
0.517	25784	981	24803	2.811	88.3	34.8	783.1	817.8
0.535	27774	947	26827	2.981	89.3	35.6	847.0	882.5
0.553	29766	923	28843	3.178	91.0	36.9	910.6	947.6

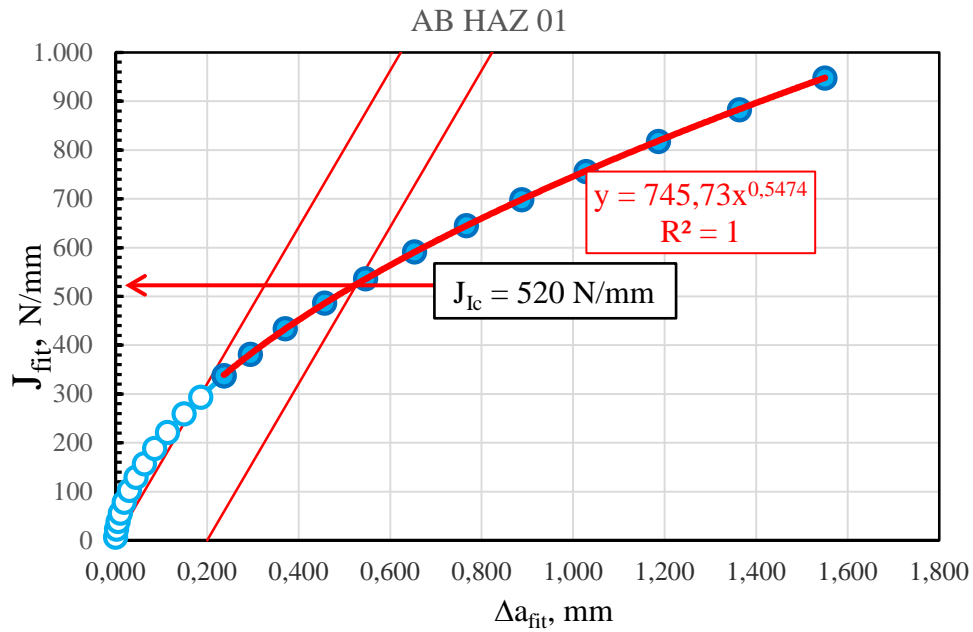


Figure 3.48. *J-R* curve for fitted compliances with CMOD changes

It is clear that compliance fitting procedure give us smooth *J-R* curve and lower J_{Ic} value. If we have better instrumentation this will be not so dramatic. Another problem is position of crack in HAZ zone and crack will try to enter constituent with lower tensile properties. Specimen AB HAZ 02 will be presented in shorter form because previous specimens are represented more complex and there is no reason to repeat all procedure for all specimens.

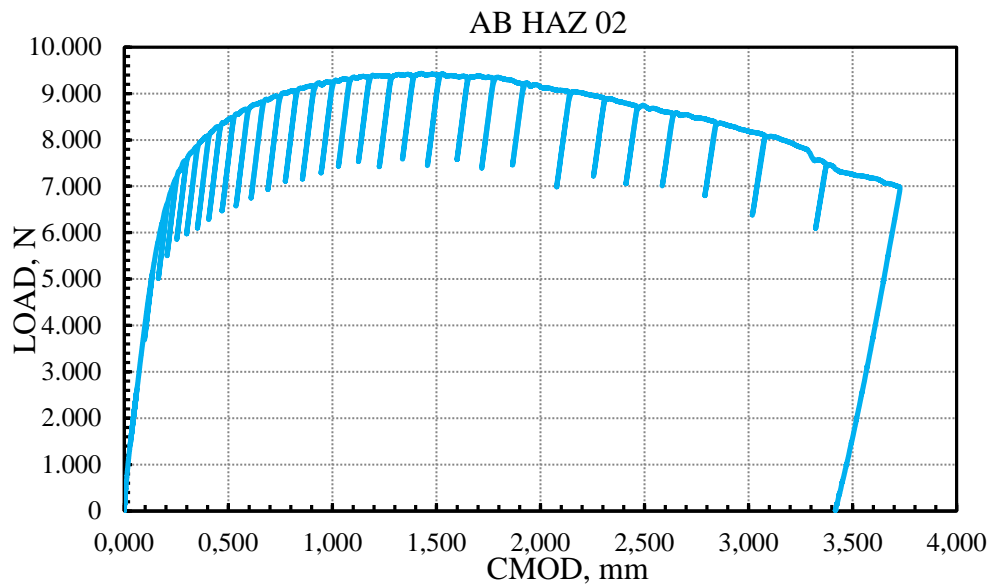


Figure 3.52. Load – CMOD for specimen AB HAZ 02

Table 3.10. Data evaluation of specimen AB HAZ 02

AB HAZ 02		F	$CMOD$	$Compliance$	$a_{icorr.}$	$\Delta a_{icorr.}$	a_i/W
		N	mm	mm/N	mm	mm	
B , mm	10	4,579	0.116	2.754E-05	3.905	0.000	0.391
W , mm	10	4,960	0.132	2.681E-05	3.781	-0.124	0.378
S , mm	45	6,586	0.207	2.704E-05	3.821	-0.084	0.382
$a_{o-mes.}$, mm	3.905	7,033	0.248	2.684E-05	3.786	-0.119	0.379
$a_{f-mes.}$, mm	5.641	7,382	0.294	2.709E-05	3.829	-0.076	0.383
$a_{o-calc.}$, mm	5.781	7,607	0.345	2.731E-05	3.866	-0.039	0.387
$a_{f-calc.}$, mm	6.400	7,786	0.398	2.705E-05	3.822	-0.083	0.382
$\sigma_{0.2}$, MPa	768	8,032	0.454	2.702E-05	3.818	-0.087	0.382
σ_u , MPa	837	8,170	0.517	2.727E-05	3.860	-0.045	0.386
σ_{flow} , MPa	802.5	8,133	0.580	2.723E-05	3.853	-0.052	0.385
E , GPa	204	8,110	0.647	2.735E-05	3.874	-0.031	0.387
		8,496	0,734	2.740E-05	3.882	-0.023	0.388
		8,640	0,817	2.766E-05	3.926	0.021	0.393
		8,643	0,898	2.756E-05	3.908	0.003	0.391
		8,698	0,986	2.751E-05	3.901	-0.004	0.390
		8,857	1,070	2.793E-05	3.970	0.065	0.397
		8,868	1,164	2.818E-05	4.011	0.106	0.401
		9,076	1,273	2.840E-05	4.045	0.140	0.405
		9,194	1,384	2.864E-05	4.085	0.180	0.408
		9,074	1,504	2.841E-05	4.047	0.142	0.405
		9,079	1,644	2.906E-05	4.150	0.245	0.415
		9,006	1,765	2.924E-05	4.179	0.274	0.418
		8,918	1,910	2.986E-05	4.274	0.369	0.427
		8,810	2,135	3.067E-05	4.393	0.488	0.439
		8,609	2,299	3.120E-05	4.470	0.565	0.447
		8,450	2,455	3.196E-05	4.577	0.672	0.458
		7,636	2,606	3.366E-05	4.805	0.900	0.480
		7,243	2,805	3.457E-05	4.921	1.016	0.492
		6,790	3,032	3.589E-05	5.082	1.177	0.508
		6,519	3,338	3.785E-05	5.308	1.403	0.531
		6,992	3,724	4.099E-05	5.641	1.736	0.564

Table 3.10. Continuation

$f(a_i/W)$	A_{iel}	A_{ipl}	K_i	J_{el}	J_{pl}	J_{total}
	N·mm	N·mm	MPa m ^{0.5}	N/mm	N/mm	N/mm
1.931	289	-7	39.8	7.1	-0.2	6.8
1.867	330	25	41.7	7.7	0.8	8.5
1.887	587	215	55.9	14.0	6.7	20.7
1.869	664	418	59.2	15.6	13.0	28.6
1.891	738	705	62.8	17.6	22.0	39.6
1.910	790	1038	65.4	19.1	32.4	51.4
1.888	820	1443	66.1	19.5	45.0	64.5
1.886	872	1845	68.2	20.7	57.5	78.2
1.907	910	2341	70.1	21.9	73.0	94.9
1.903	900	2942	69.7	21.6	91.7	113.3
1.915	900	3556	69.9	21.8	110.9	132.6
1.919	989	4201	73.3	24.0	131.0	155.0
1.942	1032	4900	75.5	25.4	152.8	178.2
1.932	1029	5649	75.2	25.2	176.1	201.3
1.928	1041	6451	75.5	25.4	201.1	226.5
1.966	1096	7146	78.3	27.4	222.8	250.1
1.988	1108	8007	79.3	28.1	249.6	277.7
2.007	1170	8931	82.0	30.0	278.4	308.4
2.029	1210	9903	83.9	31.4	308.7	340.1
2.008	1170	11089	82.0	30.0	345.7	375.7
2.067	1198	12369	84.4	31.8	385.6	417.4
2.084	1186	13574	84.4	31.8	423.1	455.0
2.140	1188	14871	85.9	32.9	463.6	496.5
2.215	1190	16934	87.8	34.4	527.9	562.3
2.265	1156	18470	87.8	34.4	575.8	610.1
2.338	1141	19846	88.9	35.3	618.7	653.9
2.505	981	21509	86.1	33.0	670.5	703.5
2.597	907	23367	84.6	32.0	728.4	760.4
2.733	827	25377	83.5	31.1	791.1	822.2
2.944	804	27695	86.4	33.3	863.3	896.6
3.302	1002	30076	103.9	48.2	937.6	985.7

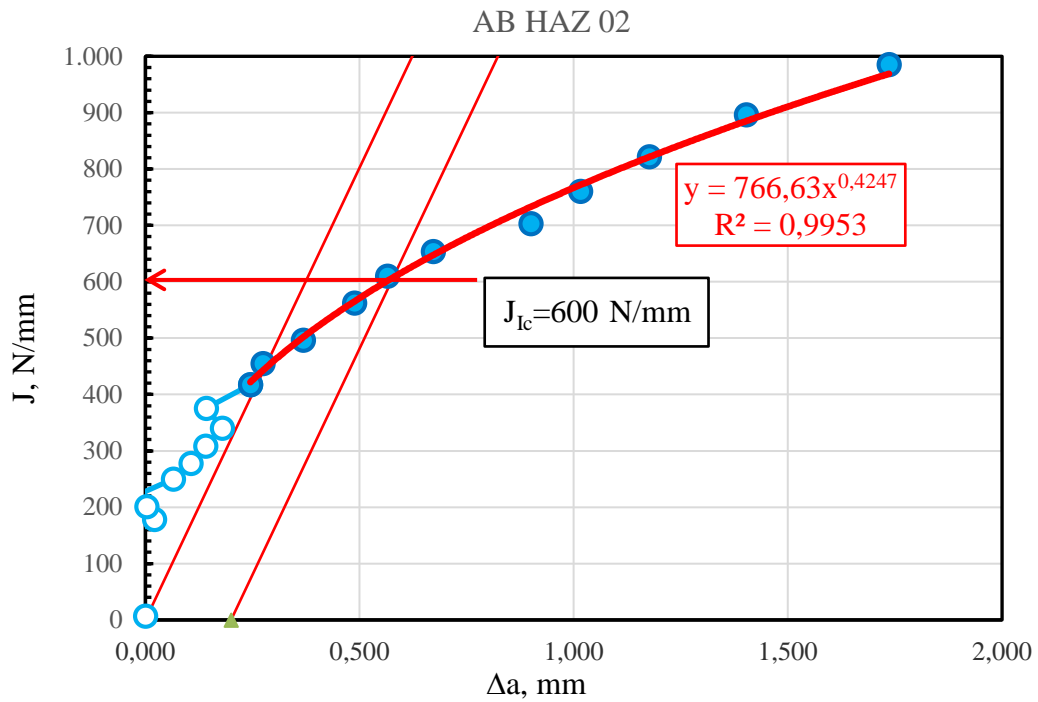


Figure 3.53. Evaluation of J_{Ic} using corrected a_i values with experimentally obtained ones

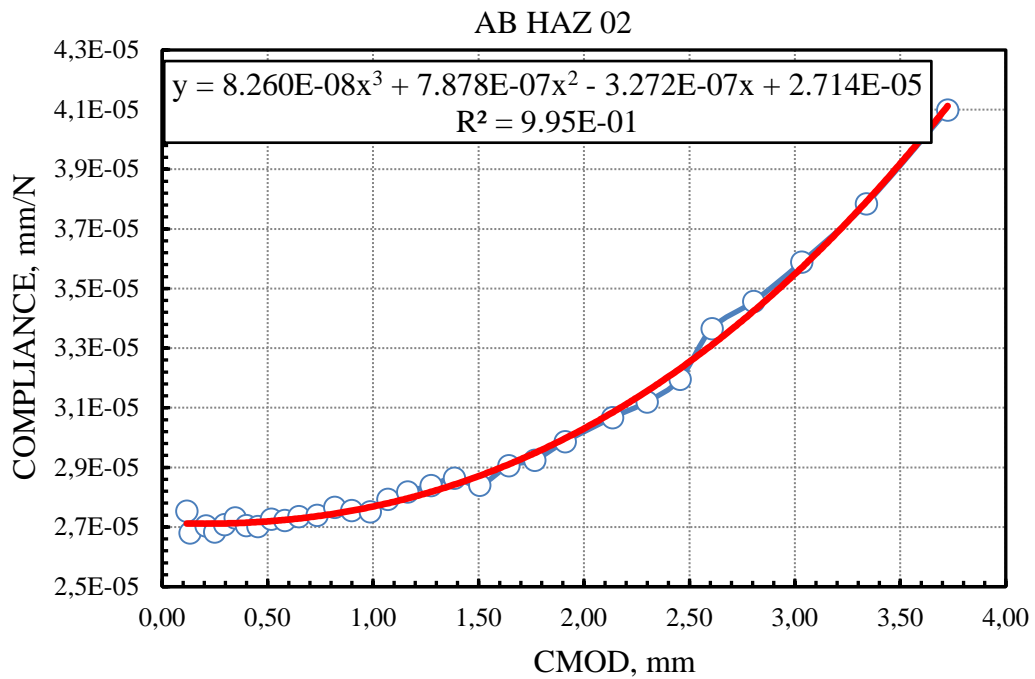


Figure 3.54. Compliance fitted with CMOD

Table 3.11. Data evaluation of specimen AB HAZ 02 with fitted compliances

AB HAZ 02		F	$CMOD$	$C_{i,fit}$	a_i/W	a_i	Δa_i
		N	mm	mm/N		mm	mm
B , mm	10	4579	0.116	2.712E-05	0.5756	3.905	0.000
W , mm	10	4960	0.132	2.712E-05	0.5756	3.905	0.000
S , mm	45	6586	0.207	2.711E-05	0.5756	3.904	-0.001
$a_{o-mes,}$ mm	3.905	7033	0.248	2.711E-05	0.5756	3.904	-0.001
$a_{f-mes,}$ mm	5.641	7382	0.294	2.712E-05	0.5756	3.905	0.000
$a_{o-calc,}$ mm	5.781	7607	0.345	2.713E-05	0.5757	3.907	0.002
$a_{f-calc,}$ mm	6.400	7786	0.398	2.714E-05	0.5758	3.909	0.004
$\sigma_{0.2}$, MPa	768	8032	0.454	2.717E-05	0.5759	3.913	0.008
σ_u , MPa	837	8170	0.517	2.720E-05	0.5761	3.918	0.013
σ_{flow} , MPa	802.5	8133	0.580	2.724E-05	0.5763	3.924	0.019
E , GPa	204	8110	0.647	2.729E-05	0.5766	3.932	0.027
		8496	0.734	2.736E-05	0.5771	3.944	0.039
		8640	0.817	2.745E-05	0.5776	3.958	0.053
		8643	0.898	2.755E-05	0.5782	3.974	0.069
		8698	0.986	2.767E-05	0.5789	3.993	0.088
		8857	1.070	2.780E-05	0.5797	4.014	0.109
		8868	1.164	2.796E-05	0.5806	4.039	0.134
		9076	1.273	2.818E-05	0.5819	4.073	0.168
		9194	1.384	2.842E-05	0.5833	4.110	0.205
		9074	1.504	2.872E-05	0.5850	4.155	0.250
		9079	1.644	2.910E-05	0.5871	4.213	0.308
		9006	1.765	2.948E-05	0.5892	4.268	0.363
		8918	1.910	2.997E-05	0.5919	4.339	0.434
		8810	2.135	3.084E-05	0.5964	4.462	0.557
		8609	2.299	3.156E-05	0.6001	4.560	0.655
		8450	2.455	3.231E-05	0.6038	4.660	0.755
		7636	2.606	3.311E-05	0.6076	4.761	0.856
		7243	2.805	3.425E-05	0.6129	4.902	0.997
		6790	3.032	3.570E-05	0.6193	5.073	1.168
		6519	3.338	3.790E-05	0.6284	5.317	1.412
		6992	3.724	4.112E-05	0.6405	5.641	1.736

Table 3.11. Continuation

a_i/W	$f(a_i/W)$	A_{iel}	A_{ipl}	K_i	J_{el}	J_{pl}	J_{total}
		N·mm	N·mm	MPa·m ^{0.5}	N/mm	N/mm	N/mm
0.3905	1.9307	284.3	-2.9	39.8	7.1	-0.1	7.0
0.3905	1.9305	333.6	21.7	43.1	8.3	0.7	9.0
0.3904	1.9302	588.0	213.9	57.2	14.6	6.7	21.3
0.3904	1.9303	670.6	410.8	61.1	16.6	12.8	29.5
0.3905	1.9308	738.9	704.4	64.1	18.4	22.0	40.3
0.3907	1.9317	785.0	1043.0	66.1	19.5	32.5	52.0
0.3909	1.9330	822.8	1440.1	67.7	20.5	44.9	65.4
0.3913	1.9349	876.3	1840.7	69.9	21.8	57.4	79.2
0.3918	1.9376	907.7	2343.5	71.2	22.6	73.1	95.7
0.3924	1.9409	900.7	2941.4	71.0	22.5	91.7	114.2
0.3932	1.9451	897.3	3558.3	71.0	22.5	110.9	133.4
0.3944	1.9517	987.4	4202.8	74.6	24.8	131.0	155.8
0.3958	1.9591	1024.4	4908.5	76.2	25.9	153.0	178.9
0.3974	1.9675	1028.8	5649.2	76.5	26.1	176.1	202.2
0.3993	1.9780	1046.6	6444.8	77.4	26.7	200.9	227.6
0.4014	1.9893	1090.4	7151.3	79.3	28.0	222.9	251.0
0.4039	2.0035	1099.4	8016.0	79.9	28.5	249.9	278.4
0.4073	2.0222	1160.5	8939.8	82.6	30.4	278.7	309.1
0.4110	2.0436	1201.1	9912.3	84.5	31.9	309.0	340.9
0.4155	2.0696	1182.2	11076.0	84.5	31.9	345.3	377.1
0.4213	2.1036	1199.5	12367.5	85.9	33.0	385.5	418.5
0.4268	2.1370	1195.6	13564.6	86.6	33.5	422.9	456.3
0.4339	2.1810	1191.7	14866.6	87.5	34.2	463.4	497.6
0.4462	2.2600	1196.7	16927.7	89.6	35.8	527.7	563.5
0.4560	2.3262	1169.4	18456.9	90.1	36.2	575.4	611.6
0.4660	2.3967	1153.7	19833.4	91.1	37.1	618.3	655.3
0.4761	2.4717	965.1	21525.1	84.9	32.2	671.0	703.2
0.4902	2.5818	898.2	23376.0	84.1	31.6	728.7	760.3
0.5073	2.7257	823.0	25381.5	83.3	30.9	791.2	822.2
0.5317	2.9521	805.5	27693.7	86.6	33.5	863.3	896.8
0.5641	3.3021	1005.2	30073.0	103.9	48.2	937.5	985.6

Fitting compliance data with CMOD will give smooth J - R curve and reduced J_{Ic} from 600 to 550 N/mm, Fig. 3.55.

Results for the third specimen, AB HAZ03 are presented in Figures 3.56 and in Table 3.12.

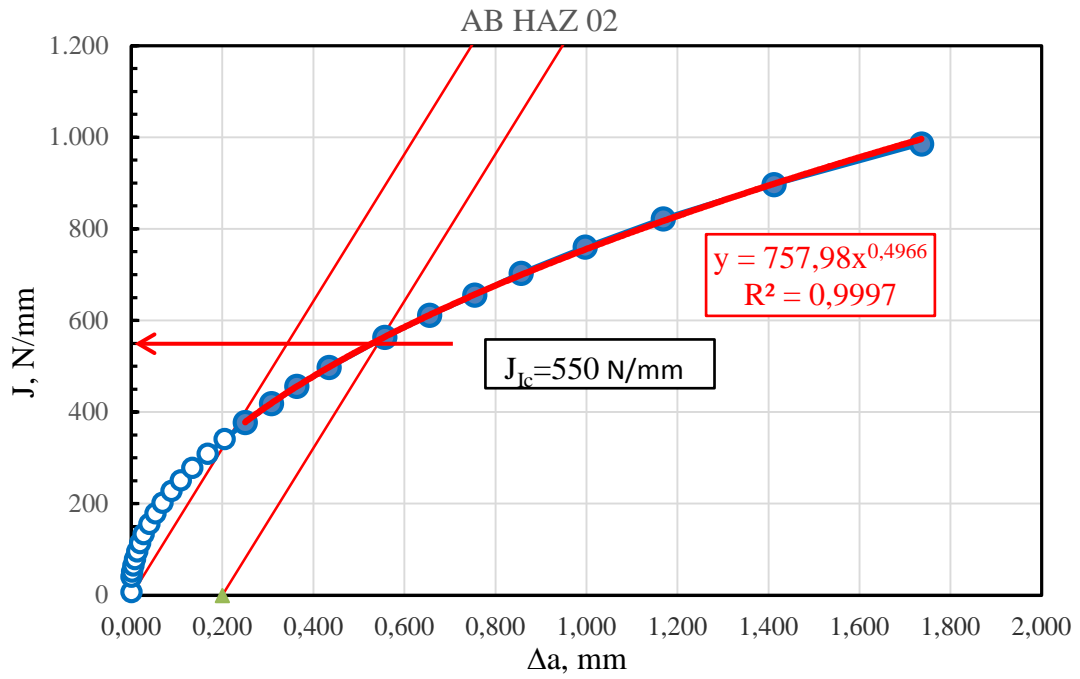


Figure 3.55. *J-R* curve for specimen AB HAZ 02 using fitted compliance data

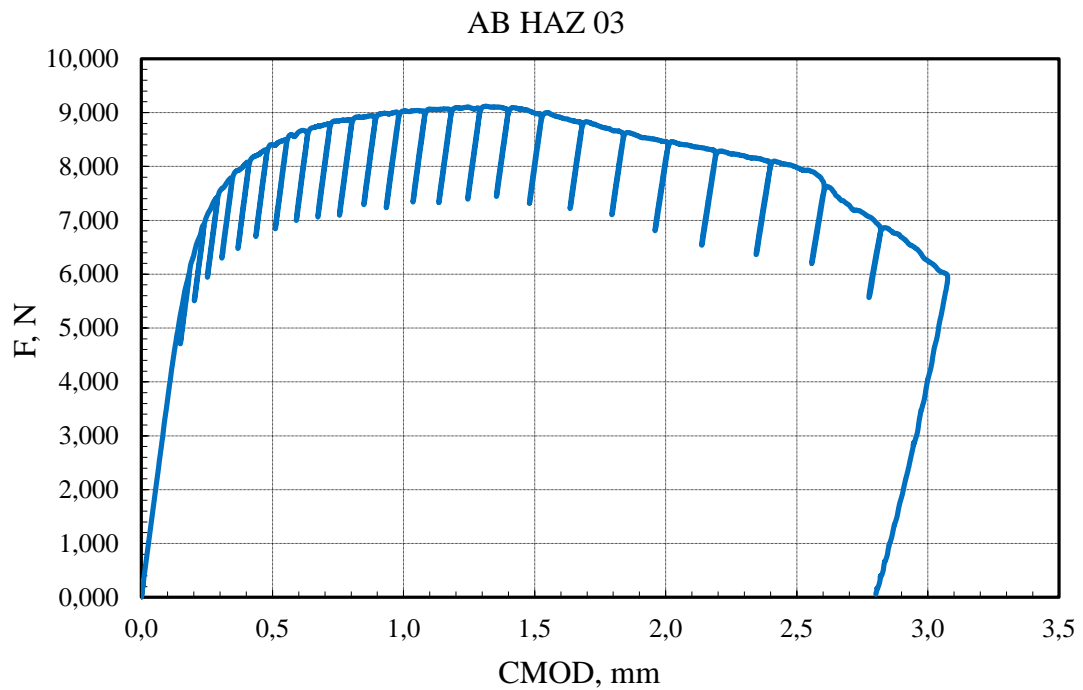


Figure 3.56. Load vs, CMOD distribution for specimen AB HAZ 03

Table 3.12. Evaluation of specimen AB HAZ 03 with corrected crack lengths according to the experimentally obtained values

AB HAZ 03		<i>CMOD</i>	<i>F</i>	<i>Compliance,</i> <i>C_i</i>	<i>a_{icorr},</i>	Δa_i	<i>a_{ic}/W</i>
		mm	N	mm/N	mm	mm	
<i>B</i> , mm	10	0.108	3,999	2.691E-05	3.678	0.000	0.368
<i>W</i> , mm	10	0.181	5,995	2.699E-05	3.690	0.012	0.369
<i>S</i> , mm	45	0.237	6,896	2.691E-05	3.678	0.000	0.368
<i>a_{o-mes}</i> , mm	3.678	0.287	7,424	2.691E-05	3.678	0.000	0.368
<i>a_{f-mes}</i> , mm	5.2	0.340	7,784	2.734E-05	3.746	0.068	0.375
<i>a_{o-calc}</i> , mm	5.547	0.403	8,075	2.685E-05	3.668	-0.010	0.367
<i>a_{f-calc}</i> , mm	6.151	0.472	8,308	2.687E-05	3.672	-0.006	0.367
$\sigma_{0,2}$, MPa	768	0.550	8,491	2.678E-05	3.657	-0.021	0.366
σ_u , MPa	837	0.631	8,631	2.688E-05	3.674	-0.004	0.367
σ_{flow} , MPa	802.5	0.713	8,792	2.757E-05	3.781	0.103	0.378
<i>E</i> , GPa	204	0.796	8,870	2.752E-05	3.773	0.095	0.377
		0.886	8.940	2,780E-05	3.817	0.139	0.382
		0.977	8.996	2,811E-05	3.863	0.185	0.386
		1.075	9.033	2,791E-05	3.833	0.155	0.383
		1.174	9.061	2,819E-05	3.876	0.198	0.388
		1.285	9.081	2,822E-05	3.880	0.202	0.388
		1.394	9.061	2,867E-05	3.946	0.268	0.395
		1.523	8.968	2,852E-05	3.925	0.247	0.392
		1.676	8.818	2,957E-05	4.075	0.397	0.407
		1.834	8.630	3,033E-05	4.181	0.503	0.418
		2.004	8.456	3,147E-05	4.333	0.655	0.433
		2.186	8.298	3,176E-05	4.371	0.693	0.437
		2.394	8.093	3,266E-05	4.485	0.807	0.448
		2.602	7.697	3,374E-05	4.618	0.940	0.462
		2.818	6.874	3,647E-05	4.928	1.250	0.493
		3.072	5.997	3,908E-05	5.200	1.522	0.520

Table 3.12. Continuation

A_{total}	A_{iel}	A_{ipl}	$f(a_i/W)$	K_i	J_{el}	J_{pl}	J_{total}
N·mm	N·mm	N·mm		MPa m ^{0.5}	N/mm	N/mm	N/mm
217.9	215.2	2.6	1.816	32.7	4.8	0.1	4.8
585.0	485.0	100.0	1.822	49.1	10.8	3.0	13.8
951.4	639.8	311.6	1.816	56.3	14.2	9.4	23.5
1,307.6	741.6	566.1	1.815	60.7	16.4	17.0	33.4
1,714.8	828.5	886.3	1.849	64.8	18.7	26.6	45.4
2,216.5	875.4	1,341.1	1.811	65.8	19.3	40.3	59.6
2,783.4	927.5	1,855.9	1.813	67.8	20.5	55.8	76.3
3,433.7	965.2	2,468.5	1.805	69.0	21.2	74.2	95.4
4,132.8	1001.3	3,131.4	1.814	70.4	22.1	94.1	116.2
4,846.5	1065.6	3,780.9	1.867	73.8	24.3	113.6	138.0
5,582.5	1082.7	4,499.8	1.863	74.4	24.7	135.2	159.9
6,383.7	1111.1	5,272.6	1.885	75.8	25.6	158.5	184.1
7,199.1	1137.4	6,061.7	1.908	77.3	26.6	182.2	208.8
8,083.1	1138.7	6,944.4	1.893	77.0	26.4	208.7	235.1
8,981.1	1157.4	7,823.7	1.915	78.1	27.2	235.1	262.3
9,996.6	1163.6	8,832.9	1.917	78.4	27.4	265.5	292.8
10,983.2	1176.9	9,806.3	1.953	79.6	28.3	294.7	323.0
12,147.4	1147.0	11,000.4	1.941	78.3	27.4	330.6	358.0
13,516.7	1149.5	12,367.3	2.023	80.3	28.8	371.7	400.4
14,896.2	1129.4	13,766.9	2.084	81.0	29.2	413.7	443.0
16,350.3	1125.1	15,225.3	2.177	82.8	30.6	457.6	488.2
17,869.0	1093.5	16,775.5	2.201	82.2	30.1	504.2	534.3
19,579.5	1069.5	18,510.1	2.275	82.9	30.6	556.3	586.9
21,240.5	999.6	20,240.9	2.367	82.0	30.0	608.3	638.3
22,807.3	861.4	21,945.8	2.603	80.5	28.9	659.6	688.5
24,454.2	702.8	23,751.4	2.840	76.6	26.2	713.8	740.0

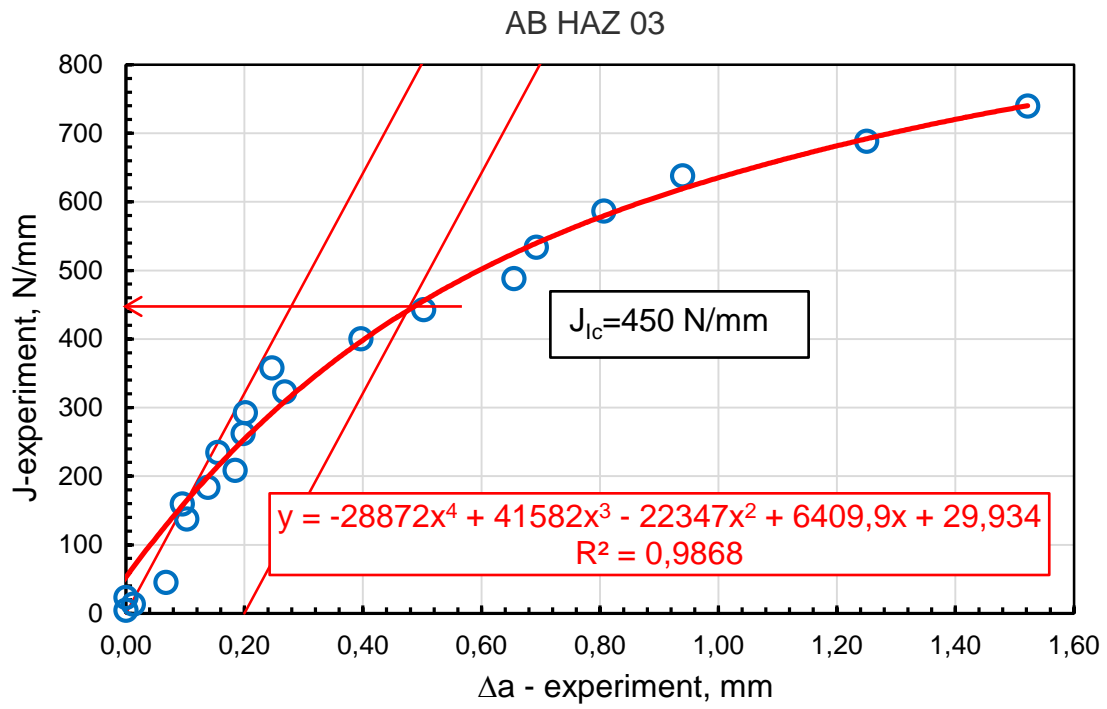


Figure 3.57. *J-R* curve of specimen AB HAZ 02 with corrected crack lengths

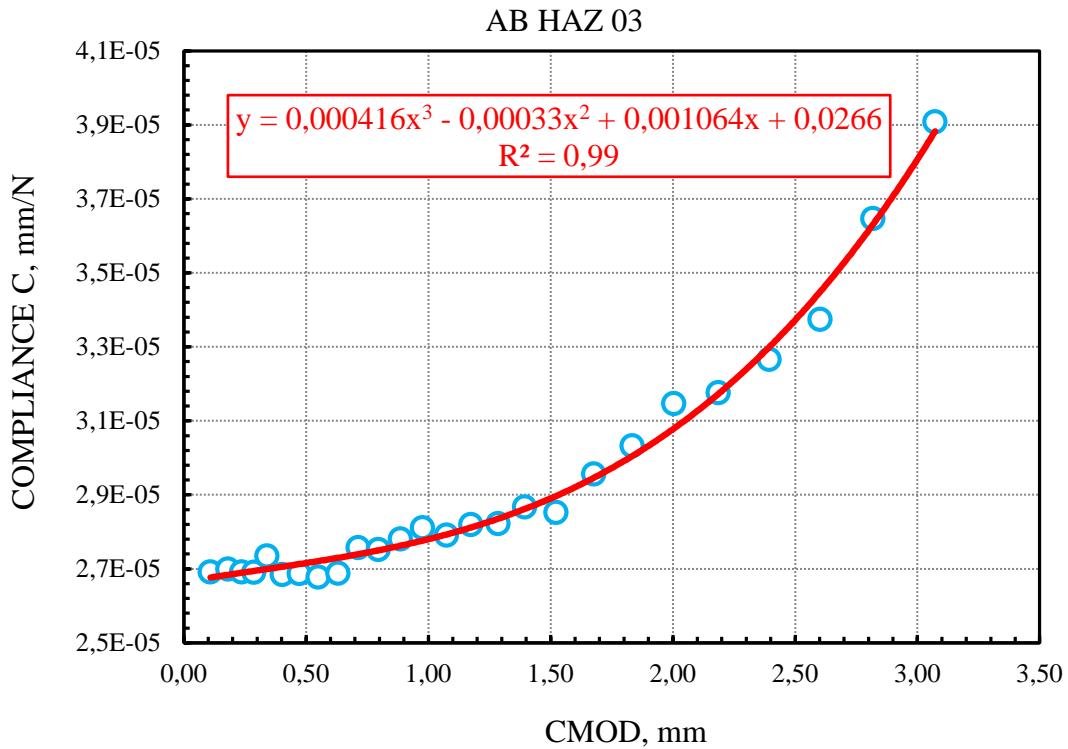


Figure 3.58. Fitted compliance of specimen AB HAZ 03 with CMOD

Table 3.13. Data evaluation of specimen AB HAZ 02 for fitted compliance

AB HAZ 03		<i>CMOD</i>	<i>F</i>	<i>Compliance, Cifit</i>	<i>aicorr,</i>	Δa_i	a_{ic}/W
		mm	N	mm/N	mm	mm	
<i>B</i> , mm	10	mm	N	mm/N	mm	mm	
<i>W</i> , mm	10	0.108	3.999	2.677E-05	3.678	0.000	0.368
<i>S</i> , mm	45	0.181	5.995	2.684E-05	3.689	0.011	0.369
<i>a_{o-mes}</i> , mm	3.678	0.237	6.896	2.689E-05	3.698	0.020	0.370
<i>a_{f-mes}</i> , mm	5.2	0.287	7.424	2.694E-05	3.706	0.028	0.371
<i>a_{o-calc}</i> , mm	5.538	0.340	7.784	2.699E-05	3.714	0.036	0.371
<i>a_{f-calc}</i> , mm	6.141	0.403	8.075	2.706E-05	3.724	0.046	0.372
$\sigma_{0,2}$, MPa	768	0.472	8.308	2.713E-05	3.735	0.057	0.373
σ_u , MPa	837	0.550	8.491	2.721E-05	3.748	0.070	0.375
σ_{flow} , MPa	802.5	0.631	8.631	2.730E-05	3.762	0.084	0.376
<i>E</i> , GPa	204	0.713	8.792	2.739E-05	3.777	0.099	0.378
		0.796	8.870	2.750E-05	3.793	0.115	0.379
		0.886	8.940	2.762E-05	3.812	0.134	0.381
		0.977	8.996	2.776E-05	3.833	0.155	0.383
		1.075	9.033	2.793E-05	3.858	0.180	0.386
		1.174	9.061	2.812E-05	3.887	0.209	0.389
		1.285	9.081	2.835E-05	3.922	0.244	0.392
		1.394	9.061	2.862E-05	3.961	0.283	0.396
		1.523	8.968	2.897E-05	4.012	0.334	0.401
		1.676	8.818	2.946E-05	4.083	0.405	0.408
		1.834	8.630	3.005E-05	4.165	0.487	0.417
		2.004	8.456	3.080E-05	4.267	0.589	0.427
		2.186	8.298	3.173E-05	4.390	0.712	0.439
		2.394	8.093	3.300E-05	4.550	0.872	0.455
		2.602	7.697	3.449E-05	4.729	1.051	0.473
		2.818	6.874	3.631E-05	4.934	1.256	0.493
		3.072	5.997	3.883E-05	5.198	1.520	0.520

Table 3.13. Continuation

$A_{i\text{total}}$	A_{iel}	A_{ipl}	$f(a_i/W)$	K_i	J_{el}	J_{pl}	J_{total}
N·mm	N·mm	N·mm		MPa m ^{0.5}	N/mm	N/mm	N/mm
217.9	214.1	3.8	1.816	32.7	4.8	0.1	4.9
585.0	482.3	102.7	1.821	49.1	10.8	3.1	13.9
951.4	639.4	312.0	1.825	56.6	14.3	9.4	23.7
1,307.6	742.5	565.1	1.829	61.1	16.7	17.0	33.6
1,714.8	817.9	896.9	1.833	64.2	18.4	27.0	45.4
2,216.5	882.2	1,334.3	1.838	66.8	19.9	40.1	60.0
2,783.4	936.2	1,847.2	1.844	68.9	21.2	55.5	76.7
3,433.7	980.8	2,452.9	1.850	70.7	22.3	73.7	96.0
4,132.8	1016.8	3,116.0	1.857	72.1	23.2	93.6	116.9
4,846.5	1058.9	3,787.7	1.864	73.8	24.3	113.8	138.1
5,582.5	1081.9	4,500.6	1.873	74.7	24.9	135.3	160.2
6,383.7	1104.0	5,279.7	1.882	75.7	25.6	158.7	184.3
7,199.1	1123.5	6,075.6	1.893	76.6	26.2	182.6	208.8
8,083.1	1139.4	6,943.7	1.906	77.5	26.8	208.7	235.5
8,981.1	1154.2	7,826.9	1.921	78.3	27.4	235.2	262.6
9,996.6	1169.1	8,827.5	1.940	79.3	28.0	265.3	293.3
10,983.2	1174.7	9,808.5	1.961	79.9	28.5	294.8	323.3
12,147.4	1164.9	10,982.5	1.989	80.3	28.7	330.1	358.8
13,516.7	1145.4	12,371.4	2.028	80.5	28.9	371.8	400.7
14,896.2	1119.1	13,777.1	2.076	80.6	29.0	414.1	443.0
16,350.3	1101.0	15,249.3	2.136	81.3	29.5	458.3	487.8
17,869.0	1092.4	16,776.6	2.213	82.6	30.5	504.2	534.7
19,579.5	1080.6	18,498.9	2.319	84.5	31.8	556.0	587.8
21,240.5	1021.9	20,218.6	2.448	84.8	32.1	607.6	639.7
22,807.3	857.7	21,949.5	2.608	80.7	29.0	659.7	688.7
24,454.2	698.3	23,755.9	2.838	76.6	26.2	714.0	740.1

Using fitted compliance data shows good agreement for all three HAZ specimens.

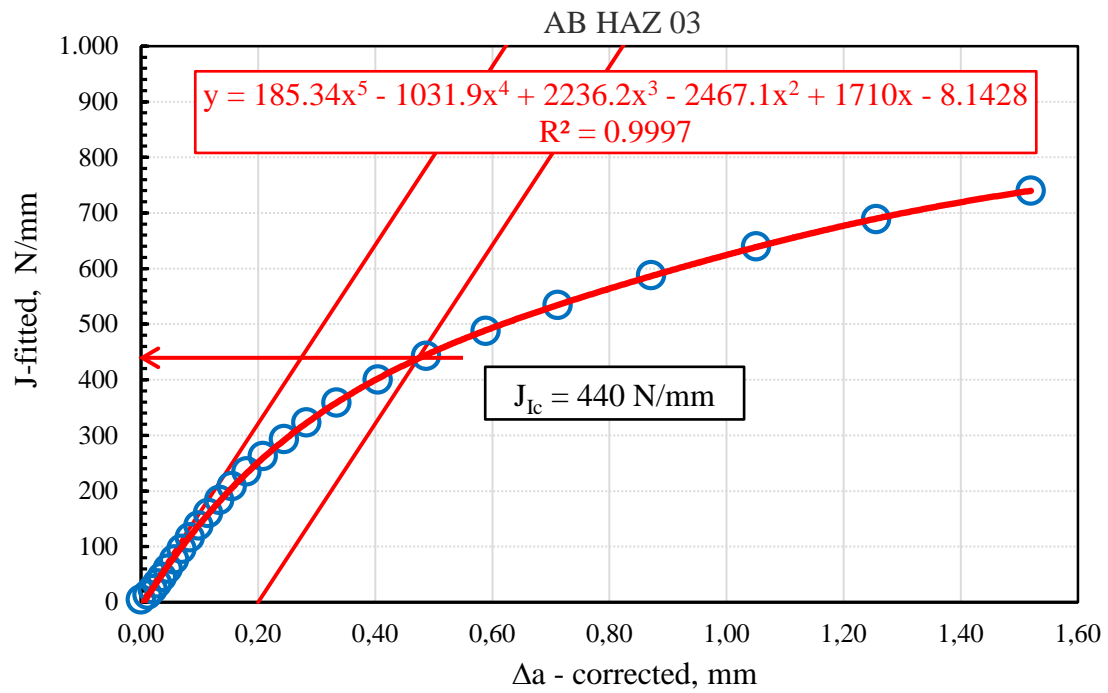


Figure 3.59. J - R curve for specimen AB HAZ 03 for fitted compliance data

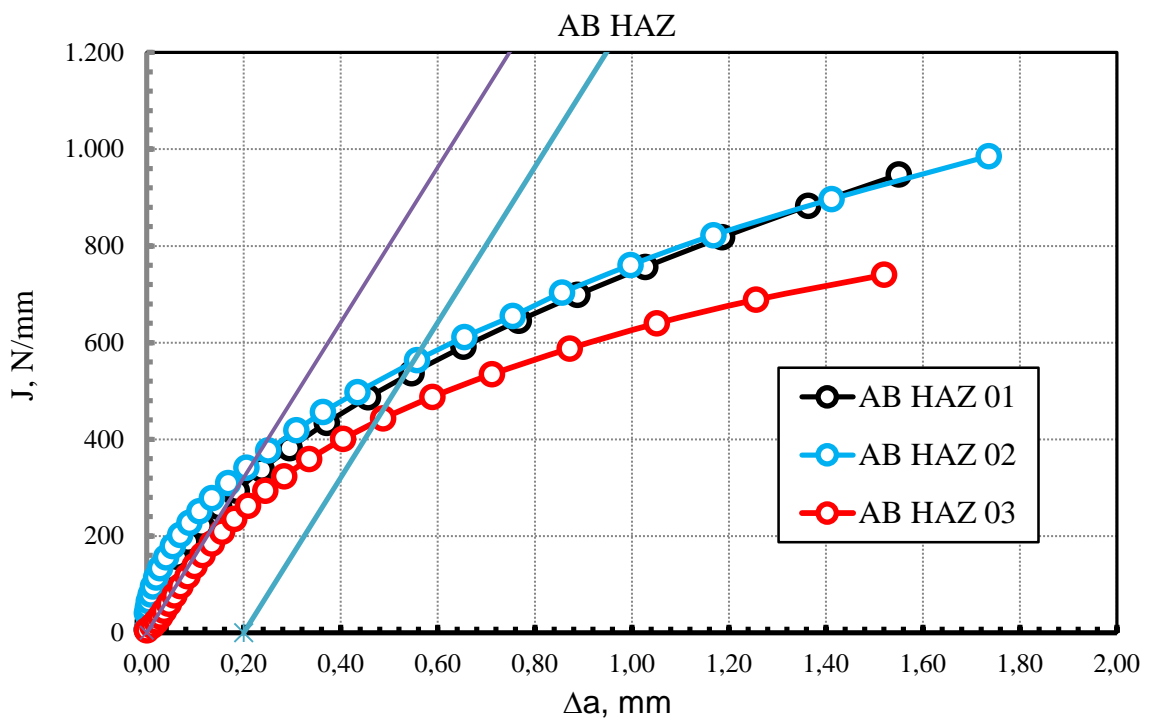


Figure 3.60. Comparison of HAZ specimen J - R curves using fitted compliance data

Table 3.14. Data evaluation of specimen AB PM 01 for corrected crack length values

AB PM 01		<i>CMOD</i>	<i>Load, F</i>	<i>Compliance</i>	<i>a_{icor.}</i>	Δa_i
		mm	N	mm/N	mm	mm
<i>B</i> , mm	10	0.122	4507.8	2.680E-05	3.982	0.000
<i>W</i> , mm	10	0.221	6694.1	2.742E-05	4.035	0.053
<i>S</i> , mm	45	0.296	7478.4	2.817E-05	4.098	0.070
<i>a_{o-mes.}</i> , mm	3.982	0.368	7932.9	2.784E-05	4.070	0.088
<i>a_{f-mes.}</i> , mm	5.101	0.455	8286.3	2.787E-05	4.073	0.091
<i>a_{o-calc.}</i> , mm	5.363	0.548	8559.7	2.776E-05	4.064	0.095
<i>a_{f-calc.}</i> , mm	6.040	0.648	8773.3	2.814E-05	4.095	0.113
$\sigma_{0.2}$, MPa	654	0.747	8944.6	2.846E-05	4.121	0.139
σ_u , MPa	820	0.856	9057.4	2.855E-05	4.128	0.146
σ_{flow} , MPa	737	0.972	9124.3	2.882E-05	4.150	0.168
<i>E</i> , GPa	200.4	1.102	9156.8	2.902E-05	4.166	0.184
		1.219	9177.4	2.864E-05	4.136	0.185
		1.369	9081.3	2.897E-05	4.162	0.190
		1.521	8964.0	2.971E-05	4.219	0.237
		1.706	8775.1	3.065E-05	4.290	0.308
		1.895	8517.9	3.112E-05	4.324	0.342
		2.080	8288.4	3.216E-05	4.397	0.415
		2.288	8044.3	3.286E-05	4.445	0.463
		2.499	7807.6	3.451E-05	4.552	0.570
		2.713	7582.1	3.721E-05	4.716	0.734
		2.954	7288.3	3.996E-05	4.866	0.884
		3.219	6980.5	4.161E-05	4.951	0.969
		3.511	6655.7	4.199E-05	4.970	0.988
		3.816	6360.8	4.477E-05	5.101	1.119

Table 3.14. Continuation

a_i/w	A_{iel}	A_{ipl}	$f(a_i/W)$	K_i	J_{el}	J_{pl}	J_{total}
	N·mm	N·mm		MPa m ^{0.5}	N/mm	N/mm	N/mm
0.398	272	5	1.972	40.00	6.9	0.2	7.1
0.404	614	232	2.001	60.29	15.7	7.3	23.1
0.410	788	596	2.036	68.53	20.4	18.8	39.2
0.407	876	1069	2.021	72.14	22.6	33.7	56.3
0.407	957	1693	2.022	75.41	24.6	53.5	78.1
0.406	1017	2416	2.017	77.70	26.2	76.3	102.4
0.410	1083	3219	2.035	80.34	28.0	101.6	129.6
0.412	1139	4043	2.050	82.51	29.5	127.6	157.1
0.413	1171	4993	2.054	83.71	30.4	157.6	188.0
0.415	1200	6019	2.066	84.84	31.2	190.0	221.2
0.417	1217	7200	2.076	85.53	31.7	227.3	259.0
0.414	1206	8283	2.058	85.00	31.3	261.5	292.8
0.416	1195	9668	2.073	84.73	31.1	305.3	336.4
0.422	1194	11042	2.107	84.99	31.3	348.6	379.9
0.429	1180	12697	2.150	84.90	31.2	400.9	432.1
0.432	1129	14390	2.171	83.22	30.0	454.3	484.3
0.440	1105	15968	2.218	82.71	29.6	504.1	533.8
0.444	1063	17710	2.249	81.40	28.7	559.2	587.9
0.455	1052	19396	2.321	81.55	28.8	612.4	641.2
0.472	1070	21034	2.438	83.17	30.0	664.1	694.0
0.487	1061	22827	2.553	83.73	30.4	720.7	751.1
0.495	1014	24770	2.622	82.35	29.4	782.0	811.4
0.497	930	26844	2.637	78.99	27.0	847.5	874.6
0.510	906	28861	2.750	78.71	26.8	911.2	938.0

3.4.3. Fracture toughness testing of PM

Results for fracture mechanics testing of PM are shown in Figs. 3.61-3.64 and Table 3.15. In the case of PM, the results for only one specimen are presented, since PM is consisting of homogeneous microstructure.

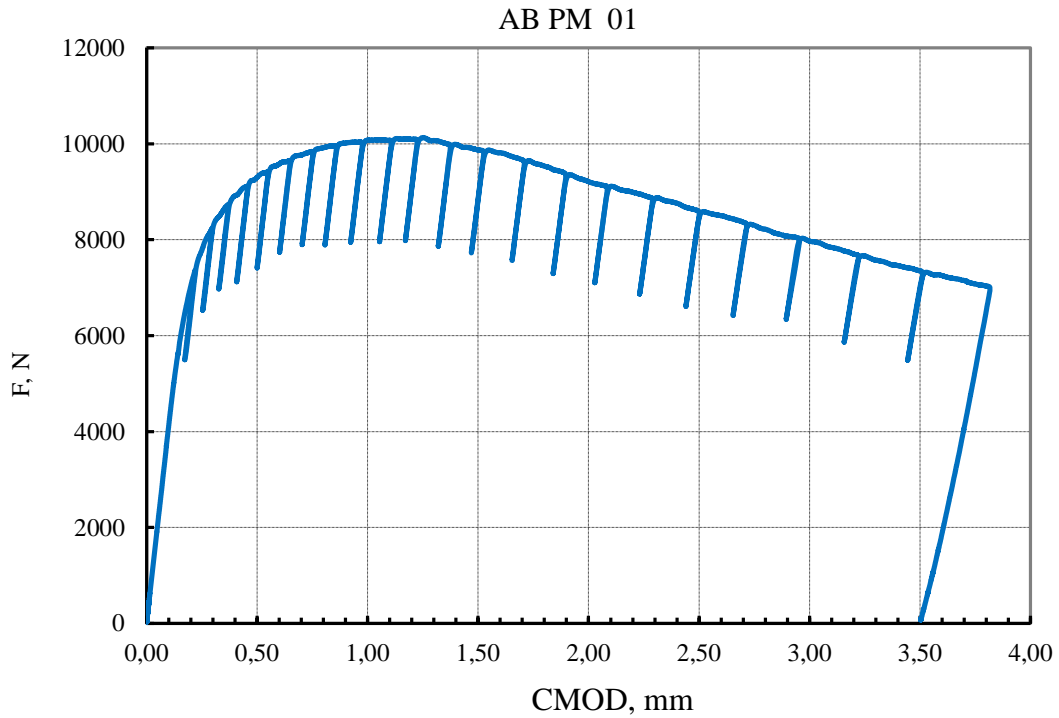


Figure 3.61. Load vs, CMOD distribution for specimen AB PM 01

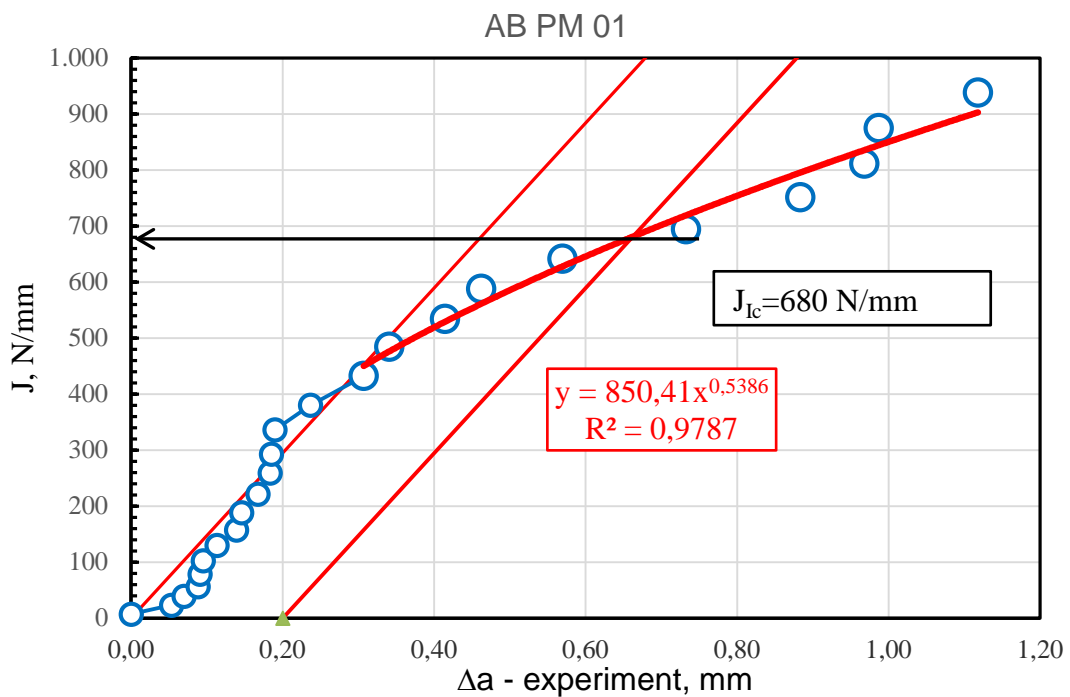


Figure 3.62. *J*-integral vs *a* for specimen AB PM 01

For the same AB PM 01 specimen data will be evaluated with compliance vs. CMOD fitted data. Fitting procedure is shown in Fig. 3.63.

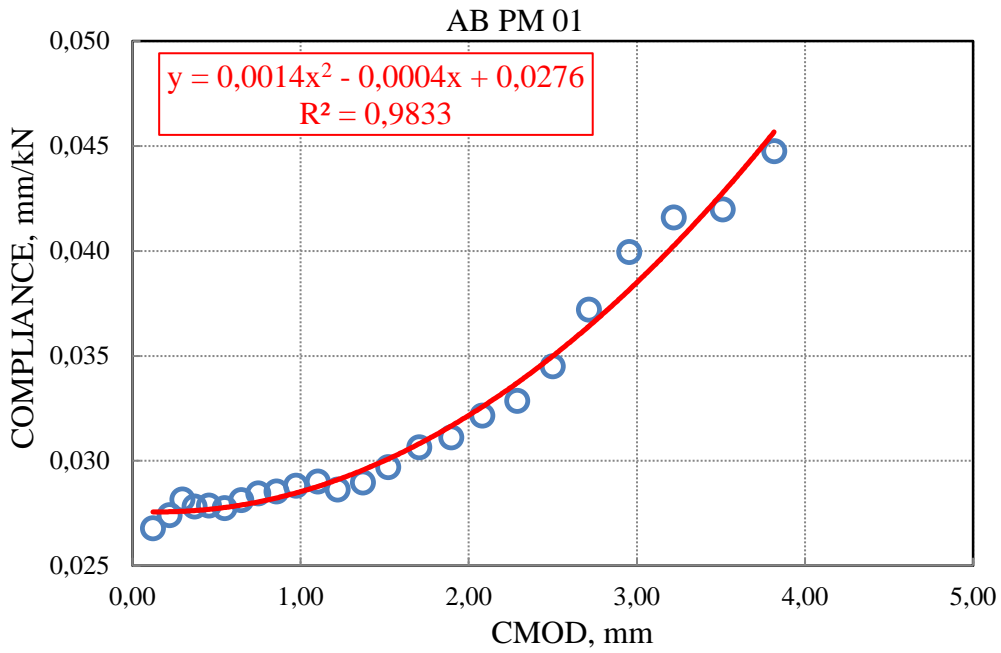


Figure 3.63. Fitting of compliance with change of CMOD

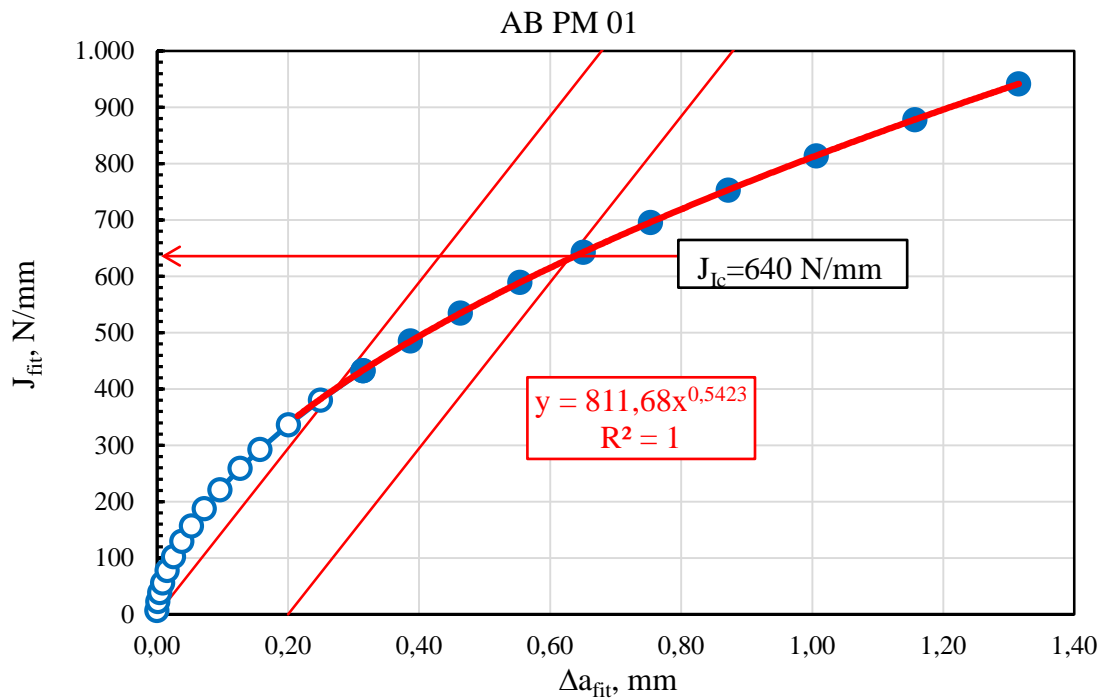


Figure 3.64. J_{fit} vs. a_{fit} for specimen AB PM 01

Table 3.15. Data evaluation of specimen AB PM 01 for fitted compliance data

AB PM 01		<i>CMOD</i>	<i>Load, F</i>	<i>Compliance</i>	<i>a_{icorr.}</i>	Δa_i
		mm	N	mm/N	mm	mm
<i>B</i> , mm	10	0.122	4507.8	2.748E-05	3.982	0.000
<i>W</i> , mm	10	0.221	6694.1	2.749E-05	3.984	0.002
<i>S</i> , mm	45	0.296	7478.4	2.752E-05	3.986	0.004
<i>a_{o-mes.}</i> , mm	3.982	0.368	7932.9	2.756E-05	3.991	0.009
<i>a_{f-mes.}</i> , mm	5.101	0.455	8286.3	2.763E-05	3.998	0.016
<i>a_{o-calc.}</i> , mm	5.363	0.548	8559.7	2.773E-05	4.007	0.025
<i>a_{f-calc.}</i> , mm	6.040	0.648	8773.3	2.785E-05	4.020	0.038
$\sigma_{0,2}$, MPa	654	0.747	8944.6	2.801E-05	4.035	0.053
σ_u , MPa	820	0.856	9057.4	2.821E-05	4.054	0.072
σ_{flow} , MPa	737	0.972	9124.3	2.845E-05	4.078	0.096
<i>E</i> , GPa	200.4	1.102	9156.8	2.877E-05	4.109	0.127
		1.219	9177.4	2.910E-05	4.139	0.157
		1.369	9081.3	2.957E-05	4.183	0.201
		1.521	8964.0	3.010E-05	4.232	0.250
		1.706	8775.1	3.084E-05	4.296	0.314
		1.895	8517.9	3.168E-05	4.369	0.387
		2.080	8288.4	3.260E-05	4.445	0.463
		2.288	8044.3	3.374E-05	4.536	0.554
		2.499	7807.6	3.501E-05	4.632	0.650
		2.713	7582.1	3.643E-05	4.735	0.753
		2.954	7288.3	3.816E-05	4.854	0.872
		3.219	6980.5	4.025E-05	4.988	1.006
		3.511	6655.7	4.276E-05	5.139	1.157
		3.816	6360.8	4.563E-05	5.297	1.315

Table 3.15. Continuation

a_i/w	A_{iel}	A_{ipl}	$f(a_i/W)$	K_i	J_{el}	J_{pl}	J_{total}
	N·mm	N·mm		MPa m ^{0.5}	N/mm	N/mm	N/mm
0.398	279	-2	1.972	40.0	7.1	-0.1	7.1
0.398	616	230	1.973	59.4	15.8	7.3	23.0
0.399	770	614	1.974	66.4	19.7	19.4	39.1
0.399	867	1078	1.977	70.6	22.2	34.0	56.2
0.400	949	1701	1.980	73.8	24.3	53.7	78.0
0.401	1016	2417	1.986	76.5	26.1	76.3	102.4
0.402	1072	3230	1.993	78.7	27.6	102.0	129.6
0.403	1120	4061	2.001	80.5	28.9	128.2	157.1
0.405	1157	5007	2.012	82.0	30.0	158.1	188.1
0.408	1184	6034	2.025	83.2	30.8	190.5	221.4
0.411	1206	7211	2.043	84.2	31.6	227.7	259.3
0.414	1225	8264	2.060	85.1	32.3	260.9	293.2
0.418	1219	9644	2.086	85.2	32.4	304.5	336.9
0.423	1209	11026	2.115	85.3	32.5	348.1	380.6
0.430	1187	12690	2.154	85.1	32.3	400.6	432.9
0.437	1149	14369	2.200	84.3	31.7	453.7	485.4
0.445	1120	15952	2.249	83.9	31.4	503.7	535.0
0.454	1092	17682	2.310	83.6	31.2	558.3	589.4
0.463	1067	19380	2.377	83.5	31.1	611.9	643.0
0.474	1047	21056	2.452	83.7	31.2	664.8	696.0
0.485	1014	22874	2.543	83.4	31.0	722.2	753.2
0.499	981	24803	2.653	83.3	31.0	783.1	814.0
0.514	947	26827	2.784	83.4	31.0	847.0	878.0
0.530	923	28843	2.933	83.9	31.4	910.6	942.1

4. NUMERICAL SIMULATION OF THE FRACTURE TOUGHNESS OF WELDED JOINTS – STATIC LOADING

In this chapter, the experimental analysis of welded joint constituents (fracture toughness) using notched specimens with notch positioned in PM and WM is numerically modeled [4.1-4.4] by using the finite element method (FEM). Text presented here is based on two papers, published in the scope of work on this thesis, [4.5 and 4.6].

In order to characterize the fracture of engineering components, it is important to provide acceptable estimations of the J fracture mechanics parameter. The use of weldments usually requires an over-matched condition as it is the case in present investigation, Chapter 3. The η factor is related to plastic components of strain energy [4.7]:

$$J_p = \frac{A_p \cdot \eta}{B \cdot (W-a)} \quad (4.1)$$

Where η is a function of the specimen geometry based on either LLD or CMOD measurement can provide accurate and effective toughness measurements for different fracture geometries [4.8 - 4.19].

Fracture mechanics toughness tests were done on PM and WM specimens, according to BS standards [4.20 and 4.21], as already presented in Chapter 3. Here, some more details are presented since they are relevant for the numerical simulation. The specimen design was of single edge notch bend SENB geometry. The crack plane orientation was normal to weld direction. In the case of WM specimen (WM 01), the notch location was in the WM center line. In the case of PM testing, PM 03 specimen was used, not presented in Chapter 3.

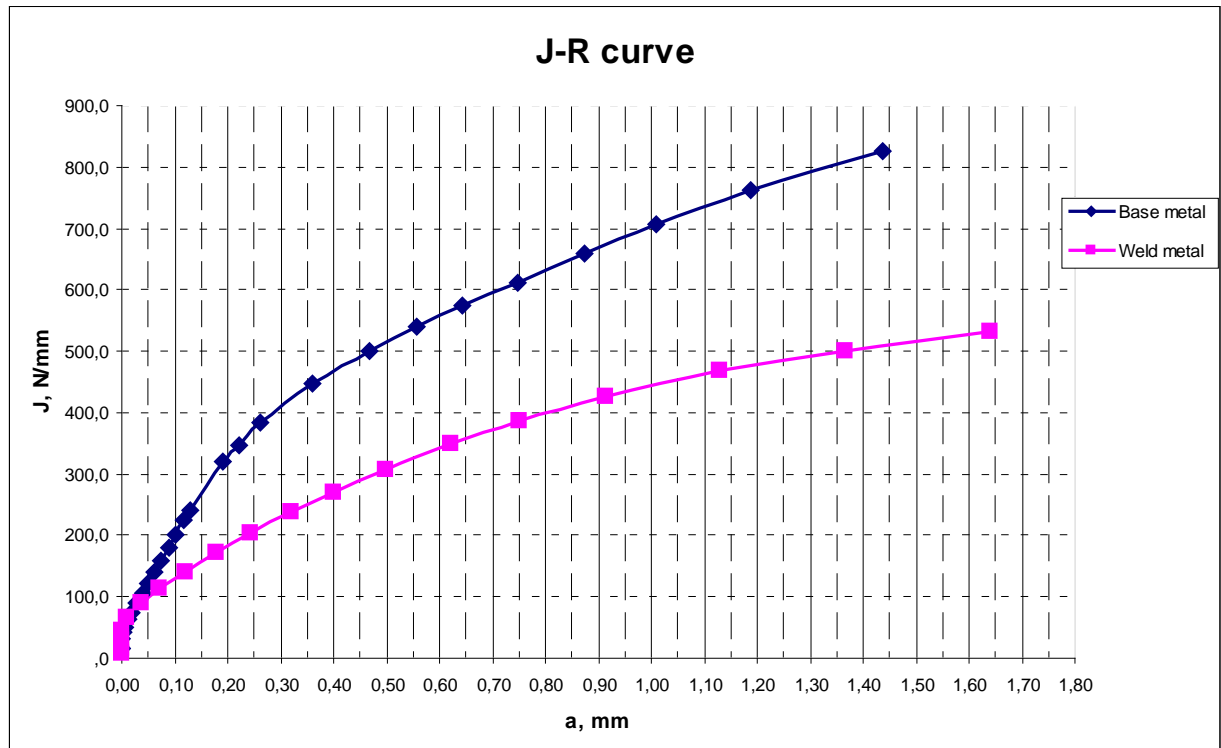


Figure 4.1. $J - \Delta a$ curve obtained by testing precracked SENB specimens with the notch positioned in PM and WM.

4.1. Finite Element Calculation of J -integral values

First step in FE model generation was to define two-dimensional geometry of specimen, Fig. 4.2, with the same dimensions as specimen used in experiment.

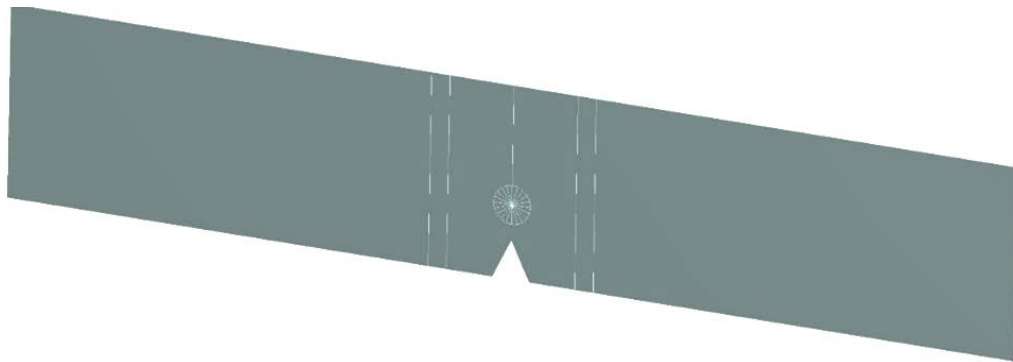


Figure 4.2 Geometry of specimen used in FE simulations

To ensure accuracy of numerical J -integral values, very fine mesh with special elements should be generated at the crack tip. Crack tip should contain 1 node in 2D numerical simulations and should be surrounded by elements of the same size, since the first contour for the area integration is positioned in these elements. Thus, 40 sector-like surfaces were created around the crack-tip node, Fig. 4.3, for the purpose of getting regular finite elements at that node.

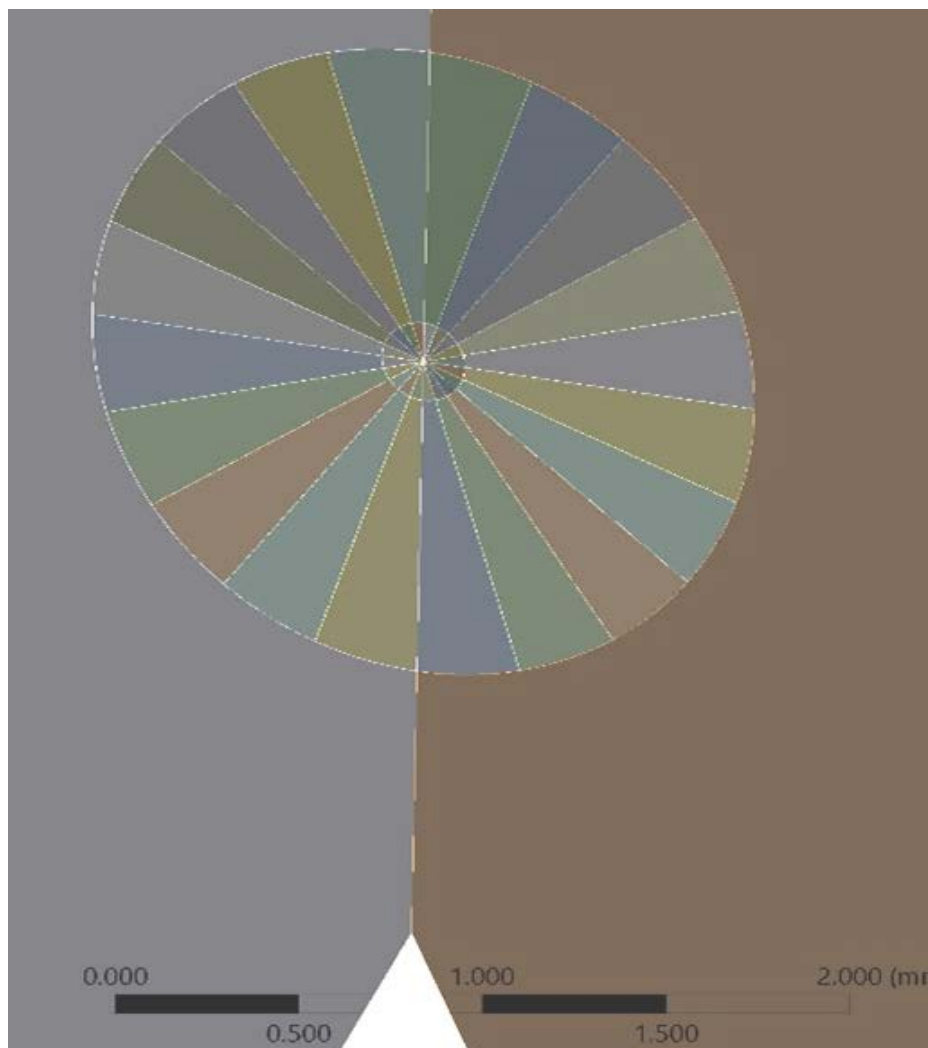


Figure 4.3 Geometry around the crack-tip node

4.1.1. Specimen made of WM

In total, 5 geometries similar to that shown in Fig. 4.2 are established to represent 5 crack tip positions during experiment. Distances between the crack-tip node and bottom edge were: $d_1 = 3.848$ mm, $d_2 = 4.026$ mm, $d_3 = 4.598$ mm, $d_4 = 4.978$ mm and $d_5 = 5.487$ mm. Corresponding force values were: $F_1 = 4347$ N, $F_2 = 9025$ N, $F_3 = 7794$ N, $F_4 = 6711$ N and $F_5 = 5408$ N, respectively. Using specimen geometries in the Ansys Workbench software, meshes were created with cca 14500 finite elements of PLANE183 type, as shown in Fig. 4.4, including the mesh around crack tip in the case of finite element model with $d_1 = 3.848$ mm. Thickness of all finite element models was $t = 10$ mm.

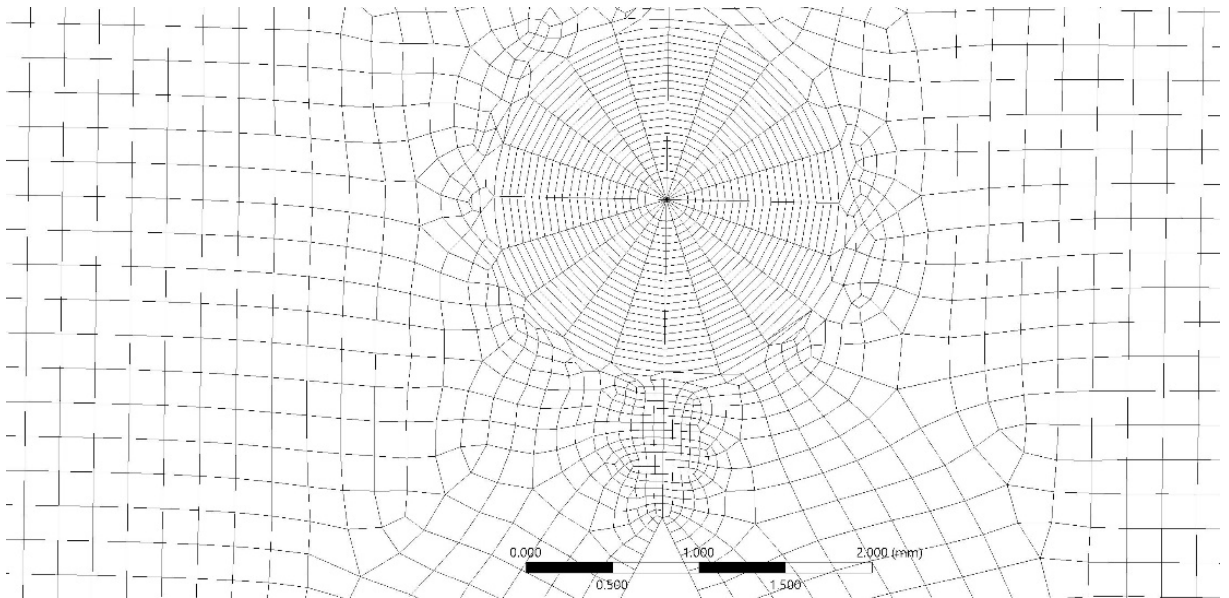


Figure 4.4 Finite element meshes with fine mesh around the crack tip

Crack growth is simulated in Ansys Workbench typically for the constant applied force; and thus multiple load steps are yet not supported by this software. Therefore, several finite element models, with different crack lengths, were created and used, with forces F_1 to F_5 applied at 13 nodes in positive x direction (downward, red dots marked by red arrow in Fig. 4.5) above the crack tip. Distance between 1st and 13th node was approximately equal to loading roller diameter. Boundary conditions were defined as for the 3 point bending case.

Typically, in finite element simulations, the contact between the roller and the specimen is defined at a single node. Anyhow, one should keep in mind that the contact between roller and specimen is actually of surface-to-surface type. Therefore, more than one node should be used to simulate experiment more realistically. Also, the surface area in the contact changes when crack grows; therefore, number of simulations should be performed to determine the number of nodes to be used, keeping the constant distance between two central nodes: $d = 45$ mm (experimental value). Here, it was found that 17 nodes perform the best, so displacements in both x and y direction were restricted for all nodes at the support on one side of the specimen, while displacement in y direction was not allowed for the nodes on the other support.

Properties of the WM, related to fracture mechanics, were determined in experiment, as already shown in Chapter 3, and used in Ansys Workbench, assuming the von Mises yield criterion with bilinear isotropic hardening, Fig. 4.6, with Young's modulus $E = 197000$ MPa, Poisson's ratio $\nu = 0.3$ and yield strength of 767 MPa.

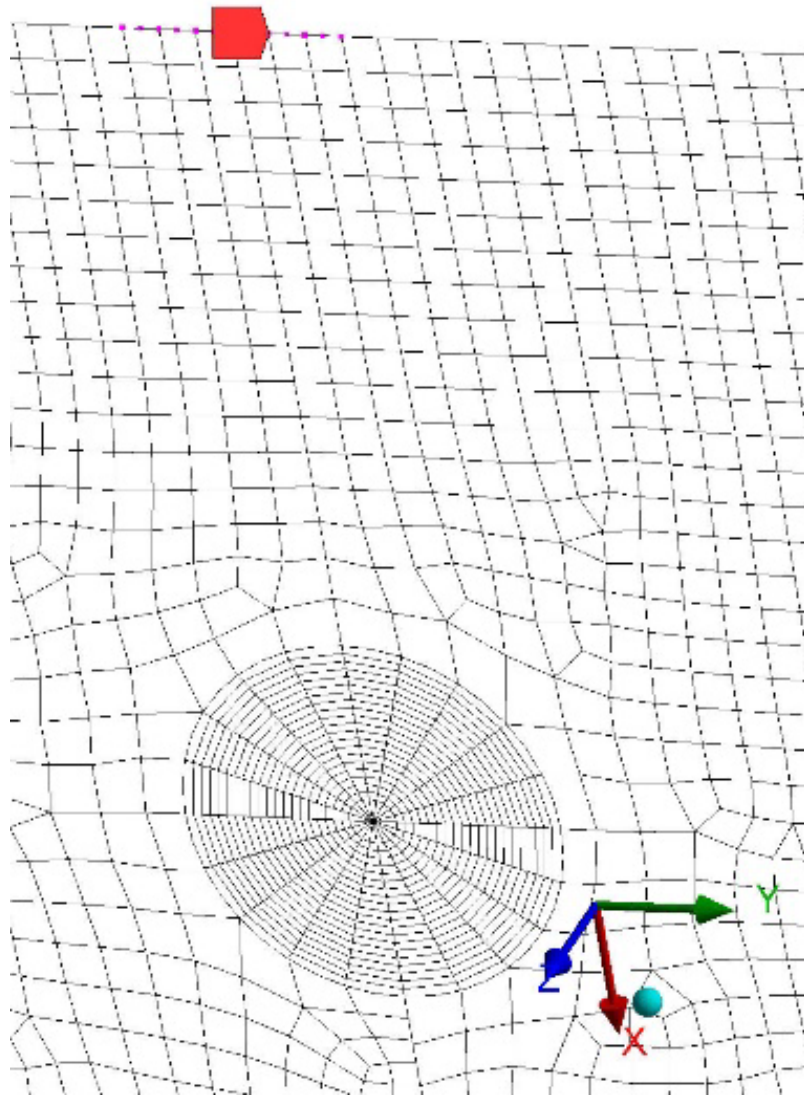


Fig. 4.5 Forces were applied directly above the crack tip (red tag) at exactly 13 nodes

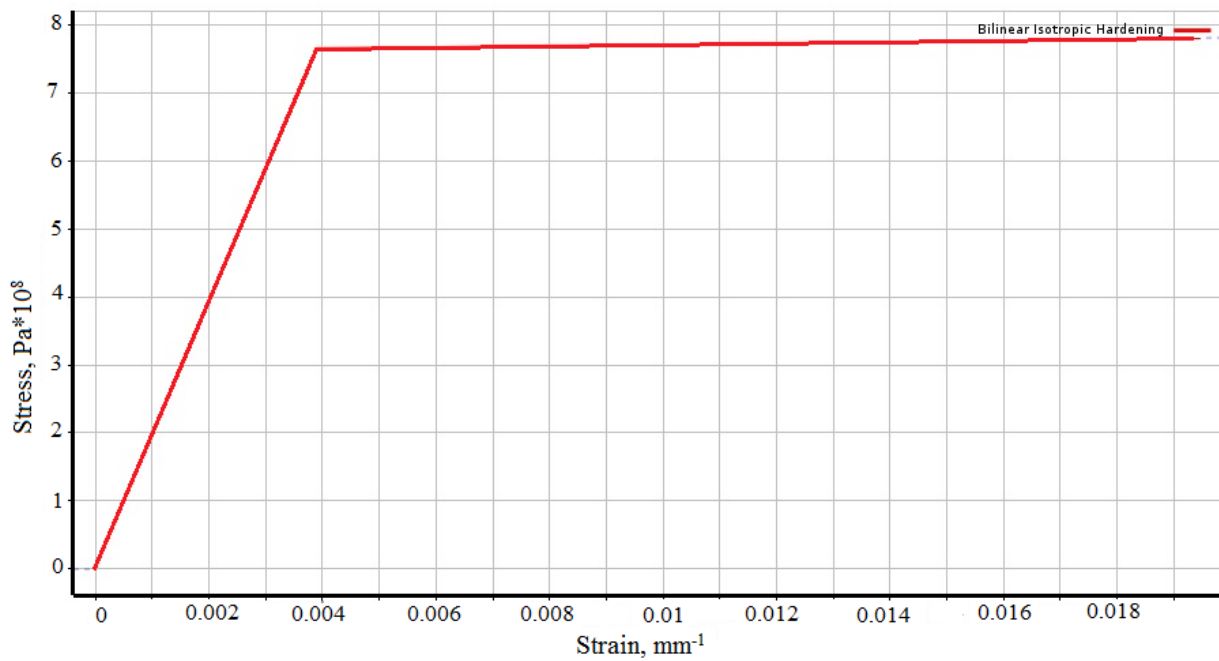


Fig. 4.6 Mathematical model used to describe plastic behavior of WM

4.1.2. Specimen made of PM

In the case of PM, specimens were also modeled with 5 different geometries to represent 5 crack tip positions during the experiment. In this case, distances between the crack-tip node and bottom edge were: $d_1=4.036$ mm, $d_2 = 4.256$ mm, $d_3 = 4.502$ mm, $d_4 = 5.046$ mm and $d_5 = 5.473$ mm, whereas the corresponding force values were: $F_1 = 4579$ N, $F_2 = 9357$ N, $F_3 = 9113$ N, $F_4 = 8019$ N and $F_5 = 6781$ N, respectively. PM properties used in this simulation were: Young's modulus $E = 183000$ MPa, Poisson's $\nu = 0.3$ and yield strength of 668 MPa. Tensile behavior of PM was modeled as shown in Fig. 4.7.

4.2. Results and discussion

Regarding properties of different zones in welded joint, it was shown in Chapter 3 that the base metal yield stress is 10% lower than for the WM, whereas its tensile strength is lower by cca 5%. It was also shown that the critical values of J -integral, J_{IC} for the WM is much lower than J_{IC} for the PM. A similar conclusion can be drawn from the J - R curve for the same samples, as shown in Fig. 4.1.

Keeping this in mind, results for numerical simulation of J -integral for the PM and WM are shown in Table 4.1, together with the experimental results.

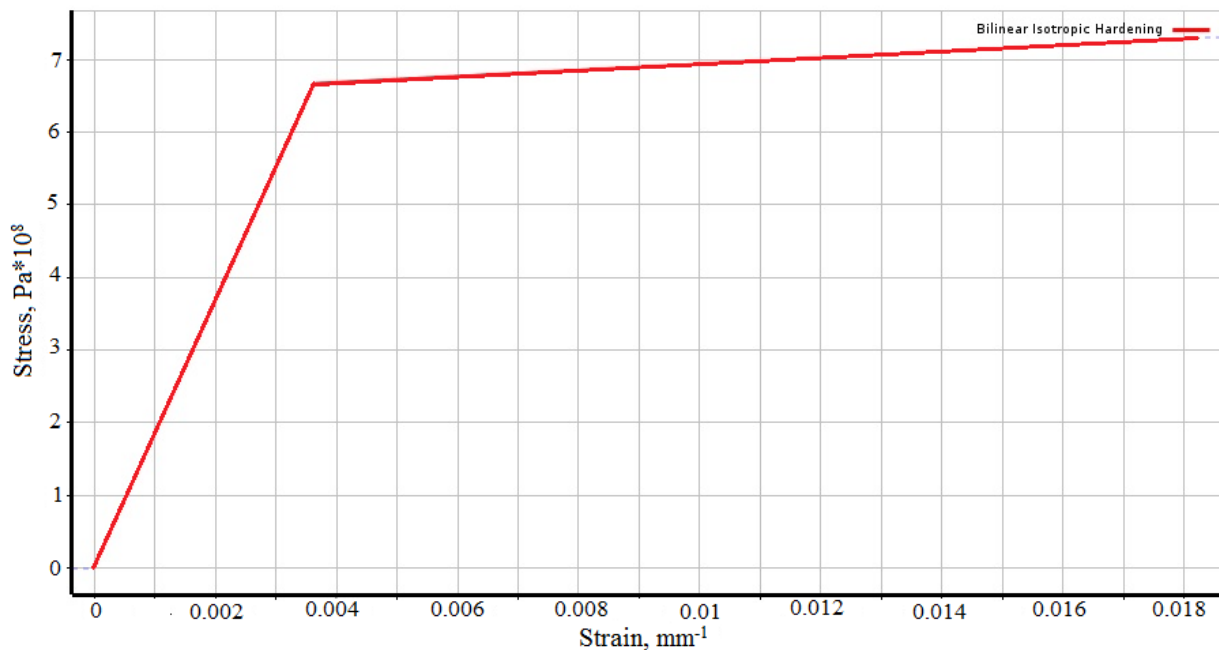


Fig. 4.7 Mathematical model used to describe plastic behavior of PM

Table 4.1. Comparison of experimentally and numerically obtained values of J -integral for characteristic crack lengths

PM			
Δa , mm	F , N	Experimental values of J -integral, N/mm	Numerical value of J -integral, N/mm
4.036	4579.1	14.70	10.842
4.256	9356.7	347.52	365.02
4.502	9113.0	499.01	516.05
5.046	8019.2	706.92	706.20
5.473	6781.2	824.92	804.22
WM			
Δa , mm	F , N	Experimental values of J -integral, N/mm	Numerical value of J -integral, N/mm
3.848	4347.2	6.91	6.807
4.026	9024.9	171.78	173.08
4.598	7793.6	387.26	396.54
4.978	6710.6	467.34	439.09
5.487	5407.7	531.68	499.12

One can see that the results for the WM indicate slightly higher deviations from experimental results compared to the results for the base metal, Tab. 4.1 and Fig. 4.8. In both cases the numerical values are slightly higher than the experimental ones are higher, up to 8%, Fig. 4.8.

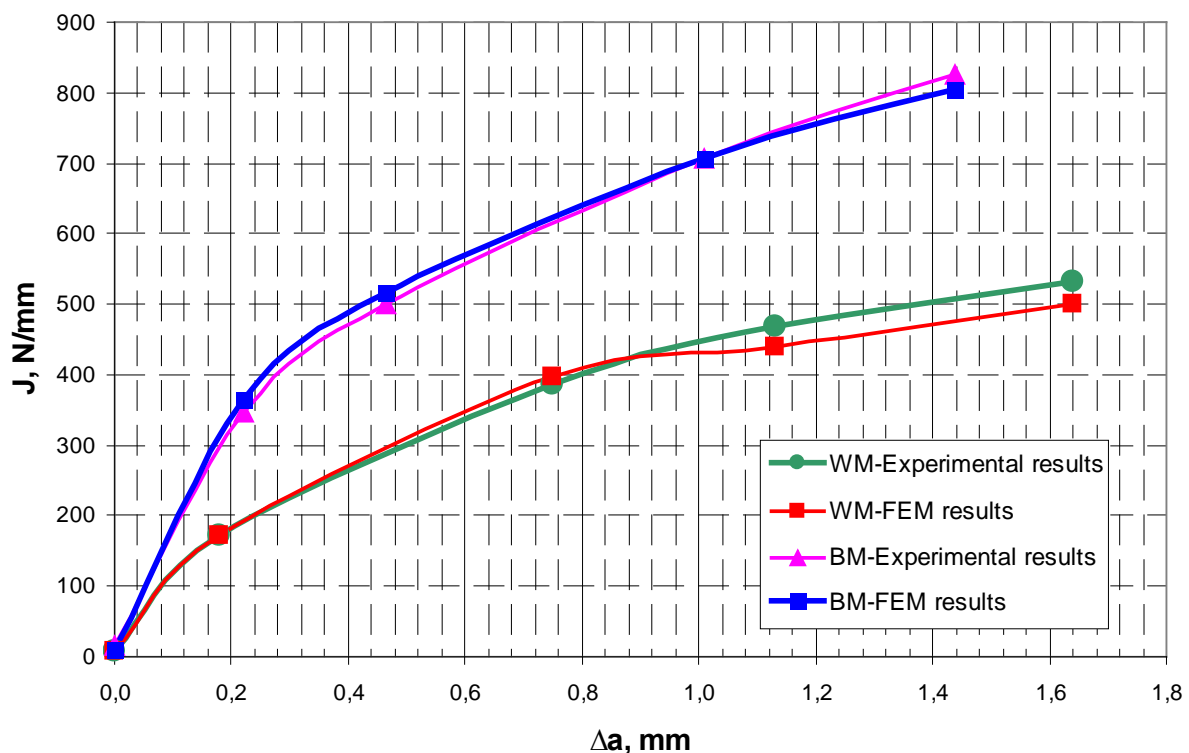


Figure 4.8. Comparison of experimentally and numerically obtained values of J -integral for PM and WM

5. FATIGUE CRACK GROWTH IN DIFFERENT WELDMENT ZONES

Different models to simulate dynamic crack propagation in welded materials can be found in literature [5.1-5.6]. Fatigue crack growth through different zones of a welded joint has been investigated, in terms of welded joint geometry and material properties, i.e. resistance to crack growth in different weldment zones. Toward this aim, two stages of numerical simulation of fatigue crack growth in a welded joint were performed using extended finite element method (XFEM), and verified with experimental results, presented in two papers, published in the scope of the work on this thesis [5.7 and 5.8]. In the first stage, numerical models in XFEM are based on Paris law in its simplest form, reducing the problem to determination of coefficients C and m , as explained in Chapter 2. In the case of a welded joint, i.e. heterogeneous material, it is of utmost importance to determine coefficients for each zone of a welded joint by applying the newly introduced procedure, as defined and explained in [1.1, 5.9 and 5.10]. In this investigation, welded joint was numerically modeled with different widths of the HAZ, using a number of models with wider and narrower HAZ.

In the second stage similar numerical models were used, with different material properties, to find out how fatigue crack growth resistance affects the number of cycles. Also, this analysis included the problem of crack growing from weld face side of the HAZ into the base metal, to find out how the total number of cycles changes in the case when the crack grows into the “more resistant” material, in terms of fatigue crack growth.

Heterogeneity of welded joints, i.e. several zones with different microstructures and mechanical properties, significantly affects fatigue crack growth rates, [5.9, and 5.10]. Results obtained by experiments on high strength low alloyed steel, presented in [5.7 and 5.8], are used here to develop numerical models, taking into account the heterogeneity of welded joints, i.e. three different zones, PM, WM and HAZ. To establish eventual effect of welded joint geometry on the fatigue life, additional numerical models are created, with the same dimensions, including total crack length, but with different mechanical and fatigue properties, corresponding to steel from a different weldability group. Yet another aspect of the problem of fatigue crack growth is the material itself, so the same procedure has been applied to another material with noticeably different properties, in this case the armour high strength steel Protac 500, having significant different fatigue crack growth properties, as explained in the Introduction and in [1.3 and 1.4].

One should keep in mind that both steels used in this analysis, although completely different in their applications, may be exposed to cyclic loading in exploitation, as in the case of the second material, Protac 500, which is used for armour vehicles, being subjected to cyclic loading, [5.11]. Therefore, fatigue crack growth is important phenomena for both steels and needs to be analyzed in details.

Keeping this in mind, numerical simulations were performed by XFEM, using ANSYS R19.2, to analyze fatigue crack growth in welded joints with different geometries and crack locations in different zones. Finite element method is now commonly used for a wide variety of problems, due to its accuracy, effectiveness and repeatability, whereas it's extended version, XFEM, is now widely accepted as the most efficient way to simulate fatigue crack growth, [5.9-5.13].

5.1. Materials and FEM input parameters

Properties of welded joints for both steels are obtained experimentally, the second one in the scope of investigations presented in [5.11]. Tensile properties are shown in Table 5.1, whereas Paris law coefficients, C and m , are shown in Table 5.2. Coefficients C and m have significantly different values in different zones of welded joint, making large difference in fatigue crack growth for each zone. One should notice that the fatigue crack was assumed to propagate through HAZ and PM in the case of armor steel Protac 500, as opposed to the 15NiMoCrB4-5 steel, where crack propagation was through WM and HAZ.

Table 5.1. Mechanical characteristics of welded joint regions, incl. both PMs [1, 5]

Zone	Yield stress, MPa	Tensile strength, MPa
HAZ (15NiMoCrB4-5)	568	829
WM (15NiMoCrB4-5)	460	690
HAZ (Protac 500)	810	1200
Parent material (Protac 500)	1210	1580

Table 5.2. Paris coefficients C and m for relevant welded joint regions

Zone	C	m
HAZ (15NiMoCrB4-5)	2.01E-11	3.4
WM (15NiMoCrB4-5)	2.87E-8	2.05
HAZ (Protac 500)	3.00E-13	5.68
Base material (Protac 500)	2.12E-10	4.0

5.2. Numerical simulation by the XFEM

Standard Charpy specimen, 10 x 10 x 55 mm, was used both for experiments and numerical simulations, with the total crack length of 5 mm. The notch was located in the root side of the HAZ. According to ANSYS requirements, at the notch tip the fatigue crack with an initial length of 0.2 mm was included in the model. Fatigue crack growth was simulated in two sets of models in the following way:

- The 15NiMoCrB4-5 steel set of models comprised two pairs, one for each welded joint zone (HAZ and WM) with according tensile properties and Paris coefficients C and m , since direct simulation of fatigue crack growth through different zones is still not possible in ANSYS, as explained in [5.12-5.14].
- In the first pair of the 15NiMoCrB4-5 steel models, the crack propagated through HAZ from initial 0.2 mm to the length of 1.9 mm, and in the case of WM model, it propagated from the length of 1.9 mm to the final length of 5 mm, so its length in the WM was 3.1 mm.
- In the second pair of the 15NiMoCrB4-5 steel models, fatigue crack length through HAZ was 2.45 mm, and in the case of WM model crack length was 2.5 mm.
- For the Protac 500 steel models, the first pair of models (“medium”) adopted the fatigue crack length in the HAZ as 2.4 mm, including 0.2 mm initial crack length, with remaining 2.6 mm of crack length in the PM.
- For the Protac 500 steel models, the second (“shorter”) and third (“longer”) pair of models, adopted crack lengths in HAZ 2.2 mm and 2.65 mm respectively, whereas PM models adopted

crack lengths 2.8 mm and 2.35 mm, respectively. In any case, the initial crack lengths in PM models were equal to the crack lengths at the end of the HAZ fatigue crack lengths.

As can be seen, in the first pair of the 15NiMoCrB4-5 steel model, the crack in the HAZ was shorter (1.9 mm) than in the example taken from [5.7], where the crack length was 2.2 mm. Therefore, the smaller HAZ and larger WM was assumed in this case. In the second pair of the 15NiMoCrB4-5 steel models, fatigue crack in HAZ was longer than the one take from the literature, so the HAZ was assumed to be larger, and thus the WM crack length was shorter, compared to its original length of 2.8 mm.

The finite element mesh used for all models is shown in Fig. 5.1, while the boundary conditions and loads are shown in Fig. 5.2, indicating one fixed end and free opposite end subjected to a bending moment, equivalent to the moment used in experiment. To simulate the real test conditions, value of the bending moment and the load gradually decreased, in order to account for the reduction of the load-bearing cross-section, due to fatigue crack growth.

Results for all models are shown in the form of diagrams, presenting relation between crack length and number of cycles. In the case of 15NiMoCrB4-5 HAZ model, the number of cycles obtained by XFEM is added to the number of cycles specimens experienced during experiment up to the crack length of 0.2 mm, to get the total number of cycles, meaning that 136,000 cycles are added to get more realistic result, i.e. to compensate for non-existing numerical fatigue crack growth from zero to 0.2 mm. On the other hand side, this was not made for WM model, since their initial crack length corresponded to the real crack length corresponding to the crack growth through the HAZ.

One should note that this was done also for the Protac 500 steel models, but somewhat differently. Namely, in this case from [5] it can be seen that the initial crack length was significantly greater than 0.2, so that the corresponding number of cycles to be added was just around 2,000.

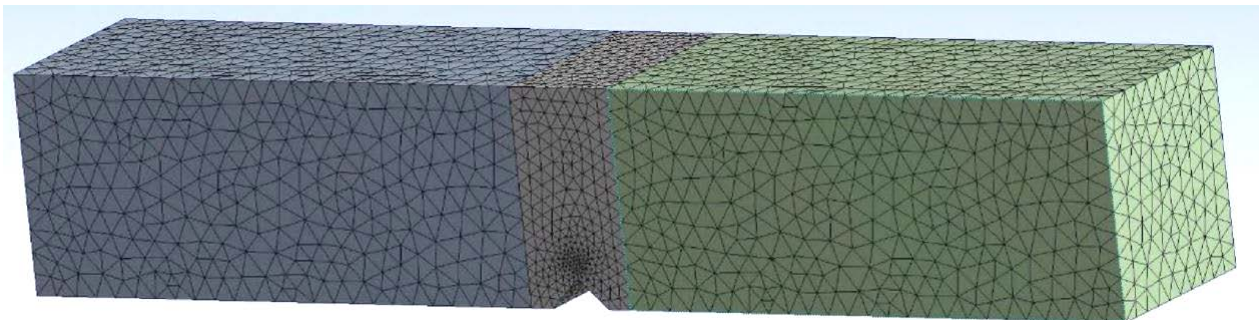


Figure 5.1. Specimen model geometry and the finite element mesh

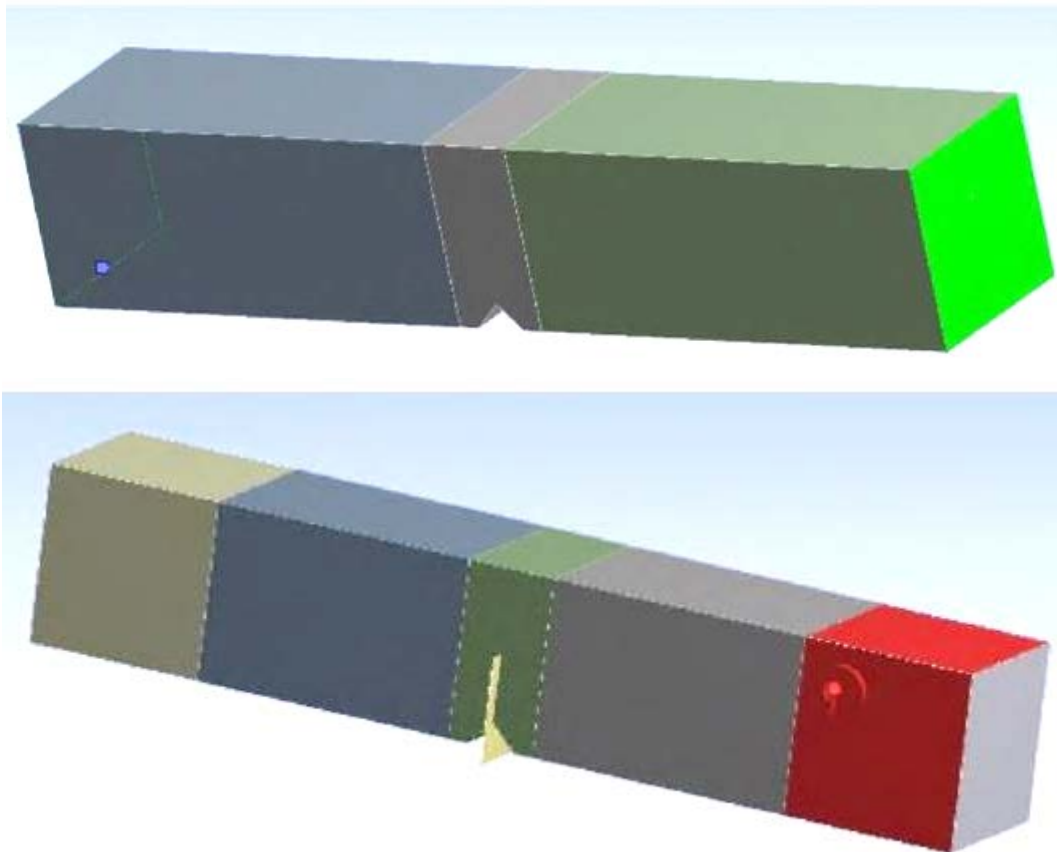


Figure 5.2. Boundary conditions – fixed support (top) and bending moment (bottom)

Numerically obtained $a-N$ curves for the first pair of 15NiMoCrB4-5 steel models with 1.9 mm long HAZ crack and 3.1 mm WM crack is shown in Fig. 5.3, while the corresponding $a-N$ curves for the second pair of P460NL1 steel models with 2.45 mm long HAZ crack and 3.1 mm long WM crack is shown in Fig. 5.4. Corresponding results for three pairs of the Protac 500 steel models, defined as “medium”, “shorter” and “longer” are shown in Figs. 5.5-5.7, respectively.

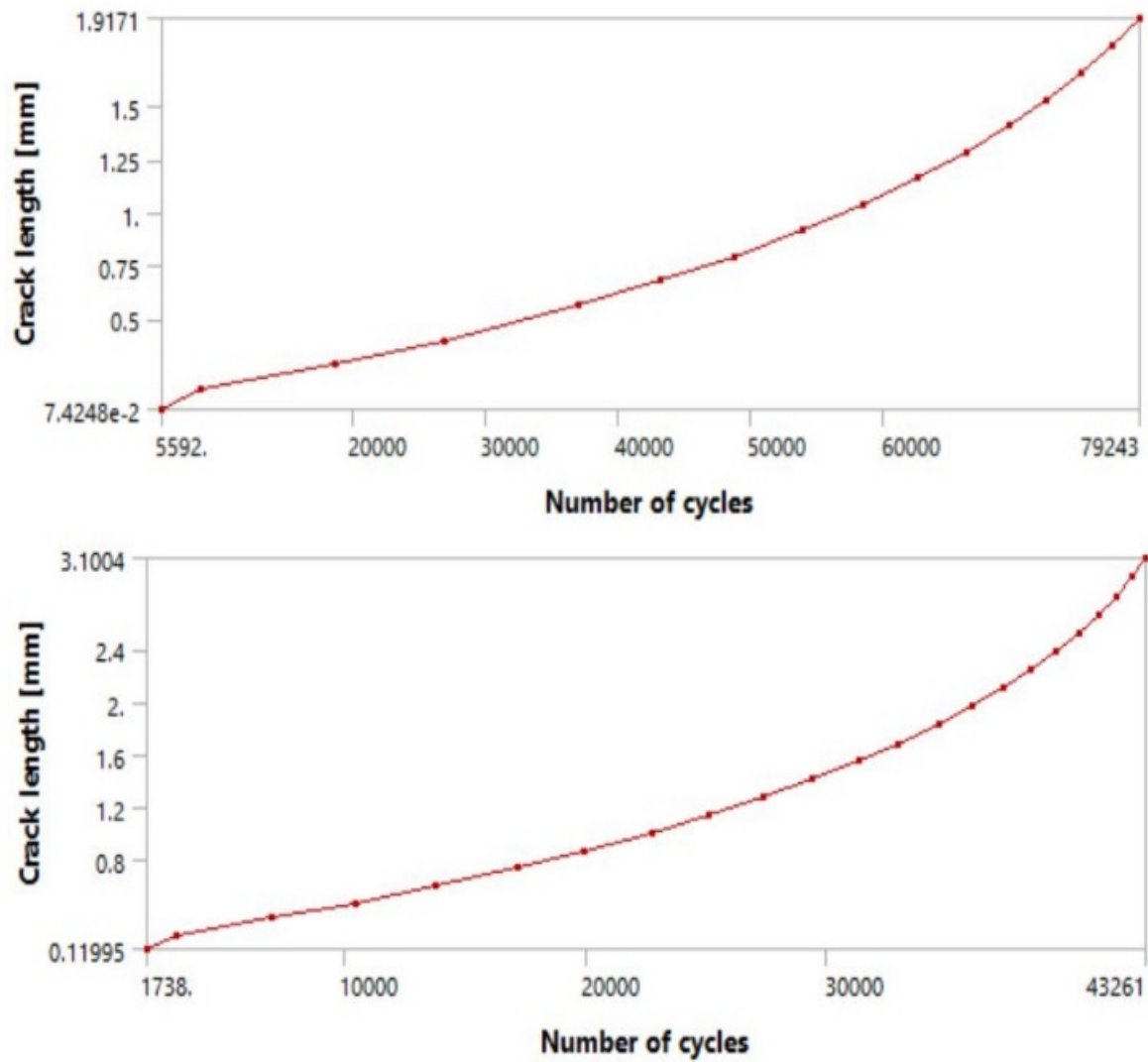


Figure 5.3. Numerically obtained $a-N$ curves the models with 1.9 mm HAZ crack (top) and 3.1 mm WM model (bottom) crack, the first pair of P460NL1 models

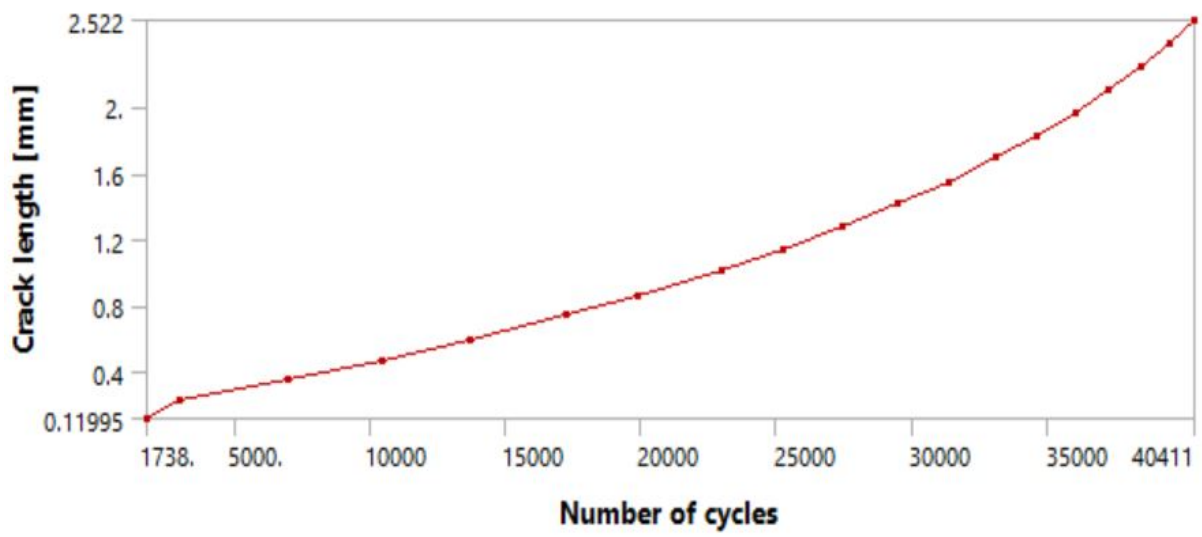
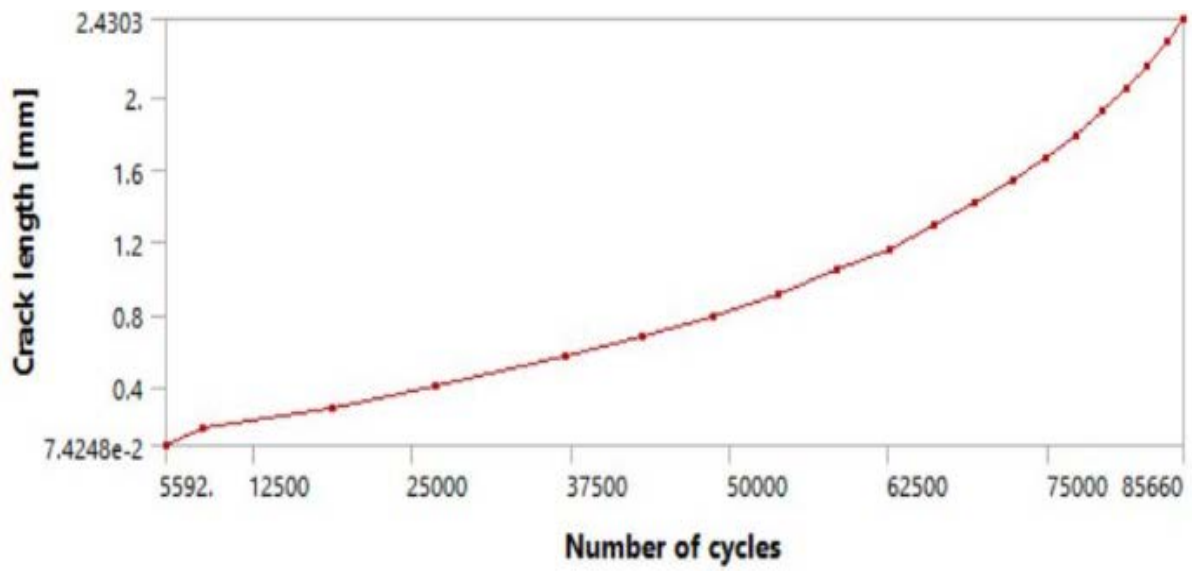


Figure 5.4. Numerically obtained $a-N$ curves the models with 2.45 mm HAZ crack (top) and 2.55 mm WM model (bottom) crack, the second pair of P460NL1

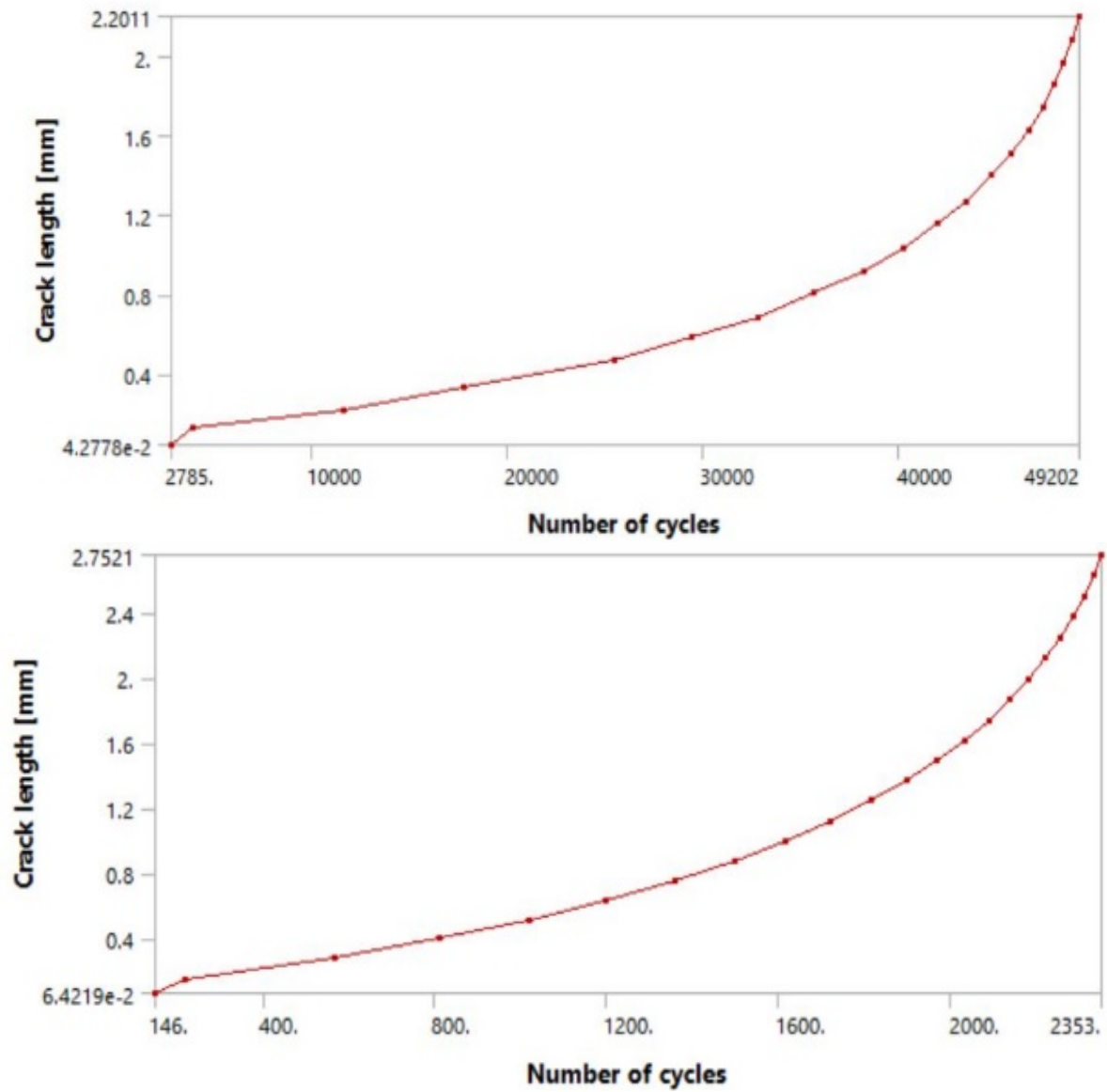


Figure 5.5. Numerically obtained $a-N$ curves for models with 2.2 mm HAZ crack (top) and 2.8 mm PM model (bottom) crack, the first pair of Protac 500 models

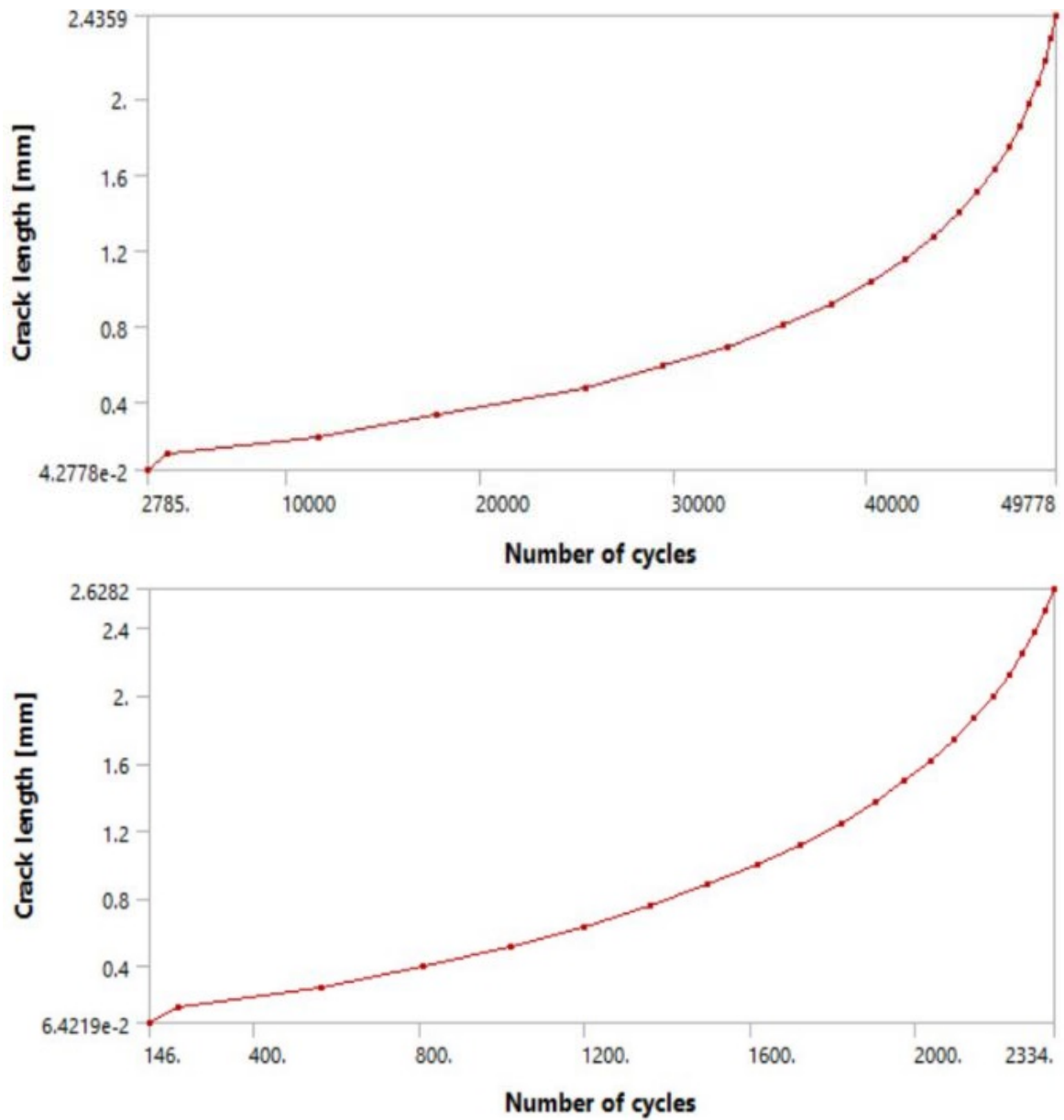


Figure 5.6. Numerically obtained $a-N$ curves the models with 2.4 mm HAZ crack (top) and 2.6 mm PM model (bottom) crack, the second pair Protac 500 models

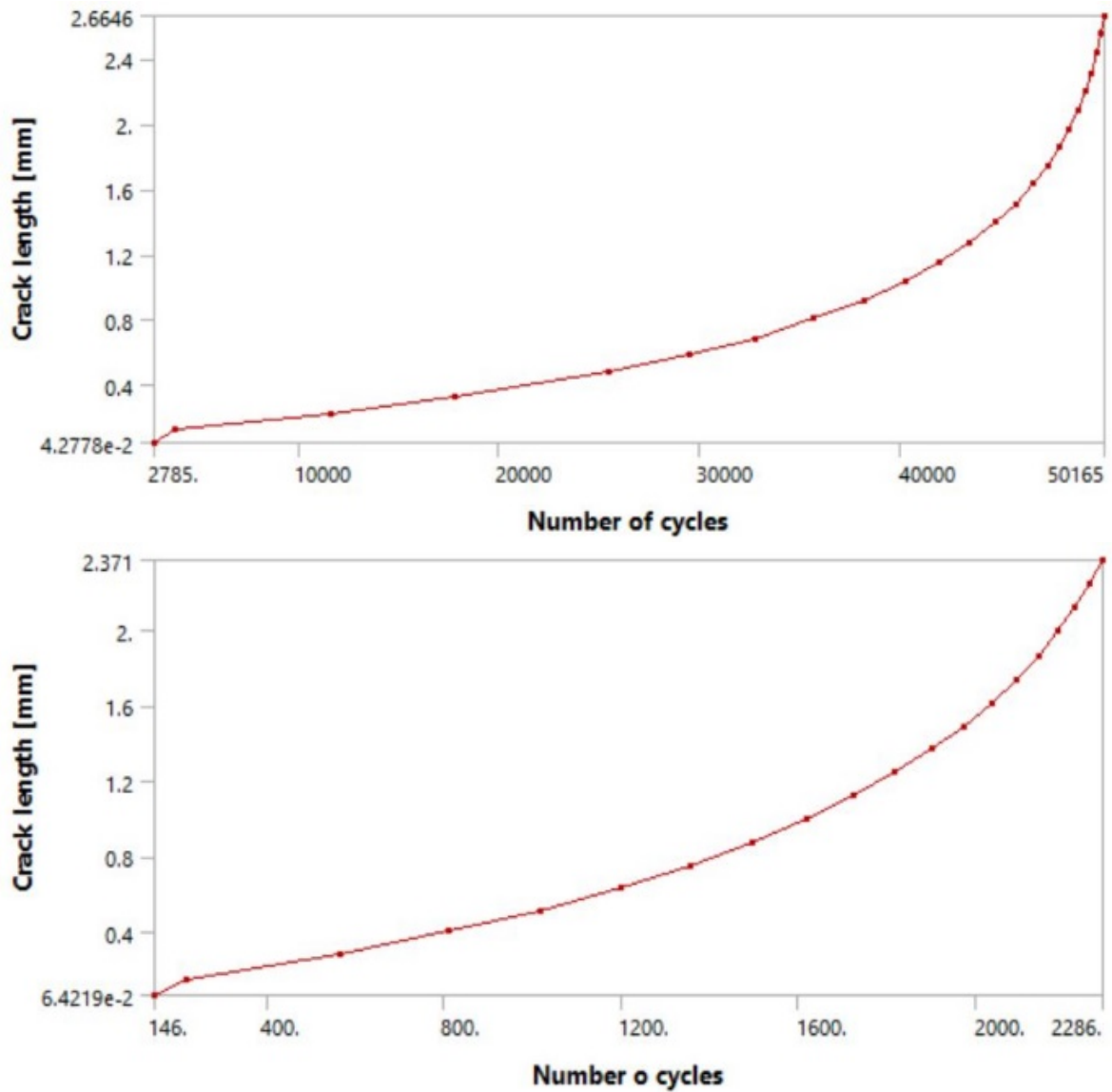


Fig. 5.7. Numerically obtained $a-N$ curves the models with 2.65 mm HAZ crack (top) and 2.35 mm PM model (bottom) crack, the third pair of Protac 500 models

Comparison of the total numbers of cycles for both pairs with the original values (2.2 mm HAZ + 2.8 mm WM) indicated, as expected, that models with increased crack length (3.1 mm in WM and 2.45 mm in HAZ) sustained larger number of cycles. On the other hand side, the other two models had slightly smaller number of cycles. The goal was to see how these changes affected the overall fatigue life, since it was reasonable to assume that the increase in the number of cycles in one region would compensate the decrease in the other, as shown in Table 5.3 in comparison with the referent model [5.7].

Table 5.3. Comparison of models with varied crack length and the original model [1]

Model	<i>N</i> , HAZ	<i>N</i> , WM	Total <i>N</i>
Referent - Specimen 5 [5.1]	218,800	42,000	260,800
First pair (1.9 mm HAZ + 3.1 mm WM)	214,500	43,200	257,700
Second pair (2.45 mm HAZ + 2.5 mm WM)	224,100	40,800	264,900

Results for the Protac500 steel pairs of models are shown in table 5.4. The numbers of cycles were significantly smaller than in the case of the 15 NiMoCrB4-5 steel. Also, one can notice that these values were practically not affected by different crack lengths.

Table 5.4. Comparison of models with varied crack length for the second set of models

Model	<i>N</i> , HAZ	<i>N</i> , PM	Total <i>N</i>
First pair (2.2 mm HAZ + 2.8 mm PM)	51,180	2,400	53,580
Second pair (2.4 mm HAZ + 2.6 mm PM)	51,160	2,310	53,470
Third pair (2.65 mm HAZ + 2.35 mm PM)	51,900	2,260	54,160

Since there were slight differences in the fatigue crack lengths in both sets of models (e.g. numerically obtained 2.43 mm vs. assumed 2.45 mm in the case of 15NiMoCrB4-5 steel), these values were extrapolated by multiplying the number of cycles with the ratio of the calculated and assumed crack length.

The results for the steel 15NiMoCrB4-5 provided the expected results, in terms of longer HAZ crack length resulting in somewhat higher resistance to fatigue crack growth. Anyhow, the HAZ size differences were small, so not a significant change in the number of cycles was obtained, around 1%. One should keep in mind that the specimen was 10 mm wide, with the fatigue crack length limited by the measuring foils (5 mm), leaving practically very little space for variation of the welded joint zone size. Anyhow, for thicker welded joints, larger differences in HAZ size can be expected, providing more noticeable differences in fatigue life.

For the Protac500 steel models, although with significantly smaller numbers of cycles, the differences were similar in relative measure (around 1.1% for the first two pairs and the third one. On the other hand, the models with “short” and “medium” HAZ crack lengths had shown practically the same result, contrary to the 15NiMoCrB4-5 steel models. Possible explanation is the initial crack length approximation.

When comparing two different steel, it is obvious that Protac 500, whose fatigue resistance originates from high crack initiation energy, as opposed to low propagation energy, is much more sensitive to crack growth, once the crack has initiated. One can say that significantly lower plasticity compared to 15NiMoCrB4-5 resulted in significantly smaller number of cycles.

Finally, one should notice that in the case of Protac500 steel, contrary to the expected behavior of the PM, the number of cycles was actually an order of magnitude lower for each PM model compared to the HAZ. This illustrates the significance of the microstructure of the welded joint regions – PM martensitic microstructure has significantly lower fatigue resistance compared to the HAZ mixed microstructure.

6. WELDED JOINT INTEGRITY ASSESSMENT BASED ON ANALYTICAL FRACTURE MECHANICS

This chapter of the thesis presents the analytical calculation of remaining life of a welded joint with a fatigue crack initiated in HAZ. The calculation is performed in two stages – the first one, when crack is growing through the HAZ, and the second one, when crack is growing through the PM. The analysis will be related to experiments previously performed with Protac 500 armour steel, as explained in the Introduction, with different fatigue properties, always with the assumption that the total crack length is 5 mm, due to measuring range of the used measuring foils, [5.7 and 5.8].

A well-known standardized experimental procedure for determination of Paris law constants can be replaced by numerical calculations in order to avoid cost-expensive experiments [6.1-6.5].

The analytical method to determine the number of cycles in a structure with a fatigue crack, based on Paris law, depends on several parameters, as explained later together with the background of these calculations, to better understand how the numerical simulation results are used in for the remaining life assessment.

Calculation presented in this Chapter was preceded by number of similar fatigue crack growth analyses, observing the crack growth in each individual welded joint zone [5.7-5.15], taking into account their different microstructures and consequent different properties and fracture behaviour. The aim is to apply the methodology introduced in [6.6], involving different steels used for fabrication of welded joints. The problems analyzed here comprise fatigue crack in the HAZ, [6.7] because:

- Previous work involved a micro-alloyed high strength steel, so the goal was to select a steel with significantly different microstructure, since it would have noticeably different mechanical and fatigue properties;
- Relevant experimental results for this steel were readily available [6.7], including mechanical properties and Paris equation coefficients C and m .

Since the fatigue crack in the analyzed problem grows through both the HAZ and the PM, these two zones are analyzed individually, taking into account their crack length. As already presented in the previous Chapter, there are three HAZ and PM combinations, with slightly increased HAZ/decreased PM crack length and vice versa, whereas the total cracks length was always 5 mm [5.7].

6.1. Analytical basis

Structural integrity assessment is based on fracture mechanics parameters evaluation, and correlation to their critical values. Knowing that a real structure may continue operating in presence of a crack, its integrity assessment is very important, since it helps making decision if a structure can continue working, or it needs to be repaired or even replaced. If fatigue is analyzed, the number of cycles is the representative parameter, being also evaluated by the numerical simulations.

To calculate the number of cycles under fatigue load, the following parameters have to be known:

- Paris coefficients C and m ,
- Static and dynamic stresses, including stress ratio,
- Initial and critical crack lengths,
- Crack geometry factor.

Paris coefficients are taken from the experimental data with the coefficient C given in units of MPa and millimetres, since crack lengths are typically given in millimetres, and stress in MPa. Thus, millimetres were used for both initial and critical crack lengths.

To determine the stresses, the mean values of bending moment are taken as the static stress. These bending moments corresponded to the initial load defined during the pure bending experiment (in this case 22240 N·mm) for HAZ, while in the case of PM, this value corresponded to different bending moment, depending on the initial crack length (2.2, 2.45 and 2.6 mm). Anyhow, these values varied only slightly, being around 15000 N·mm. Based on these values and the size of the specimen cross-section, also depending on the crack length, static stresses are evaluated and shown in table 6.1. It should be noted that all HAZ models have the same values, because the assumed initial fatigue crack length are equal, and so are their initial cross-sections and loads. On the other hand, different initial crack lengths of the PM models produces slightly different cross-section areas, and thus their static and dynamic stresses are also slightly different.

The stress ratio is used here to determine the amplitude stresses for each model, according to the following procedure:

- Static stress was calculated based on the bending moments from the experiment and the load-bearing cross-section of the specimen.
- For HAZ models, cross-section is the same, for PM models it depends on the initial crack length.
- The applied load for HAZ equals the bending moment from the experiment, while for the PM it corresponds to the relevant initial crack length (small, but not negligible difference).
- Taking into account the stress ratio, and the fact that the minimum stress equals static stress minus the amplitude stress, amplitude stresses can be calculated.
- In the case of a surface edge crack in a large plate, the geometry factor is typically adopted as 1.12, [6.8].

Table 6.1 Static and dynamic stresses used in number of cycle calculation for different HAZ and PM fatigue crack length combinations

Zone	Static stress, MPa	Dynamic stress, MPa
2.2 mm HAZ, 2.4 mm HAZ, 2.65 mm HAZ	160	130.9
2.8 mm PM	140	114.5
2.6 mm PM	134.5	110
2.35 mm PM	131.25	107.3

Taking into account the aforementioned values of static stresses, the dynamic stresses were determined based on the known stress ratio, and can also be seen in table 6.1. Initial crack lengths were adopted following the same logic as for the numerical models – 0.2 mm for the HAZ, and the final HAZ crack length as the initial for the PM model. Accordingly, critical crack lengths for the HAZ models were equal to the final length in that region, whereas the critical crack length for the PM models were always 5 mm, since that represented the actual total crack length.

Taking into account the first pair of models (2.2 mm in HAZ + 2.8 mm in PM), other models were made with a slightly larger HAZ, thus increasing the fatigue crack length and the number of cycles. Since the total crack length was constant, 5 mm, this also means that the crack length through the PM decreases, as well as the number of cycles. The formula that was used in order to determine the number of cycles, based on the above mentioned parameters, includes the Paris coefficients, C and m , stresses, initial and critical crack length and the geometry factor:

$$N = \frac{1}{\left(\frac{m-2}{2} \cdot C \cdot f^m \cdot \pi^{\frac{m}{2}} \cdot \Delta\sigma^m \right)} \left[\frac{1}{a_0^{\frac{m-2}{2}}} - \frac{1}{a_c^{\frac{m-2}{2}}} \right] \quad (6.1)$$

6.2. Results

Analytical calculation, explained in previous sub-chapter, is schematically showing in Fig. 6.1 using PM model with initial crack length of 2.2 mm as an example. In general case, this calculation takes into account the critical value of stress intensity factor, as one can see in the lower left corner of Fig. 6.1. However, in the case analyzed here, this is not needed, since the critical crack length is determined, as the unknown quantity, typical for the fracture mechanics analyses. In the analysis performed here, the critical crack length is taken as being equal to the maximum gauge length of the measuring foil (5 mm). Therefore, there was no need in this analysis to determine K_{Ic} . In reality, the critical crack length would have been larger, since no failures in the specimens occur with 5 mm length. This is due to the basic idea of this experiment, i.e. due to the fact that analysis focused on comparison of the fatigue crack growth rates through different welded joint regions, without the need for failure to occur.

Calculation in the remaining five models are performed in exactly the same way, only that different values of static/dynamic stresses and initial crack length were used for the PM models. For the HAZ models, only the critical crack length (corresponding to the initial crack length of the complementary PM model) was varied. Three different sets of Paris law coefficients were used for HAZ and PM models.

For the HAZ, the total number of cycles was around 120,000 for all three cases. More precisely, the numbers of cycles obtained for three models with different crack lengths are:

- 120,750 cycles for the 2.2 mm
- 120,970 cycles for the 2.4 mm
- 121,180 cycles for the 2.65 mm

As one can see, the number of cycles increases with increased HAZ crack length, which is expected due to its higher resistance to crack growth compared to the PM, but the differences are small, expressed only in hundreds of cycles, being just order of magnitude of 0.1%, making this effect negligible.

For the PM models, the number of cycles decreased, with the reduction in crack length, with values much smaller than in the case of the HAZ models. This was also expected, since the PM has significantly lower resistance to fatigue crack growth than the HAZ. Results for the individual specimens were as follows:

- 295 cycles for 2.2 mm crack growth.
- 250 cycles for 2.4 mm crack growth
- 205 cycles for 2.65 mm crack growth.
- Significant differences between the two groups of models are evident, even more than in the numerical ones. The numbers of cycles for the PM ranged from 205–295, significantly lower than for the first group of models (HAZ), which is expected due to its lower resistance to fatigue crack growth. Anyhow, the relative differences in the number of cycles were much greater in this case, reaching almost 20% (250 plus/minus 45).

Results are also shown in the form of diagrams for each HAZ and PM pair of models, in Figs 6.2–6.4. These diagrams were obtained by using the equation (6.1), to obtain better representation of

fatigue crack growth. They clearly illustrate significant difference in number of cycles for PM, and very small difference between HAZ models. All used Paris coefficients are shown in Table 6.2.

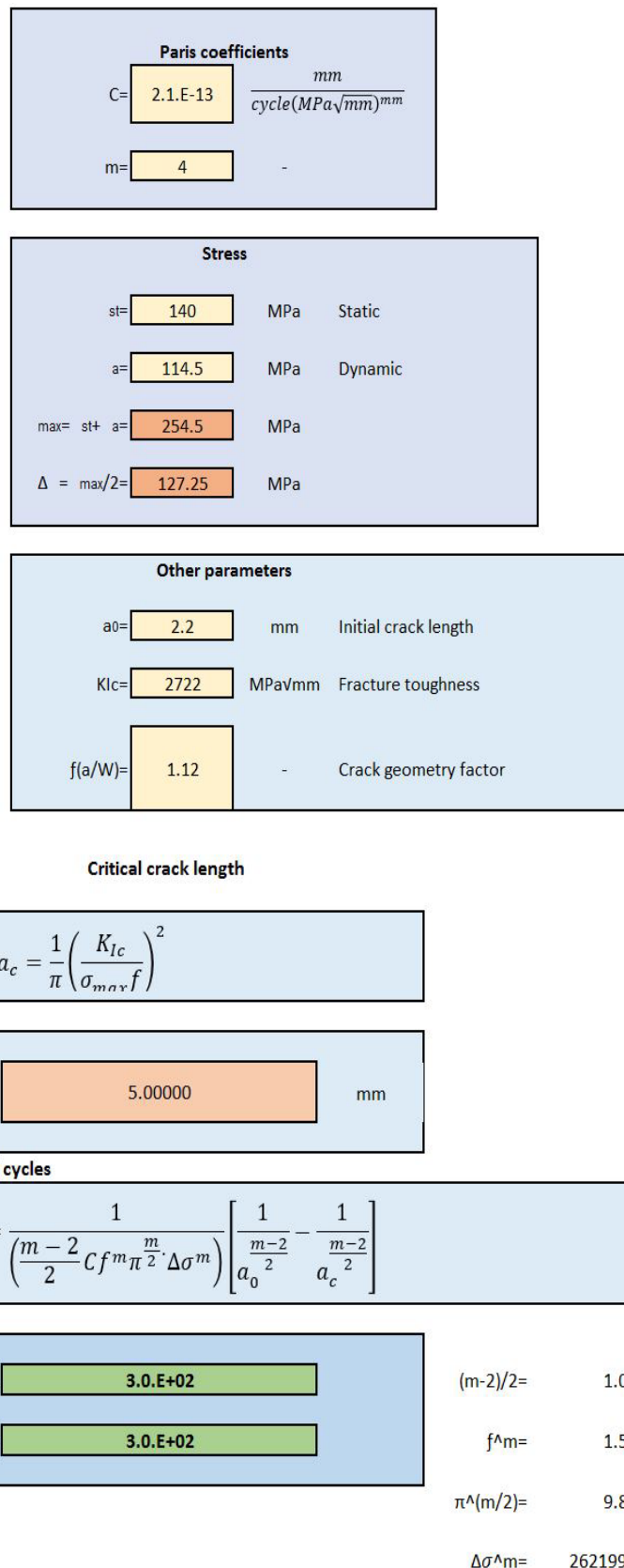


Figure 6.1. Example of the number of cycles determination based on fracture mechanics parameters, for model PM with initial crack length of 2.2 mm.

Table 6.2. Paris coefficients C and m for welded joint regions

Region	C	m
HAZ	2.01e-11	3.40
WM	2.87e-08	2.05

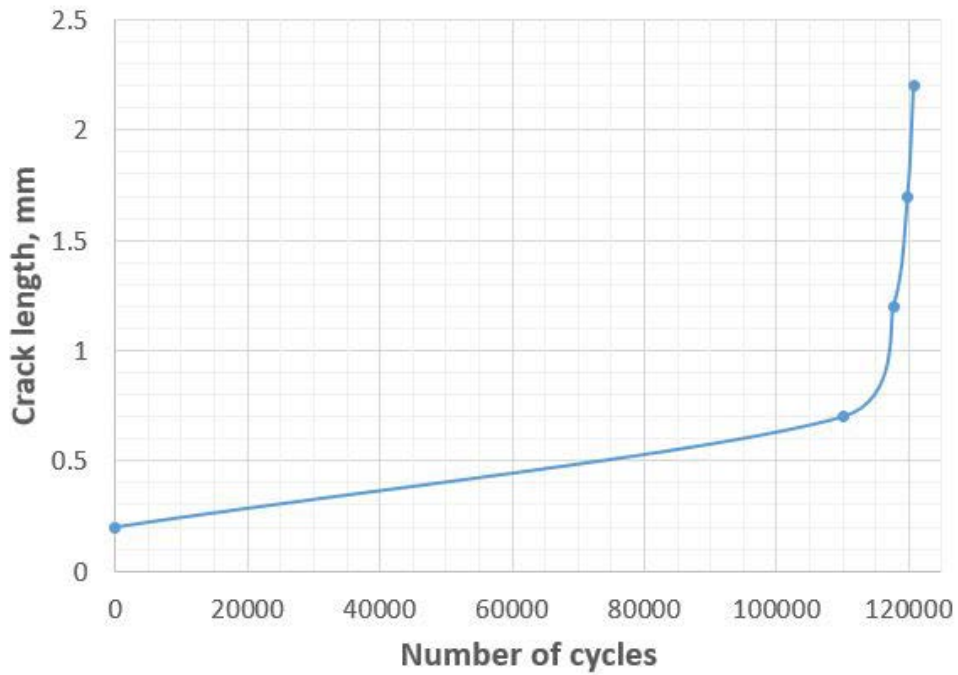
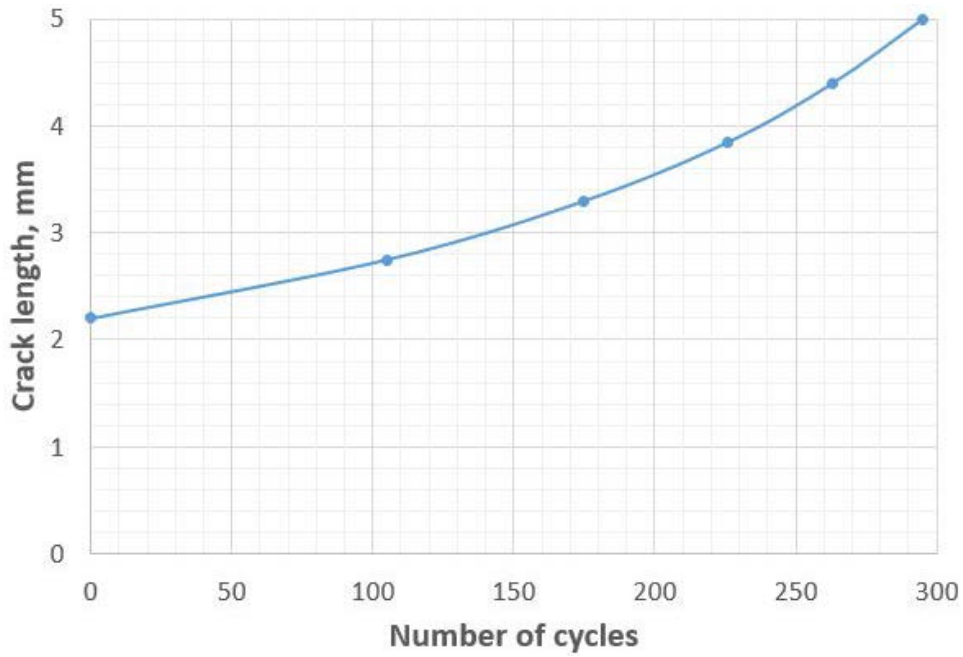


Figure 6.2 Crack lengths vs. number of cycles ($a-N$) diagrams for HAZ model with 2.2 mm critical crack length (above) and PM model with 2.8 mm critical crack length (below)

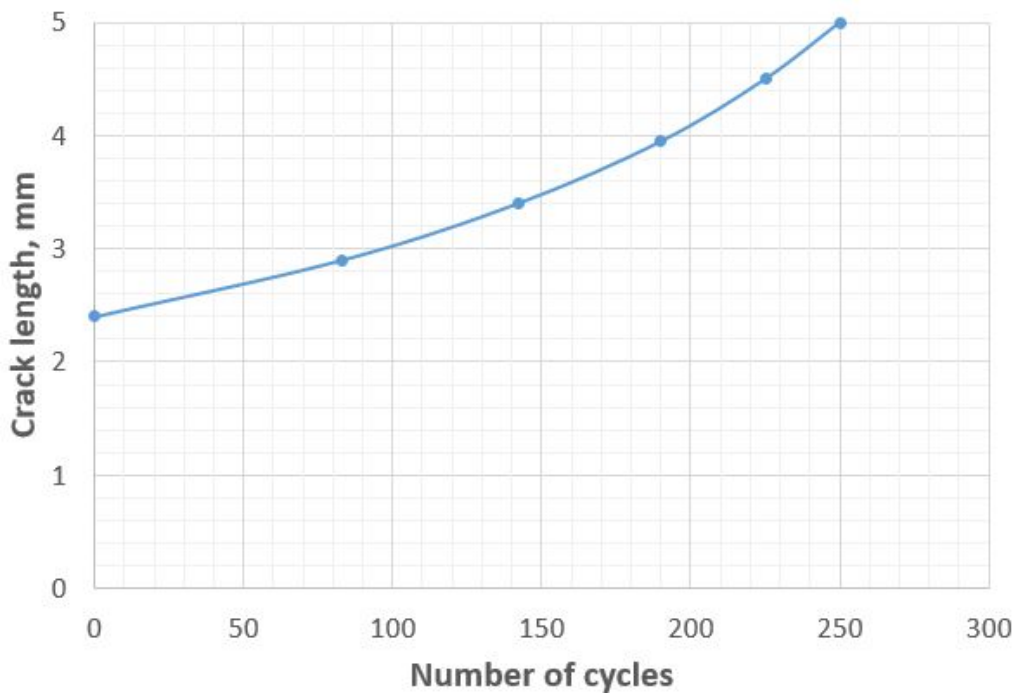
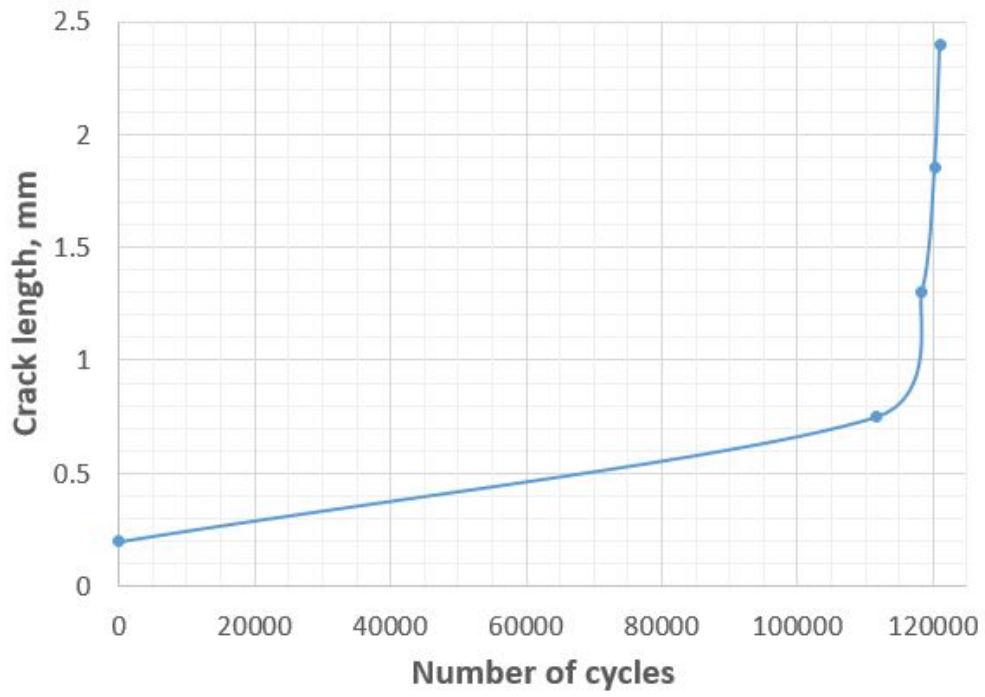


Figure 6.3 Crack lengths vs. number of cycles ($a-N$) diagrams for HAZ model with 2.4 mm critical crack length (above) and PM model with 2.6 mm critical crack length (below)

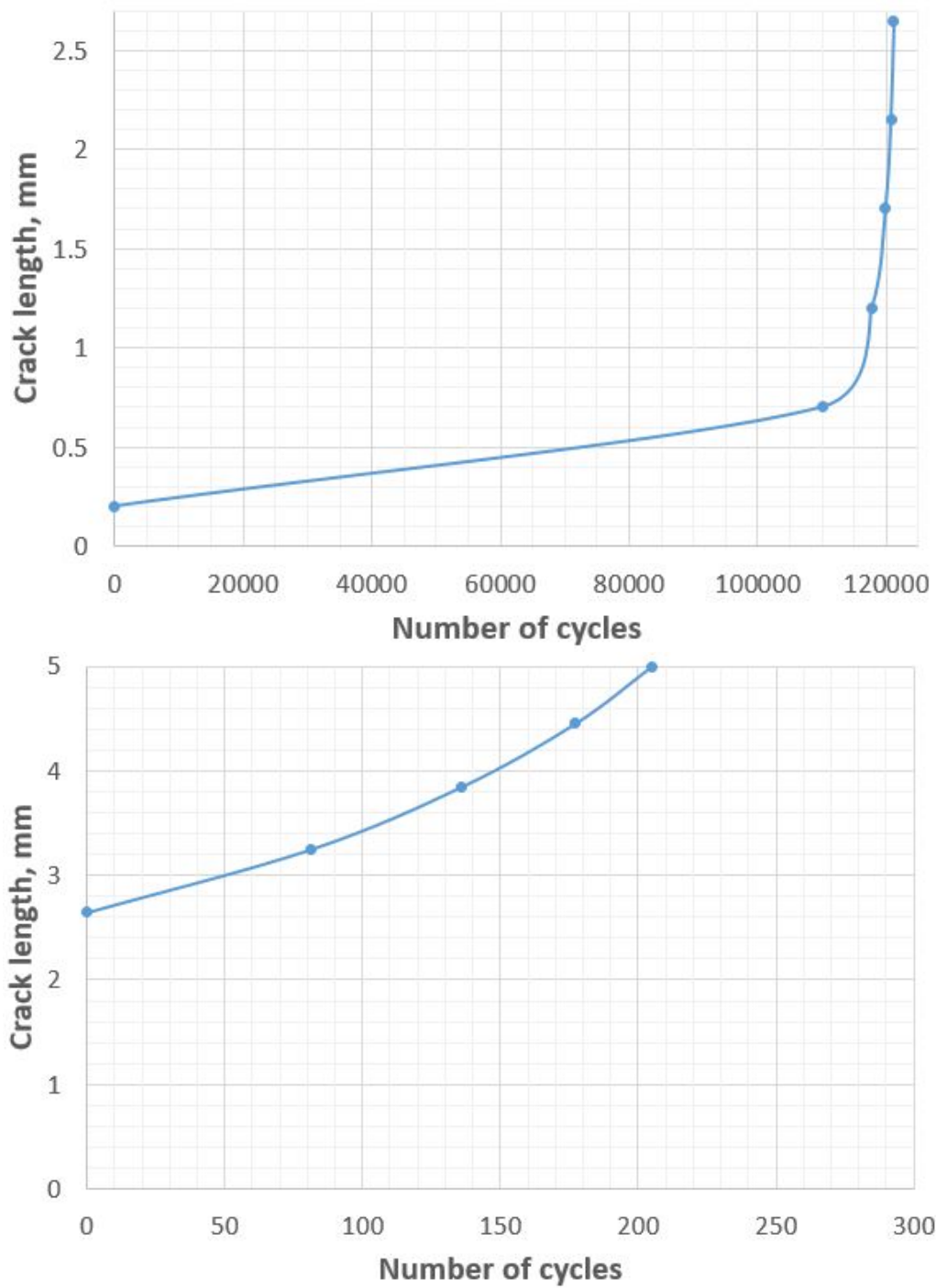


Figure 6.4 Crack lengths vs. number of cycles ($a-N$) diagrams for HAZ model with 2.65 mm critical crack length (above) and PM model with 2.35 mm critical crack length (below)

6.3. Comparison of analytical and numerical analysis

In this section of the paper, the comparison between the analytically and numerically obtained results will be presented. The overviews of these results are shown in Tables 6.3 and 6.4, for analytical and numerical results, respectively.

Table 6.3 Analytical number of cycles

HAZ fatigue crack, mm	Number of cycles	PM fatigue crack, mm	Number of cycles
2.2	120,750	2.8	264
2.4	120,970	2.6	228
2.65	121,180	2.35	187

Table 6.4. Numerical number of cycles

HAZ fatigue crack, mm	Number of cycles	PM fatigue crack, mm	Number of cycles
2.2	51,160	2.8	2,400
2.4	51,180	2.6	2,310
2.65	51,900	2.35	2,260

To compare numerical and analytical results, the $a-N$ diagrams obtained by the numerical simulation should be used, as shown in figures 5.5-5.7. Certain differences can be observed in the maximum values for crack length and number of cycles in the diagrams, when compared to the values shown in table 6.4. The reason for these differences is due to the fact that the numerical crack length could not be limited to precisely 2.2 mm, 2.4 mm, etc. This was also the reason for the 2.35 + 2.65 mm combination – crack length cannot be exactly predefined, so it is evaluated by the number of sub-steps in the fatigue analysis. Thus, the number of cycles corresponding to these approximate values is determined by interpolation. Since the differences between exact and approximate crack lengths are very small, the $a-N$ curve in this region can be taken as being linear. Therefore, determining the ratio between these two lengths and multiplying the number of cycles is sufficiently accurate for the purpose of evaluating the exact number of cycles.

Results for all three HAZ models indicate negligible differences, as the models differed by only cca 200 cycles, i.e. in relative terms, only by 0.18% between HAZ 2.2 and HAZ 2.4 mm models, and 0.17% between HAZ 2.4 and HAZ 2.65 mm models. Contrary to that, for the PM models, the differences were considerably higher, in relative terms. More concretely, the first two models, PM 2.8 mm and PM 2.6 mm (corresponding to the HAZ 2.2 and HAZ 2.4 mm models, respectively) indicate difference of 13.6% (which is almost 100 times greater than their HAZ counterparts). The difference between the second two (PM 2.6 mm and PM 2.35 mm) was even larger, around 18%. This was in accordance with previously stated facts about the fatigue crack growth resistance of both welded joint regions and the initial conditions.

If considered for the total crack length (5 mm), differences are also negligible, since the numbers of cycles in PM are almost 600 times smaller, and their high relative differences are very small on the global scale. The same holds for differences in HAZ, being very small all along, so that their sums barely changed, although they still marginally increased with the increase of crack length in more resistant region, HAZ.

Regarding the numerical results, some interesting observations can be made. The numbers of in this case were also much larger for the HAZ, even above 50000 for the HAZ models, compared to the PM models, with only around 2300 cycles. Significantly higher resistance to fatigue crack growth in this case can be explained by considering the input fatigue parameters, i.e. Paris coefficients, which are the same. Based on this, it can be seen that, for the HAZ models, the analytical calculations provided numbers of cycles more than twice greater than the numerical models, and that the differences between individual HAZ numerical models were also quite small, around 1% or even less.

For the PM models results are reversed – the numerical results indicate numbers 8-10 times larger number of cycles compared to the analytical ones. Regarding different crack lengths and differences between analytical/numerical models, the percentage increase and /or decrease in the number of cycles is significantly higher in the case of analytical results than for the numerical results. In the latter case, differences ranged from 2.2-3.75%, being around 5-6 times less than the differences in the case of analytical results.

As was determined, differences between the two welded joint regions (the HAZ and the PM) are far more prominent in the case of analytical calculation, with HAZ models having ~600 times greater cycle numbers, as opposed to the numerical ones, where these numbers are still significant, but much less pronounced ~25 times larger. The behavior of the HAZ and the PM in terms of resistance to fatigue crack growth remained the same in both cases – the HAZ performed in accordance with the expectations based on experimental work – showing much longer fatigue life for both analytical and numerical analyses.

As for the total number of cycles for each pair of HAZ and PM models, adopted in the same way for the both cases (i.e. 2.2 + 2.8 mm, 2.4 + 2.6 mm and 2.65 + 2.35 mm), the differences between numerical and analytical results are very small.

6.4. Discussion

In this part of the chapter, the comparison between the previously presented results will be given in more detail, along with the comparison showing the similarities and differences between this, analytical approach and the numerical simulation. Based on the results for all three HAZ models, it was clear that the differences were negligible, being around 0.18% between HAZ 2.2 and HAZ 2.4 mm models, and 0.17% between HAZ 2.4 and HAZ 2.65 mm models. As for the PM models, the differences were considerably higher. More accurately, the first two models, PM 2.8 mm and PM 2.6 mm (corresponding to the HAZ 2.2 and HAZ 2.4 mm models, respectively) had shown a difference of 15.3% (almost 100 times greater than their HAZ counterparts), and the difference between PM 2.6 mm and PM 2.35 mm models was even greater and equal to 18%.

Lower absolute differences in the second set of models can be simply explained by the much higher fatigue crack growth rate in the PM, resulting in much smaller numbers of cycles, over similar changes in distance (crack length). Higher relative differences are also the result of this, but it also needs to be mentioned that there is another initially significant difference between the HAZ and PM models – namely the initial crack length. The fact that the weaker material had a longer initial fatigue crack for each calculation further contributed to the considerable difference in the number of cycles for the HAZ models (with a 10^5 order of magnitude) and the PM models (wherein they were expressed in 10^2). This resulted in a considerable increase in the difference, which was already expected to be of significant order of magnitude, based on the experimentally determined values of the Paris coefficients for the HAZ and the PM.

As for the numerical results, presented in the previous chapter, some interesting observations can be made. The numbers of cycles in this case were around 50 000 for the HAZ models, and around 2 300 for the PM ones. This suggests that, in the case of the HAZ models, the analytical calculations provided numbers of cycles more than twice greater than the numerical models, but still with very small differences, well below 1% (which in turn, were the differences in the case of the other material P460NL1, also related to the numerical results).

For the PM models, however, the situation was the exact opposite – the numerically obtained numbers of cycles were between 8 to 10 times greater than the analytically obtained ones. On the other hand, the percentage increase/decrease in the number of cycles has a noticeably higher percentage in the case of analytical results, despite obviously lower values. Thus, the difference between the two welded joint regions (different materials, in terms of microstructure) was far more prominent in the case of analytical calculation, with HAZ models having ~500 times greater cycle numbers, as opposed to the numerical ones, where these numbers were „only“ ~25 times greater.

In terms of the total number of cycles for each pair of HAZ and PM models (i.e. 2.2 + 2.8 mm, 2.4 + 2.6 mm and 2.65 + 2.35 mm combinations, as was the case in the numerical models), the differences were very small. This was quite similar to the numerical results, wherein total numbers of cycles also varied by a small amount. In both cases, increased fatigue crack length through the stronger of the two zones (HAZ for this material) resulted in a small increase in the number of cycles, in accordance with expectations.

What was not expected, however was the difference in the behavior of „numerical“ and „analytical“ fatigue cracks in the PM, compared to their HAZ counterparts. This suggests that additional analyses should be undertaken as future research, to try and determine why such different behavior was obtained for different welded joint regions. This also suggests the need to thoroughly reconsider the adopted approximation, so that these models could be further improved at some point.

7. CONCLUSIONS

Having in mind the utmost requirement for welded structures, i.e. reliability and safety of welded joints, even in the presence of cracks, it is the major task to assure its structural integrity. Toward this aim, fracture mechanics analysis is inevitable tool, proving all necessary data to fulfil this task, and guarantee reliability and working ability of the welded structure.

Basic goals of this research were to determine fracture mechanics and fatigue properties of steel 15NiMoCrB4-5 and its welded joint (Chapter 3), to simulate numerically experimental J - R curve (Chapter 4), to establish effects of welded joint geometry (different zone sizes) and crack location on fatigue life of two different materials (Chapter 5) and to compare analytical and numerical results for the fatigue crack growth. Based on the fracture mechanics testing one can conclude (Chapter 3):

- Steel 15NiMoCrB4-5 and its welded joints have reasonable resistance to crack growth, both statically and dynamically.
- The static resistance is the highest in the parent material, than in the heat-affected zone, and the lowest in the weld metal.

Based on the results of numerical simulation of the J - R curve (Chapter 4), one can conclude that newly introduced procedure provided very good agreement with the experimental data both for the parent material and for the weld metal.

Based on the results of numerical simulation of the fatigue crack growth (Chapter 5) the following can be concluded:

- A small difference in the number of cycles in both zones was observed in the first case, leading to a total number of cycles (combination of number of cycles for each heat-affected zone and weld metal model) slightly different from the original value (for the model based on pure bending experiment). Increased crack length in the heat-affected zone provided larger number of cycles, due to the fact that heat-affected zone has higher fatigue resistance.
- Since the second set involved steel with lower fatigue resistance, the number of cycles was lower, and so were the differences between them. However, when viewed in terms of percentage, difference was very small, cca 1%. In this case, longer heat-affected zone cracks were also the better option, with slightly longer fatigue life.
- The main advantage of the numerical simulation shown in this paper is the possibility of simple adjusting of the welded joint geometry, and providing as many different calculations as needed in short time, without the need to make any significant adjustments to the initial model. Since all of the models are based on the experimentally verified one, there is no need to perform additional experiments, which would be rather complicated.
- This method can be applied to different welded joint thickness values, as well as to different groove shapes (V, X, K grooves...), since their geometry also affects the fatigue crack length in the case where the crack propagates through different regions. While the results shown here have suggested that favorable location of a fatigue crack is in the heat-affected zone, regardless if in the weld face or root, there is a number of other possibilities to be taken into account. Different combinations of welded joint regions and material properties could provide entirely different results, depending on the type of steel in question. The methodology presented here offers a simple and effective way to consider all of the factors, so long as there is a solid base of experimental results to rely on.

Comparison between numerical and analytical calculations of fatigue life of welded joints, with special focus on crack growth through different regions has been presented in Chapter 6. Different crack

lengths in the heat-affected zone and parent metal were adopted to analyse differences in consequent number of cycles. Main conclusions are the following:

- Total number of cycles (for combined zones) was not affected by fatigue crack length change for cca 0.2 mm, at least not significantly.
- Similar conclusion holds for heat-affected zone models, whereas parent material models show much greater relative differences, but at low level of number of cycles, making this difference not very much important either.
- Although most results are in accordance with expectations, some questions arose as for difference in „numerical“ and „analytical“ fatigue cracks behaviour in parent metal, compared to their heat-affected zone counterparts. Namely, for both heat-affected zone and parent metal either smaller fatigue life was expected in the case of analytical calculation, but this was not the case for the parent metal.

This suggests that additional analyses should be made in future research, to explain different behaviour in different welded joint regions. This implies the need to reconsider used approximation, to enable improvement of the applied models.

Another conclusion would be that relatively small changes in fatigue crack length do not make significant differences in number of cycles, indicating that future analyses should assume larger differences in crack lengths. This also indicates that the geometry of each welded joint should also change considerably, to explain increase/decreases in crack length.

Finally, it can be concluded that this approach is suitable for comparison of homogeneous welded joints with different groove geometries.

LITERATURE

References Chapter 1

- [1.1] Simon Sedmak: Integrity and life assessment of welded joints made of micro-alloyed high strength steels under static and dynamic loading, Doctoral thesis, Faculty of Mechanical Engineering, University of Belgrade, 2019.
- [1.2] S.A. Sedmak, A. Sedmak, A. Grbović, Z. Radaković: Integrity and Life Assessment of Welded Joints Made of Micro-alloyed High Strength Steels, *Advanced Materials Research*, Vol. 1157, pp. 161-167, 2020
- [1.3] Aleksandar Čabrilo: Mehaničke osobine i brzina rasta zamorne prsline u zavarenom spoju pancirnog čelika, doktorska disertacija, Fakultet Tehničkih Nauka, Univerzitet u Novom Sadu, 2018.
- [1.4] Cabrilo A., Geric, K. Weldability of High Hardness Armor Steel, *Advanced Materials Research*, Vol. 1138, pp. 79-84, 2016..

References Chapter 2

- [2.1] A. Sedmak, S. Sedmak, Lj. Milović: Pressure equipment integrity assessment by elastic-plastic fracture mechanics methods, monograph, DIVK, 2011, 294 pages.
- [2.2] M.V. Deo, P. Michaleris, J. Sun: Prediction of buckling distortion of welded structures, *Science and Technology of Welding and Joining*, Vol. 8, No. 1, 2003, pp. 55-61
- [2.3] Algoul, M.; Sedmak, A.; Petrovski, B.; Tatic, U.; Sedmak, S.; Đurdjevic, A.: Quality Assurance of a Large Welded Penstock Manufacturing by Means of Full-scale Model Testing, 2nd International Conference Manufacturing Engineering & Management 2012, 107-108, ISBN 978-80-553-1216-3.
- [2.4] M. Rutheravan: Summary of safety criteria in design, Technical report, 2016, DOI: <https://doi.org/10.13140/RG.2.1.1501.5285>
- [2.5] I. Hajro, O Pašić, Z. Burzić: Investigation of elastic-plastic fracture mechanics parameters of quenched and tempered high-strength steel welds, *Structural Integrity and Life*, Vol. 10, No. 3, 2010, pp. 225-230.
- [2.6] E. Džindo, S.A. Sedmak, A. Grbović, N. Milovanović, B. Đorđević: XFEM simulation of fatigue crack growth in a welded joint of a pressure vessel with a reinforcement ring, *Archive of Applied Mechanics*, Vol. 89, No. 5, pp. 919-926.
- [2.7] I. Vučetić, S. Kirin, T. Vučetić, T. Golubović, A. Sedmak: Risk analysis in the case of air storage tank failure at RHPP Bajina Bašta, *Structural Integrity and Life*, Vol. 18, No. 1, 2018, pp. 3-6
- [2.8] A.A. Wells: Crack opening displacements from elastic-plastic analyses of externally notched tension bars, *Engineering Fracture Mechanics*, Vol. 1, No. 3, 1969, pp. 399-410
- [2.9] James R. Rice: A Path Independent Integral and the Approximate Analysis of Strain Concentration by Notches and Cracks, *Journal of Applied Mechanics*, Vol. 35, 1968, pp. 379-386.

[2.10] Lj. Milović, V. Milošević-Mitić, Z. Radaković, N. Anđelić, B. Petrovski: Assessment of pressure vessel load capacity in the presence of cracks, *Structural Integrity and Life*, Vol. 13, No. 1, pp. 9-16.

[2.11] X. Zheng, M.A. Hirt: Fatigue crack propagation in steels, *Engineering Fracture Mechanics*, Vol. 18, No. 5, 1983, pp. 965-973

[2.12] P.C. Paris, F. Erdogan, A Critical Analysis of Crack Propagation Laws, *Trans. ASME, Journal Basic Eng.* Vol. 85, No. 4, p. 528

[2.13] E.K. Walker, An Effective Strain Concept for Crack Propagation and Fatigue with Specific Application to biaxial Stress Fatigue, *AFFDL-TR-70-144*, p. 225-233, 1970

[2.14] R.G. Forman, V.E. Kerney, R.M. Engle, Numerical Analysis of Crack Propagation in Cyclic-Loaded Structures, *Trans. ASME, Journal Basic Eng.* Vol. 89, No. 3, p. 459, 1997.

[2.15] T.L. Anderson, *Fracture Mechanics: Fundamentals and Applications*, 3rd ed., CRC Press, 2004.

[2.16] J.M. Barsom, S.T. Rolfe, *Fracture and Fatigue Control in Structures: Applications of Fracture Mechanics*, 3rd ed., ASTM International, 1999.

[2.17] M. Janssen, J. Zuidema, R.J.H. Wanhill, *Fracture Mechanics*, 2nd ed. Spon Press, 2004.

References Chapter 4

[4.1] Rakin M., Gubelj N., Dobrojević M., Sedmak A.: Modelling of ductile fracture initiation in strength mismatched welded joint, *Engineering Fracture Mechanics*, Vol. 75, Issue 11. 2008, 3499-3510.

[4.2] Rakin M, Cvijović Z, Grabulov V, Putić S, Sedmak A.: Prediction of ductile fracture initiation using micromechanical analysis. *Engng Fract Mech* 2004;71:813–27.

[4.3] Rakin M., Medjo B., Gubelj N., Sedmak A.: Micromechanical assessment of mismatch effects on fracture of high-strength low alloyed steel welded joints, *Engineering Fracture Mechanics*, Vol. 109, 2013, 221-235.

[4.4] Younise B., Sedmak A., Rakin M., Gubelj N., Medjo B., Burzić Z., Zrilić, M.: Micromechanical analysis of mechanical heterogeneity effect on the ductile tearing of weldments, *Materials and Design* 37 (2012) 193-201.

[4.5] Aleksić, B., Grbović, A., Milović, L., Hemer, A., Aleksić, V.: Numerical simulation of fatigue crack propagation: A case study of defected steam pipeline, *Engineering Failure Analysis*, Vol. 106, 2019, <https://doi.org/10.1016/j.engfailanal.2019.104165>

[4.6] Aleksić, B., Milović, L., Grbović, A., Hemer, A., Aleksić, V., Zrilić, M.: Experimental and numerical investigation of the critical values of J-integral for the steel of steam pipelines, *Procedia Structural Integrity*, Vol. 13, 2018, pp. 1589-1594.

[4.7] H. Zhou, F. Biglari, C. M. Davies, A. Mehmanparast, and K. M. Nikbin, "Evaluation of fracture mechanics parameters for a range of weldment geometries with different mismatch ratios," *Eng. Fract. Mech.*, vol. 124–125, pp. 30–51, 2014.

[4.8] Marie S, Nedelec M., Mismatch effect on CT specimen mechanical effect and consequences on the weld toughness characterization. In: *ASME conference proceedings*, vol. 2011(44533); 2011. p. 449–58.

[4.9] Donato G, Rodrigo M, Claudio R. Effects of weld strength mismatch on J and CTOD estimation procedure for SE(B) specimens. *Int J Fract* 2009;159(1):1–20.

[4.10] Ruggieri C. Further results in J and CTOD estimation procedures for SE(T) fracture specimens --Part I: homogeneous materials. *Engng Fract Mech* 2012;79: 245–65.

[4.11] Paredes M, Ruggieri C. Further results in J and CTOD estimation procedures for SE(T) fracture specimens – Part II: weld centerline cracks. *Engng Fract Mech* 2012; 89: 24–39.

[4.12] Kim YJ, Kim JS, Cho SM. 3-D constraint effects on J testing and crack tip constraint in M(T), SE(B), SE(T) and C(T) specimens: numerical study. *Engng Fract Mech* 2004;71(9–10):1203–18.

[4.13] Davies C, Kourpetis M, Nikbin K. Experimental evaluation of the J or C* parameter for a range of cracked geometries. In: 5th international ASTM/ESIS symposium on fatigue and fracture; 2007.

[4.14] Kim YJ, Son BG, Kim YJ. Elastic–plastic finite element analysis for double-edge cracked tension (DE(T)) plates. *Engng Fract Mech* 2004;71(7–8):945–66.

[4.15] Kim YJ, Budden PJ. Plastic g factor solutions of homogeneous and bi-material SE(T) specimens for toughness and creep crack growth testing. *Fatigue Fract Engng Mater Struct* 2001;24(11):751–60.

[4.16] Wilson CD, Mani P. Plastic J-integral calculations using the load separation method for the double edge notch tension specimen. *Engng Fract Mech* 2008;75(18):5177–86.

[4.17] Savioli RG, Ruggieri C. Improved J and CTOD estimation formulas for C(T) fracture specimens including overmatched weldments. In: ASME conference proceedings, vol. 2011(44533); 2011. p. 429–38.

[4.18] Xuan FZ, Tu ST, Wang ZD. A modification of ASTM E 1457 C* estimation equation for compact tension specimen with a mismatched cross-weld. *Engng Fract Mech* 2005;72(17):2602–14.

[4.19] Savioli RG, Ruggieri C. Improved J and CTOD estimation formulas for C(T) fracture specimens including overmatched weldments. In: ASME conference proceedings, vol. 2011(44533); 2011. p. 429–38.

[4.20] BS 7448-2: 1997 “Method for determination of K_{IC} critical CTOD and critical J values of weld in metallic materials”.

[4.21] BS EN ISO 12737:2010 “Metallic materials. Determination of plane-strain fracture toughness”.

References Chapter 5

[5.1] Đurđević A., Živojinović D., Grbović A., Sedmak A., Rakin M., Dascau H., Kirin S.: Numerical simulation of fatigue crack propagation in friction stir welded joint made of Al2024-T351 alloy, *Engineering Failure Analysis*, Vol. 58, 2015, pp. 477-484.

[5.2] Shibanuma K., Yanagimoto F., Namegawa T., Suzuki K., Aihara S.: Brittle crack propagation/arrest behavior in steel plate-Part I: Model formulation, *Engineering Fracture Mechanics* 162 (2016) 324-340.

[5.3] Shibanuma K., Yanagimoto F., Namegawa T., Suzuki K., Aihara S.: Brittle crack propagation/arrest behavior in steel plate-Part II: Experiments and model validation, *Engineering Fracture Mechanics* 162 (2016) 341-360.

[5.4] Machida S, Yoshinari H, Yasuda M, Aihara S, Mabuchi H. Fracture mechanical modeling of brittle fracture propagation and arrest of steel (1) – a fundamental model. *Bull Soc Naval Archit Jpn* 1995; 177:243–57.

[5.5] Aihara S, Machida S, Yoshinari H, Mabuchi H. Fracture mechanical modeling of brittle fracture propagation and arrest of steel (2) – application to temperature-gradient type test. *Bull Soc Naval Archit Jpn* 1996; 178:545–54.

[5.6] Aihara S, Machida S, Yoshinari H, Tsuchida Y. Fracture mechanical modeling of brittle fracture propagation and arrest of steel (3) – application to duplex type test. *Bull Soc Naval Archit Jpn* 1996;179: 389–98.

[5.7] Hemer, A., Milović, L., Grbović, A., Aleksić, B., Aleksić, V.: Numerical determination and experimental validation of the fracture toughness of welded joints, *Engineering Failure Analysis*, Vol. 107, 2020, <https://doi.org/10.1016/j.engfailanal.2019.104220>

[5.8] Hemer, A. M., Arandjelović, M., Milović, L., Kljajin, M., Lozanović-Šajčić, J.: Analytical vs Numerical Calculation of Fatigue Life for Different Welded Joint Regions, *Tehnički vjesnik/Technical Gazette*, Vol. 27, No. 6, 2020, TV-20200921152557

[5.9] S.A. Sedmak, A. Sedmak, A. Grbović, Z. Radaković: Integrity and Life Assessment of Welded Joints Made of Micro-alloyed High Strength Steels, *Advanced Materials Research*, Vo. 1157, pp. 161-167, 2020

[5.10] S .A. Sedmak, Z. Burzic, S. Perkovic, R. Jovicic, M. Arandelovic, Lj. Radovic, N. Ilic: Influence of welded joint microstructures on fatigue behaviour of specimens with a notch in the heat affected zone, *Engineering Failure Analysis*, Vol. 106, December 2019

[5.11] Kraedegh, A., Li, W., Sedmak, A., Grbović, A., Trišović, N., Mitrović, R., Kirin, S.: Simulation of fatigue crack growth in A2024-T351 T-welded joint, *Structural Integrity and Life*, 2017, Vol. 17, No. 1 pp. 3-6

[5.12] Sghayer A., Grbović A., Sedmak A., Dinulović M., Doncheva E., Petrovski B., Fatigue Life Analysis of the Integral Skin-Stringer Panel Using XFEM, *Structural Integrity and Life*, Vol. 17, Issue 1, (2017), 7-10.

[5.13] Sedmak A., Computational fracture mechanics: An overview from early efforts to recent achievements. *Fatigue Fract Eng Mater Struct*. 2018;41:2438–2474. <https://doi.org/10.1111/ffe.12912>,

[5.14] Sedmak, S.A., Burzić, Z., Perković, S., Jovičić, R., Arandjelović, A., Radovic, Lj., Ilic, N.: Influence of welded joint microstructures on fatigue behaviour of specimens with a notch in the heat affected zone, *Engineering Failure Analysis*, Vol. 106, December 2019

[5.15] A. Sedmak, M. Rakin, Application of fracture mechanics in assessment of structural integrity, in: S. Sedmak, Z. Radaković (Eds.), *Monograph of the VIII International Fracture Mechanics Summer School, TMF and DIVK, Belgrade, 2004*, pp. 373–386.

[5.16] Jong Wan Hu, J-Integral evaluation for calculating structural intensity and stress intensity factor using commercial finite element (FE) solutions, *Adv. Mater. Res.* 650 (2013) 379–384.

[5.17] Goran Vukelic, Josip Brnic, Numerically predicted J-integral as a measure of crack driving force for steels 1.7147 and 1.4762, *J. Theor. Appl. Mech.* 55 (2) (2017) 659–666 Warsaw.

[5.18] B. Henjica, F. Islamovic, Dz. Gačo, E. Bajramović, Numerical calculation of J-integral using finite elements method, 7th International Scientific conference on defensive Technologies OTEH, (2016).

References Chapter 6

[6.1] M. Mlikota et al. *J. Phys.: Conf. Ser.* 843, 2017, 012042

[6.2] Ž. Božić, S. Schmauder, M. Mlikota, M. Hummel, Multiscale fatigue crack growth modelling stiffened panels, *Fatigue Fract Engng Mater Struct* 00, 2014, 1-12.

[6.3] M. Mlikota, S. Schmauder, Ž. Božić, M. Hummel, Modelling of overload effects on fatigue crack initiation in case of carbon steel, *Fatigue Fract Engng Mater Struct* 40(8), 2017, 1182-1190.

[6.4] Ž. Božić, M. Mlikota, S. Schmauder, Application of the ΔK , ΔJ and $\Delta CTOD$ parameters in fatigue crack growth modelling, *Technical Gazette* 18, 3(2011), 459-466.

[6.5] Ž. Božić, S. Schmauder, M. Mlikota, Fatigue growth models for multiple long cracks in plates under cyclic tension based on ΔK_I , ΔJ -integral and $\Delta CTOD$ parameter, *Key Engineering Materials*, 2011, 1382(488) pp.525

[6.6] Simon A. Sedmak: Integrity and life assessment of welded joints made of micro-alloyed high strength steels under static and dynamic loading, Doctoral Thesis, Faculty of Mechanical Engineering, University of Belgrade, 2019.

[6.7] A. Sghayer, A. Grbović, A. Sedmak, M. Dinulović, E. Doncheva, B. Petrovski, Fatigue life analysis of the integral skin-stringer panel using XFEM, *Structural Integrity and Life*, Vol.17, No. 1, 2017, pp. 7-10.

[6.8] Abubkr M. Hemer, Mihajlo Arandjelović, Lj. Milović, M. Kljajin, Jasmina Lozanović Šajić, Analytical vs Numerical Calculation of Fatigue Life for Different Welded Joint Regions, accepted for publishing, TV-20200921152557, Vol. 27/No. 6.

[6.9] Aleksandar Cabrilo, Aleksandar Sedmak, Zijah Burzic, Srdja Perkovic, Fracture mechanics and fatigue crack propagation in armor steel welds, *Engineering Failure Analysis*, 106 (2019) 104155.

CV FORM OR STUDENT HISTORY

My name Abubkr Mohamed Hemer, I was born in Zliten, Libya on January 1, 1966 . I finished elementary and secondary school in Zliten.

I got a BSc degree in Industrial and manufacturing systems from the Faculty of engineering at the University of Benghazi in 1990/1991, by the end of fall 1990 semester, academic year1990/1991.

I got an MSc in Production Engineering; I fulfilled the requirements for the degree of Master of Technology, by the end of fall 2009 semester, academic year 2009/2010 In the postgraduate Technical program conducted at Mechanical technology branch in cooperation with the Faculty of engineering University of Tripoli (Al-Fateh University previously).

After finishing college study, I worked as production engineer in the Production department from November 15, 1991 to January 30, 1995. in Kaam industry.

I worked as director of the Mechanical maintenance department in the same industry from February 1, 1995 to November 30, 2000.

I worked as a Practical engineer from December 1, 2000 to December 31, 2006 in The Higher Polytechnic Institute Zliten

I was the staff member (as Assistant Lecturer), in The Higher Polytechnic Institute Zliten from December 31, 2010 to December 25, 2014.

I enrolled in PhD Study in Engineering material department at University of Belgrade-Faculty of Technology and Metallurgy in November 5, 2020.

ИЗЈАВА О АУТОРСТВУ

Име и презиме аутора Abubkr Mohamed Abdulhamid Abdulah HEMER

Број индекса 4038/15

Изјављујем

- да је докторска дисертација под насловом

„Еластопластично понашање завареног споја челика високе чврстоће при деловању статичког и динамичког оптерећења“

(„Elastic-plastic behavior of high strength steel welded joint under static and dynamic loading“)

резултат сопственог истраживачког рада;

- да дисертација у целини ни у деловима није била предложена за стицање друге дипломе према студијским програмима других високошколских установа;
- да су резултати коректно наведени и
- да нисам кршио/ла ауторска права и користио/ла интелектуалну својину других лица.

Потпис аутора

У Београду, 16. децембра 2020.

ИЗЈАВА О ИСТОВЕТНОСТИ ШТАМПАНЕ И ЕЛЕКТРОНСКЕ ВЕРЗИЈЕ ДОКТОРСКОГ РАДА

Име и презиме аутора Abubkr Mohamed Abdulhamid Abdulah HEMER

Број индекса 4038/15

Студијски програм Инжењерство материјала

Наслов рада „Еластопластично понашање завареног споја челика високе чврстоће при деловању статичког и динамичког оптерећења“

(„Elastic-plastic behavior of high strength steel welded joint under static and dynamic loading“)

Ментор проф. др Љубица Миловић, редовна професорка Универзитет у Београду, Технолошко-металуршки факултет

Изјављујем да је штампана верзија мог докторског рада истоветна електронској верзији коју сам предао/ла ради похрањена у **Дигиталном репозиторијуму Универзитета у Београду**.

Дозвољавам да се објаве моји лични подаци везани за добијање академског назива доктора наука, као што су име и презиме, година и место рођења и датум одбране рада.

Ови лични подаци могу се објавити на мрежним страницама дигиталне библиотеке, у електронском каталогу и у публикацијама Универзитета у Београду.

Потпис аутора

У Београду, 16. децембра 2020.

ИЗЈАВА О КОРИШЋЕЊУ

Овлашћујем Универзитетску библиотеку „Светозар Марковић“ да у Дигитални репозиторијум Универзитета у Београду унесе моју докторску дисертацију под насловом:

„Еластопластично понашање завареног споја челика високе чврстоће при деловању статичког и динамичког оптерећења“

(„Elastic-plastic behavior of high strength steel welded joint under static and dynamic loading“)

која је моје ауторско дело.

Дисертацију са свим прилозима предао/ла сам у електронском формату погодном за трајно архивирање.

Моју докторску дисертацију похрањену у Дигиталном репозиторијуму Универзитета у Београду и доступну у отвореном приступу могу да користе сви који поштују одредбе садржане у одабраном типу лиценце Креативне заједнице (Creative Commons) за коју сам се одлучио/ла.

1. Ауторство (CC BY)
2. Ауторство – некомерцијално (CC BY-NC)
3. Ауторство – некомерцијално – без прерада (CC BY-NC-ND)
4. Ауторство – некомерцијално – делити под истим условима (CC BY-NC-SA)
5. Ауторство – без прерада (CC BY-ND)
6. Ауторство – делити под истим условима (CC BY-SA)

(Молимо да заокружите само једну од шест понуђених лиценци.
Кратак опис лиценци је саставни део ове изјаве).

Потпис аутора

У Београду, 16. децембра 2020.

ОЦЕНА ИЗВЕШТАЈА О ПРОВЕРИ ОРИГИНАЛНОСТИ ДОКТОРСКЕ ДИСЕРТАЦИЈЕ

На основу Правилника о поступку провере оригиналности докторских дисертација које се бране на Универзитету у Београду и налаза у извештају из програма iThenticate којим је извршена провера оригиналности докторске дисертације **„Еластопластично понашање завареног споја челика високе чврстоће при деловању статичког и динамичког оптерећења” („Elastic-plastic behavior of high strength steel welded joint under static and dynamic loading“)**, аутора **Abubkr Mohamed Abdulhamid Abdulah NEMER**, констатујем да утврђено подударане текста износи **11%**. Ова подударност се уочава у поглављима 4 и 7 и последица је **претходно публикованих резултата докторанда проистеклих из његове дисертације**, а што је у складу са чланом 9. Правилника.

На основу свега изнетог, а у складу са чланом 8 став 2 Правилника о поступку провере оригиналности докторских дисертација које се бране на Универзитету у Београду, изјављујем да извештај указује на оригиналност докторске дисертације, те се прописани поступак припреме за њену одбрану може наставити.

20. новембра 2020. године

Ментор


Проф. др Љубица Миловић